OoC-integrated impedance spectroscopy for blood-brain barrier integrity analysis

Master Thesis

Lovro Ivančević

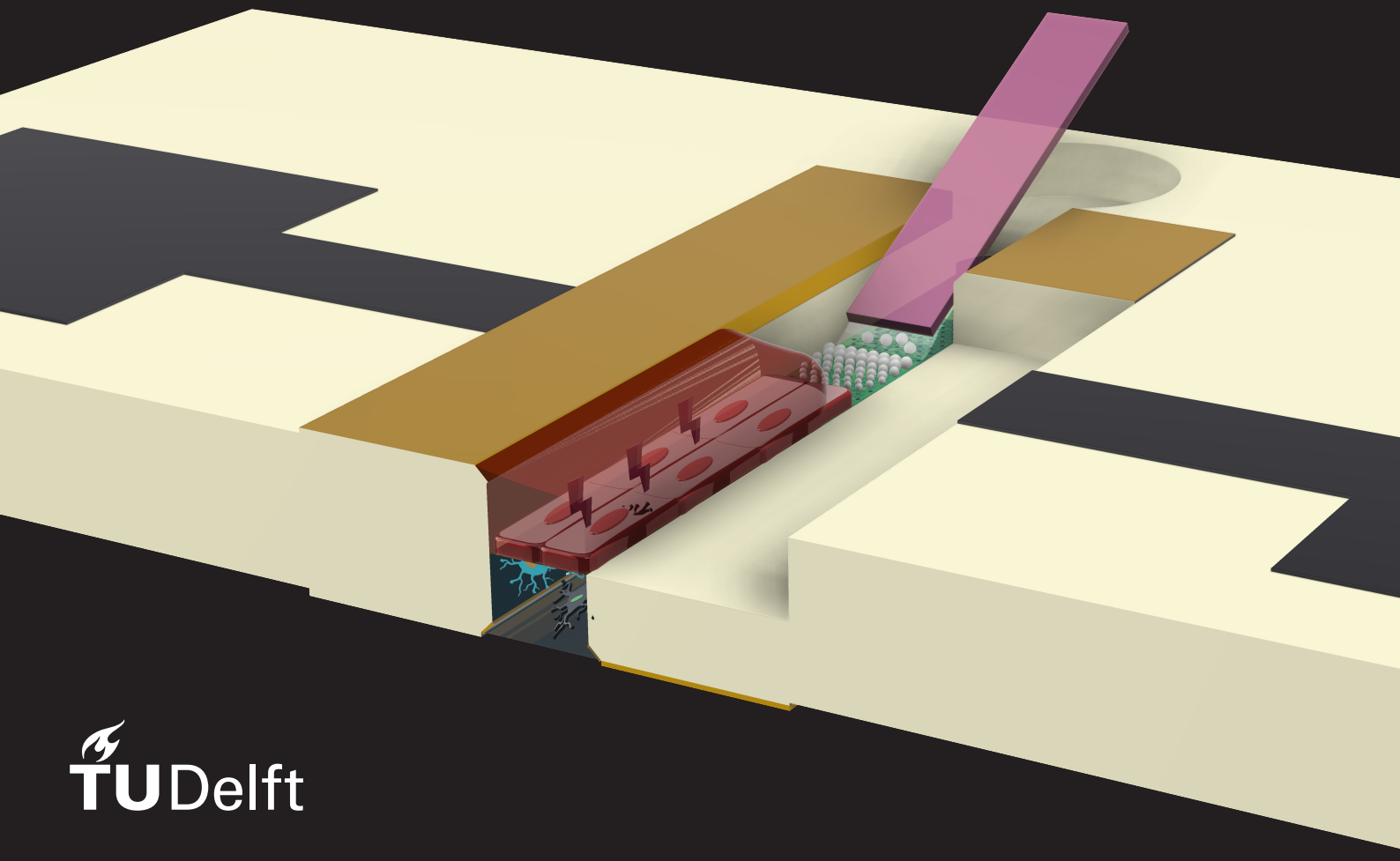

TU Delft

OoC-integrated impedance spectroscopy for blood-brain barrier integrity analysis

Master Thesis

by

Lovro Ivančević

to obtain the degree of Master of Science
at the Delft University of Technology,
to be defended publicly on October 27, 2021 at 10:00

Student number:	5140307	
Project duration:	January 2021 – October 2021	
Thesis committee:	Prof. dr. P.J. French,	TU Delft
	Dr. M. Mastrangeli,	TU Delft, supervisor
	Dr. O. Isabella,	TU Delft

This thesis is confidential and cannot be made public until October 27, 2022

TU Delft

Abstract

The lack of reliable human physiology models *in vitro* combined with an ever-increasing set of health and safety requirements imposed by pharmaceutical regulatory agencies across the world is causing a concerningly low number of new drugs to reach the market. Organ-on-Chip (OoC) technology aims to aid faster development of new drugs by providing more accurate in vitro models of human tissue, ultimately leading to a higher number of potentially successful drug candidates during preclinical testing. To achieve this, convergence of different engineering disciplines is necessary for fabricating cell culture environments that closely mimic their in vivo counterparts and offer better technological capabilities compared to conventional cell cultures by incorporating cell stimulation and sensor integration. In the case of human blood-brain barrier (BBB), these models offer invaluable insight into how BBB disruption causes neurodegeneration associated with many progressive diseases such as Alzheimer's or Parkinson's disease.

In this thesis work, a novel OoC device for measuring permeability of the blood-brain barrier using impedance spectroscopy was designed and fabricated. The core of the device is a suspended, 150nm-thin silicon nitride microporous membrane which enables an *in-vivo*-like separation distance between cells constituting the BBB. A sidewall electrode topology was proposed as it offers a fully unobstructed view of the cell culture environment. A cleanroom-based fabrication flow was devised which enabled device fabrication of a two-channel microfluidic device with integrated impedance spectroscopy electrodes. Through simulation-based modelling, the electrode topology was optimized and was shown to be highly uniform in terms of measurement sensitivity, removing the need for commonly used measurement correction functions. To go beyond the limits of photolithography, a process flow utilizing convective self-assembly-based nanosphere lithography was demonstrated in fabricating sub-500 nm diameter pores, thereby facilitating higher pore density per cultured cell.

A preliminary testing setup was designed, but due to machine unavailability in the cleanroom the full fabrication of the device could not be completed and testing of the final device is expected to be done in the future in a biology lab. The proposed electrode geometry design and fabrication flow can be extended to other OoC-integrated barrier tissue models utilizing more conventional polymer-based substrates.

Contents

1

Literature Review

1.1. Industry trends in drug development

Modern pharmaceutical industry is heavily dependent on patent ownership. The grand economical scale of this dependence became apparent in 2012, when Pfizer's patent over cholesterol-lowering drug Lipitor expired, leading to a sudden revenue loss of 5 billion USD. Prior to that, Lipitor had been the world's most successful prescription drug [1].

In economic jargon, this is often referred to as the 'patent cliff', as the revenue loss that happened with Pfizer's Lipitor is happening repeatedly when branded drugs become generic and producible by other companies at a lower price. Pharmaceutical companies have developed different strategies for dealing with this issue but an important takeaway is that, at least from an economical viewpoint, in order to ensure business growth, new 'blockbuster' drugs need to be developed consistently [1].

This is in contrast with the increasing research and development costs associated with drug development. R&D productivity in pharmaceutical industry has been consistently lowering through the years (as shown in Figure 1.1) and the number of drugs approved by US Food and Drug Administration has been halving approximately every 9 years per 1 billion USD spent on R&D since 1950. Adjusted for inflation, cumulatively this equals an 80-fold decrease. Interestingly, this phenomenon in pharmaceutical industry has been named Eroom's law, since it behaves in opposite to Moore's law in microelectronics where the number of transistors per chip had been doubling steadily every two years [2].

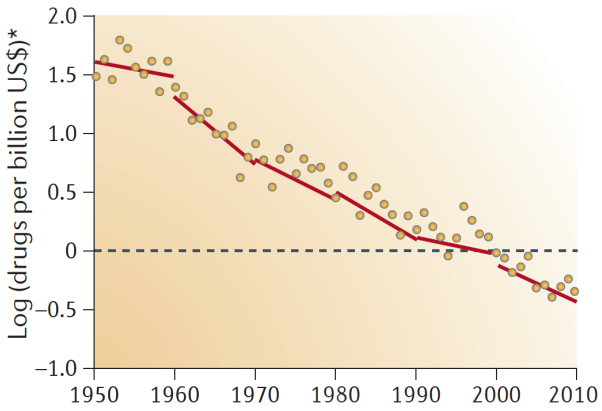

Figure 1.1: Rate of decline in pharmaceutical R&D productivity over 10-year periods. Adapted from [2].

The bulk of the increasing costs in drug development comes from drugs which never reach the market due to failure in clinical testing. 96% of new drugs that are developed eventually fail [3], but perhaps a more interesting number is the failure rate of 90% for new drugs that reach the clinical testing stage. This is a clear indication that there is a lack of understanding on working mechanisms of human physiology and that models used in preclinical drug testing cannot replicate human *in vivo* conditions accurately, causing new drugs to pass through to the next, significantly more expensive testing stage, without sufficient certainty of

success.
For these reasons, the field of bioengineering has in recent years been developing alternative models for recapitulatin human physiology *in vitro*, in order to replace conventional *in vitro* testing methods and *in vivo* testing on animals.

1.2. Alternative *in vitro* models for human physiology

In order to create better *in vitro* models, current research efforts in mimicking human phyisiology can be divided into two main subgroups [4]: organoids and organs-on-chip (OoC).

Organoids are *'stem-cell derived or progenitor-cell derived 3D structures that on much smaller scales, re-create important aspects of the 3D anatomy and multicellular repertoire of their physiological counterparts and that can recapitulate basic tissue-level functions'* [5].

Organ-on-a-chip is *'a fit-for-purpose microfluidic device, containing living engineered organ substructures in a controlled microenvironment, that recapitulates one or more aspects of the organ's dynamics, functionality and (patho)physiological response* in vivo *under real-time monitoring'* [6].

Although the two model groups bear similarities, there are important differences that need to be emphasized. Organoids are formed through self-organization of differentiated cells inside hydrogels or hanging drops and are in that sense stochastic with little control over their morphology. Although this is desirable as cells can form structures which are accurate representative of their *in vivo* counterparts, their behaviour is difficult to analyze under applied stimulus (such as a chemical gradient) and the technology still suffers from high variability [4].
OoC devices on the other hand are created using known microfabrication techniques which enable precise control over device topology in order to facilitate cell culturing in a physiologically more relevant environment. The level of complexity of these devices can range from simple devices, that mimic a single functionality of a given tissue to sophisticated multi-organ systems which interconnect different 'organs', in order to model complete organ systems such as the reproductive system.
The organ-on-chip development gained considerable traction after the demonstration of the first lung-on-a-chip device by Huh *et al.* in 2010 [7] (shown in Figure 1.2). Although it was not the first microfluidic model of a tissue, it was the first which provided relevant mechanical stimulation to epithelial airway tissue demonstrating its importance in general design of biomimetic devices.

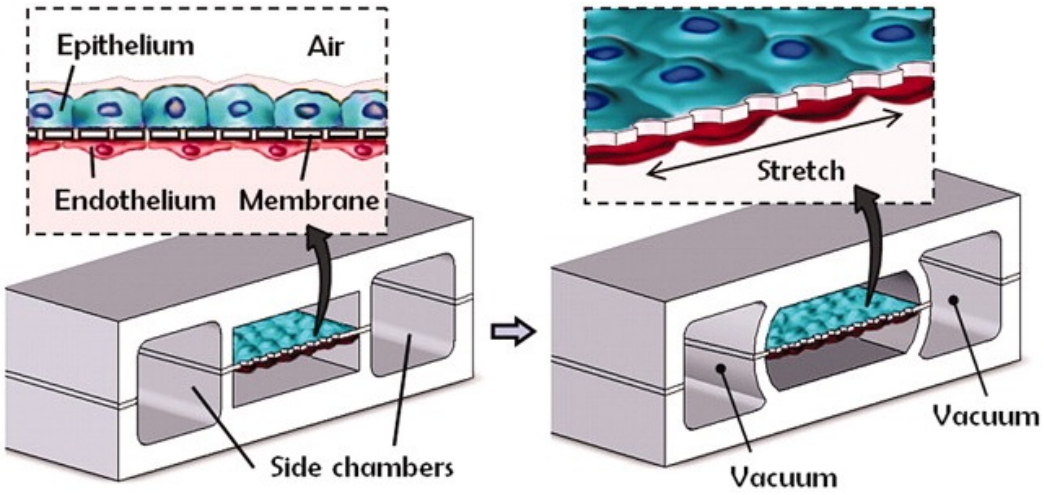

Figure 1.2: Lung-on-a-chip, the first proof-of-principle for organ-on-chip technology. Adapted from [7].

A wide variety of devices have been constructed and characterized since then, but a common design paradigm can be deduced from these research efforts, which is to think of the human body from a reverse engineering perspective. Determining the simplest principles on why and how a certain tissue performs its function is crucial in developing synthetic biological models [8]. Using such a design paradigm, OoC devices are expected to be sufficiently accurate compared to their *in vivo* counterpart in modelling (patho)physiology

whilst retaining technical feasibility.

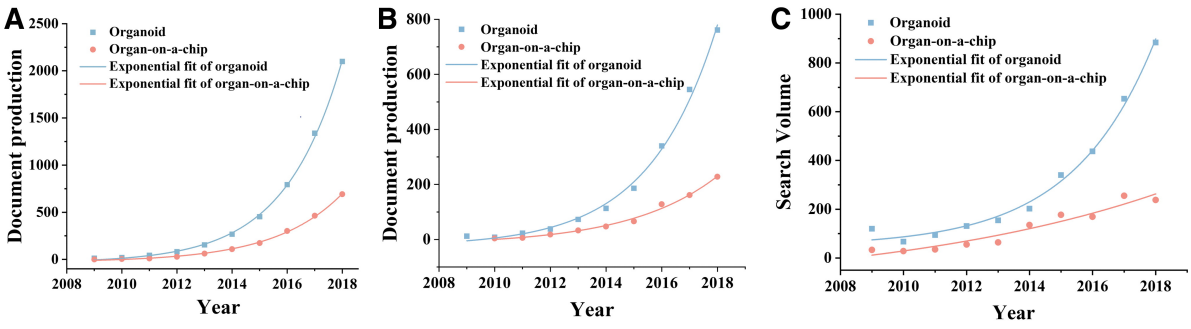

Figure 1.3: Number of articles on organoids and organs-on-chip through the years (A, B represent the number of articles published cummulatively and yearly, respectively. C represents the social impact determined from Google Trends). Adapted from [9].

The number of publications and social impact of the technology has been increasing exponentially since the first OoC device (shown in Figure 1.3).
From a pharmaceutical business perspective, a valid question is whether organ-on-chip technology can benefit the end user to a sufficient degree that it is worth investing in its development. Although the technology is still in its early stages far from general adoption [6], a study has been conducted which estimated the impact in pharmaceutical R&D costs by adoption of OoC technology [10]. In Figure 1.4 estimated impact on different cost drivers during each development stage is shown. In the research a total cost reduction is estimated between 10% and 26% per new drug (equalling to reduction of between 170 and 760 million USD, depending on the expected cost of a drug today, which is also an estimated value). However, as can be seen from the Figure 1.4, 80% of experts in the survey (all of whom are in leading positions in pharmaceutical/biotechnological/OoC companies and have prior experience with OoC) do believe that success rate in preclinical trials can be improved by OoC technology and a similar number believes that project costs can be lowered.

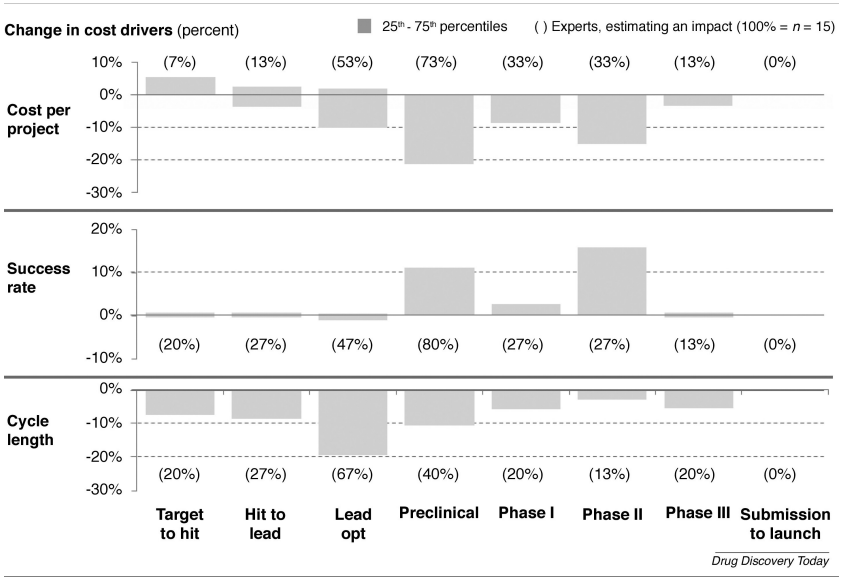

Figure 1.4: Estimated impact of OoC adoption on R&D cost reduction per drug development stage. Cost per project refers to the total R&D cost of each drug and cycle length to the total time between each new successfully developed drug. Adapted from [10].

With the above given explanation of organ-on-chip technology and its implications for pharmaceutical industry, it can be concluded that organs-on-chip present a viable alternative to conventional *in vitro* cell cultures and animal models.

In this thesis, a novel OoC device will be designed for monitoring integrity of the human blood-brain barrier using impedance spectroscopy.

1.3. Blood-brain barrier

The blood-brain barrier (BBB) represents a highly selective interface between blood and brain tissue. Its existence was first noticed by Paul Ehrlich and Edwin Goldman at the start of twentieth century, when they discovered that different dyes injected in the blood stream did not stain the cerebrospinal fluid, indicating the presence of a physiological border between the two tissues.
The BBB is one of three barriers present in the central nervous system (CNS), the other two being the blood-cerebrospinal fluid barrier and the arachnoid barrier. BBB is considered the most important of the three and physically the largest (with an estimated area between 12 and 18 m^2[11]). The main function of the BBB is restricting the passage of molecules which could potentially harm the CNS. Although this is a favourable characteristic for maintaining homeostasis in the CNS, it is also the greatest obstacle in development of new drugs for CNS-related diseases. What's more, the working mechanisms of the BBB are still not fully understood which further hinders drug development.

1.3.1. Neurovascular unit

In the past it was considered that blood-brain barrier functionality is achieved solely by a confluent monolayer of brain microvascular endothelial cells (BMECs), but more recent research is showing a strong dependency of barrier properties on other cell types. These mainly include other vascular cells (pericytes and vascular smooth muscle cells, with the already mentioned endothelial cells) and glial cells (astrocytes, microglia and oligodendria), although neurons are also known to influence transport selectivity [12]. Vascular cells are separated from glial cells by a 20-200 nm thick basement membrane which is formed from extracellular matrix (ECM) of proteins. To emphasize the importance of intercellular coupling in achieving barrier functionality, blood-brain barrier is now commonly referred to as the neurovascular unit (NVU).
A schematic overview of the neurovascular unit is shown in Figure 1.5.

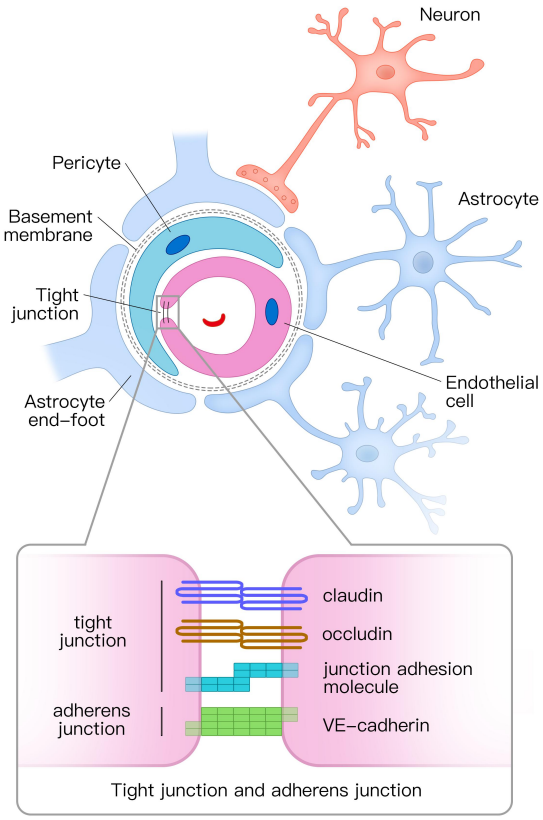

Figure 1.5: Schematic overview of NVU. Adapted from [13].

1.3.2. Endothelial cells

Endothelial cells line the lumen of vessels in the circulatory system. Their most notable characteristic is the formation of tight and adherens junctions between them by secretion of different proteins. In the NVU, these junctions are considered to be responsible for restricting paracellular passive transport (i.e. between cells) of 100% of large molecules (defined as molecules with a molecular weight larger than 400 Da), and 98% of small molecules (molecules that can pass are lipid-soluble).
Tight junctions (zonula occludens (ZO)) of the NVU are formed by a variety of proteins, but the most important ones include claudins, occludin and junction adhesion molecules (JAMs). Downregulation (i.e. decrease in quantity) of any of these proteins more or less severely influences the permeability of blood-brain barrier. As an example, it was found that lack of claudin-5 gene expression (through genetic modification) in newborn mice resulted in increased paracellular permeability and subsequent death. In humans, different neurodegenerative disorders such as multiple sclerosis [11] and Alzheimer's disease [14] are known to change the gene expression of these proteins in neurovascular cells.

1.3.3. Pericytes

Pericytes are vascular cells surrounding endothelium. They are responsible for maintaining vascular wall stability, angiogenesis (formation of blood vessels) and removal of toxins through phagocytosis [12]. Because of their proximity to endothelial cells, they communicate with ECs through paracrine signalling and have the ability to change EC gene expression. They also have a role in communication between astrocytes and endothelial cells, as lack of pericyte presence causes abnormal distribution of astrocytes (i.e. pericytes function as 'cues' for attachment of astrocytes to blood vessels [15]).

1.3.4. Astrocytes

Astrocytes are glial cells that are found on the opposite side of the basement membrane in the NVU. Their characteristic end-feet (as shown in Figure 1.5) present the direct interface between neural cells and vascular cells [11]. This tight coupling is represented best in an event of damage to the brain tissue (related to aging, neurodegenerative disease, etc.). Astrocytes in such events change their phenotype (also known as astrocyte reactivity), resulting in a change in their morphology and functionality in order to restore the blood-brain barrier, protect the neurons and maintain homeostasis [16] (shown in Figure 1.6).

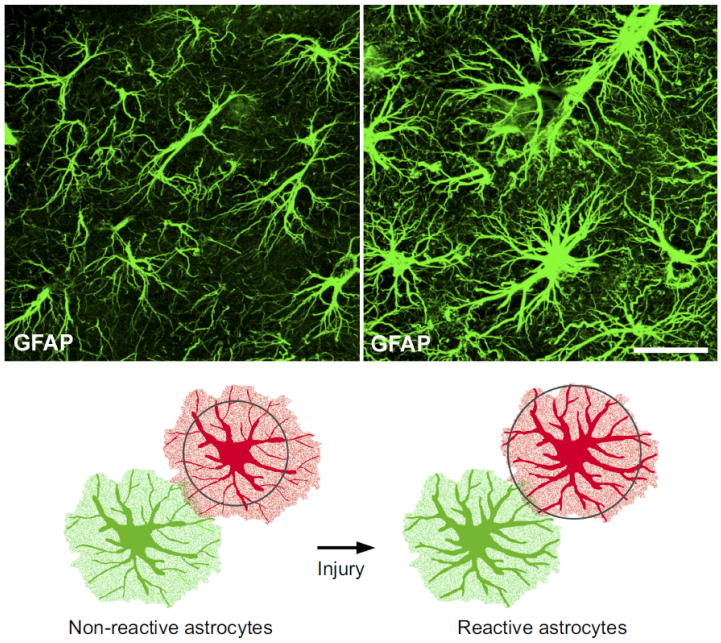

Figure 1.6: Astrocyte reactivity in response to mice brain lesion. Adapted from [16].

As can already be seen from the brief description of different cell types forming the neurovascular unit, the blood-brain barrier is a highly complex cellular system dependent on tightly regulated interaction between different cells in order to protect the brain. Dysfunction in any of the constituent parts which form the blood-brain barrier is both a cause and a consequence of many neurodegenerative diseases for which effective remedies are yet to be found. Novel remedies for treating neurodegenerative diseases are often targeted directly at the blood-brain barrier and not the neural tissue itself, as there is growing evidence that treating the barrier is crucial in restoring homeostasis and allowing the neural tissue to heal.

1.4. Assessing barrier permeability

The key functionality of any physiological barrier is the selective transport of molecules between different tissues or environment. Selectivity is achieved both physically (size restricted passive transport through tight junctions) and biochemically (mainly concerning active transcellular transport mechanisms). In order to monitor the barrier permeability, different techniques are used but they can be separated in three main groups [17]:

- techniques utilizing biochemical methods
- techniques utilizing quantitative chemistry
- techniques utilizing electrochemical methods

1.4.1. Barrier assessment by monitoring expression of biomarkers

Analytical chemistry methods are used to detect expression of different barrier specific proteins (such as claudins or JAMs), which are responsible for the formation of tight junctions between epithelial or endothelial cells. These techniques include polymerase chain reaction (PCR) and its more advanced variants (RT-PCR, qRT-PCR), western blotting and immunohistochemistry. Despite the ability to give explicit measurement of barrier composition on a molecular level, these techniques are considered end-point (i.e. at the end of a cell culture) and cannot give a real-time measurement of barrier permeability.

1.4.2. Barrier assessment using quantitative chemistry

A second group of techniques utilizes labeled solutes (fluorescent or radioactive solutes) and quantification on the amount of labeled solutes that pass from the apical side to the basolateral side of the barrier. This can either be done using imaging (e.g. particle counting) or more commonly, by measuring concentration difference between the two sides. These measurements are considered to be highly accurate, but they are invasive, possibly cytotoxic (depending on the used solute) and require specialized (often expensive) equipment.

1.4.3. Barrier assessment using electrochemical methods

First notable use of electrochemistry to quantify permeability of physiological barriers was done by Hans H. Ussing in 1950. His system (nowadays named the Ussing chamber, shown in Figure 1.7) was used to measure transport of sodium ions in isolated frog skin [18].
The skin was placed as a separator between two compartments filled with equally concentrated Ringer solutions (isotonic solution of different salts) in order to ensure that no transport occurs because of concentration difference. In this environment, active transport through the membrane occurs due to differences in concentration of ions between intracellular and extracellular space. However, this creates an electric potential difference due to the now generated charge imbalance. A balance between these two effects is what generates the transmembrane potential. If now a current is applied between the opposite sides of the membrane in order to bring the potential difference back to zero (i.e. current gradient in the opposite direction to the transmembrane potential gradient), it's value can be used as a quantifier on membrane permeability.
This device is still in use today for measurements on isolated or substrate-grown epithelial tissue, albeit with some improvements which compensate for other membrane transport mechanisms (e.g. non-ionic transport) and unwanted electrochemical effects (e.g. electrode polarization due to use of DC current).

The electrical impedance exhibited by cells forming physiological barriers is what is nowadays considered one of the key parameters for determining barrier properties. Therefore it is important to give an explanation on the origin of this bioimpedance, before going into specific measurement techniques.

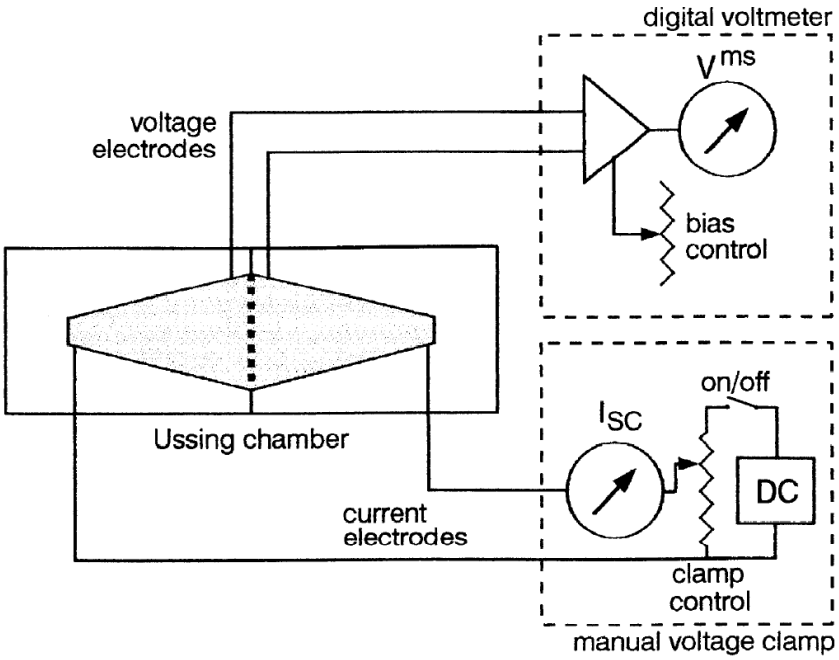

Figure 1.7: Ussing chamber for determining electrical resistance of epithelial tissue. Adapted from [19].

Origin of cellular electric impedance

All animal cells consist of a cell membrane, cytoplasm, nucleus and different organelles (cellular subunits responsible for achieving different cell functions, e.g. ribosomes for protein synthesis).
Briefly, the cytoplasm is a mixture of water, dissolved salts and different organic molecules. It behaves as an electrolyte, much like the extracellular fluid. Cell membrane consists of a very thin (≈7nm) self-assembled lipid bilayer which isolates the cytoplasm and organelles from extracellular fluid. It is a strong electrical insulator, which combined with the extracellular fluid and cytoplasm forms a capacitor [20].
This construction enables an approximation of cells as conductive spheres with an insulating thin shell (as shown in Figure 1.8), and the use of electromagnetic theory for cell modelling.

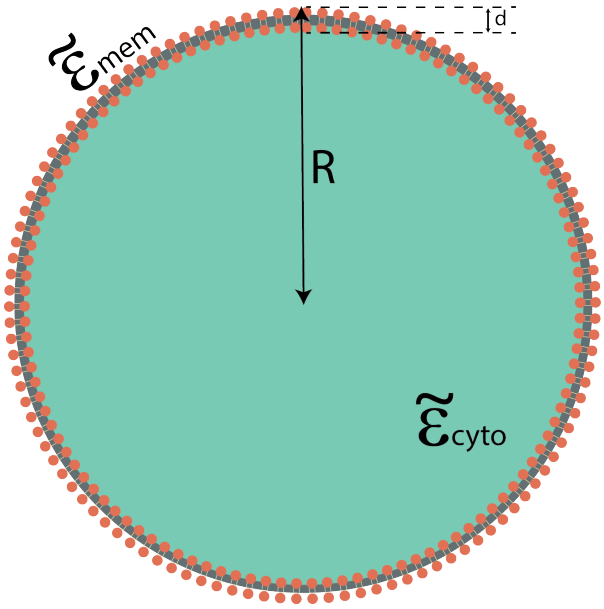

Figure 1.8: Equivalent electromagnetic model of a cell.

Single cell's complex permittivity can therefore be modelled as [21]:

$$\widetilde{\epsilon}_{cell} = \widetilde{\epsilon}_{mem} \frac{\left(\frac{R}{R-d}\right)^3 + 2\left(\frac{\widetilde{\epsilon}_{cyto} - \widetilde{\epsilon}_{mem}}{\widetilde{\epsilon}_{cyto} + 2\widetilde{\epsilon}_{mem}}\right)}{\left(\frac{R}{R-d}\right)^3 - \left(\frac{\widetilde{\epsilon}_{cyto} - \widetilde{\epsilon}_{mem}}{\widetilde{\epsilon}_{cyto} + 2\widetilde{\epsilon}_{mem}}\right)} \tag{1.1}$$

where complex permittivities of cytoplasm and membrane are defined as $\widetilde{\epsilon}_{cyto} = \epsilon_{cyto} + \frac{\sigma_{cyto}}{\omega j}$ and $\widetilde{\epsilon}_{mem} = \epsilon_{mem} + \frac{\sigma_{mem}}{\omega j}$ respectively. R and d are cell radius and membrane thickness.
The analysis can further be extended by using Maxwell's mixture theory to include the extracellular medium:

$$\widetilde{\epsilon}_{mix} = \widetilde{\epsilon}_{med} \frac{1 + 2\phi f_{CM}}{1 - \phi f_{CM}} \tag{1.2}$$

where ϕ is the ratio of cell volume to total volume and f_{CM} is Clausius-Mossotti factor defined as:

$$f_{CM} = \frac{\widetilde{\epsilon}_{cell} - \widetilde{\epsilon}_{med}}{\widetilde{\epsilon}_{cell} + 2\widetilde{\epsilon}_{med}} \tag{1.3}$$

The analysis above does not include frequency dependent dielectric dispersion, which exists due to a delay between applied frequency-dependent electric field and dielectric polarization. In cell analysis, three distinct regions can be identified [20] (shown in Figure 1.9):

- α-dispersion - caused by polarization of ions in the cell medium (up to a few kHz)
- β-dispersion - caused by polarization of cell membrane (at lower frequencies, up to a few MHz) and of cell cytoplasm (at higher frequencies, up to 100MHz)
- γ-dispersion - caused by polarization of water molecules (at microwave frequencies)

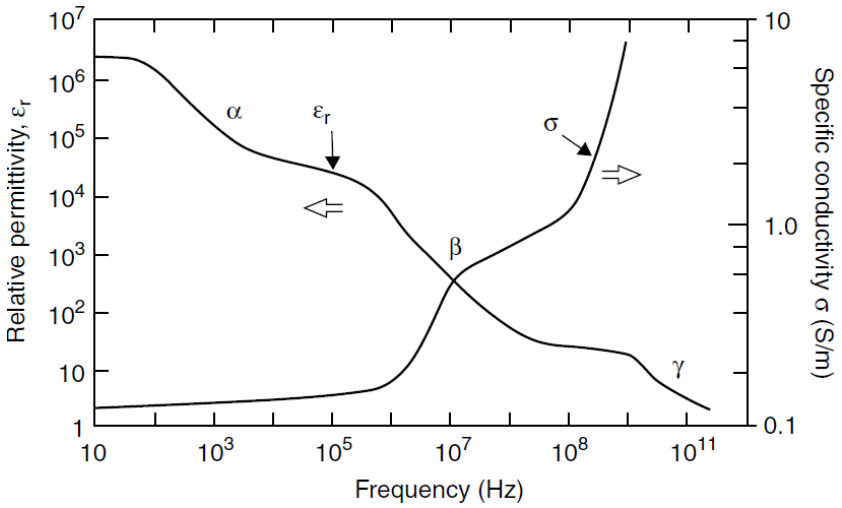

Figure 1.9: Conductivity and permittivity of cells as a function of frequency. Adapted from [22].

Frequency regions where α- and β-dispersion occur are of interest in studying tissue bioimpedance as they are influenced by cell morphology, proliferation, etc. Therefore, most commercial and non-commercial barrier measurement assays are focused on this frequency range. These assays can be split in two different categories:

- assays utilizing measurement of transendothelial (or transepithelial) electrical resistance (TEER),
- assays utilizing electric cell-substrate impedance sensing (ECIS)

The latter two assays will be explained in this section and TEER will be explained in more detail in the later section as it is the main part of this thesis.

Electric cell-substrate impedance sensing (ECIS)

Electric cell-substrate impedance sensing is a measurement technique which utilizes impedance spectroscopy in order to monitor cellular adhesion, spreading and proliferation [20].
The technique is directly derived from the analysis given previously on single cells, but finds use mainly in analysis of multiple cells. As shown in Figure 1.10, cells are cultured directly on electrodes (typically made of gold, although other materials like aluminium and titanium have been reported [23]).

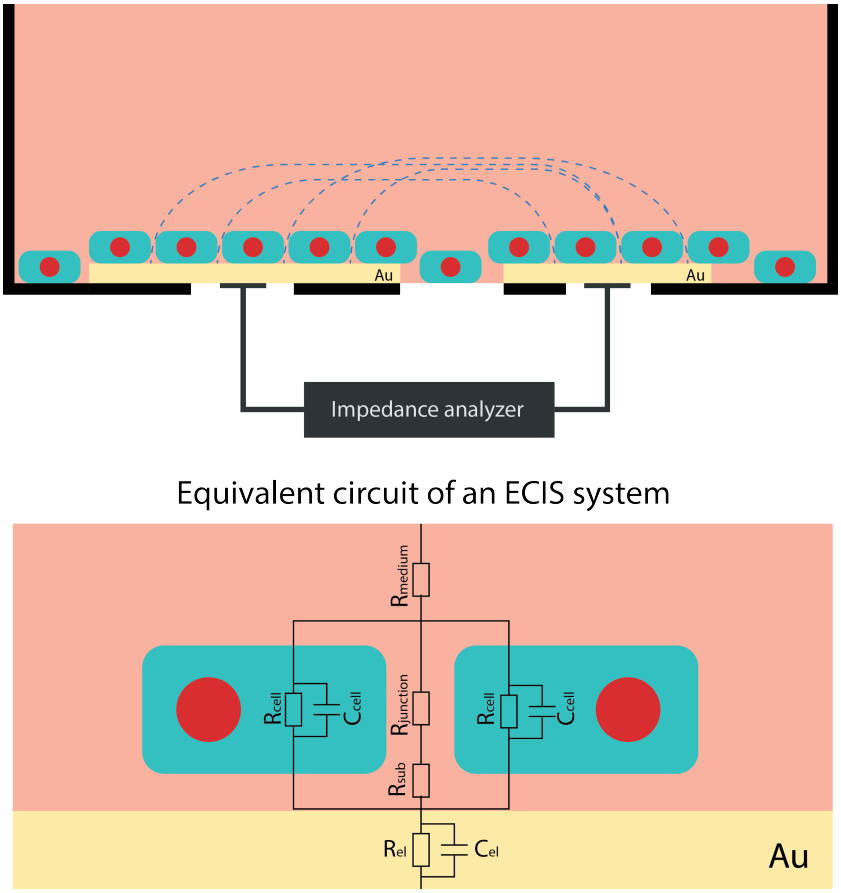

Figure 1.10: A schematic drawing of an ECIS system.

As can be seen from Figure 1.10, cell characterization is done by measuring AC impedance of cells adherent to electrode.
This can be done either by monitoring impedance at a single frequency or by obtaining an impedance spectrum (usually from 100Hz to 100kHz) [20]. The second option is preferred as it enables parameter extraction from the obtained spectrum by fitting the measured frequency spectrum to that of an equivalent circuit (shown on the bottom of Figure 1.10). The lumped element equivalent circuit is used as then analysis is simpler compared to the single cell analysis given in the previous section.
An example of a real-time single frequency measurement (at 4000Hz) and a real-time multifrequency measurement is given in Figure 1.11. As can be seen, due to the proximity to electrodes three parameters are extracted in real-time (tight junction resistance R_b, basal adhesion α and monolayer capacitance C_m). Basal adhesion measurement is not possible with other techniques [24], which is the main benefit of ECIS.
Proximity to the electrodes is also a major disadvantage of ECIS, as variable cell coating density is a common error source which can considerably alter the measured impedance [25]. This can be managed by precisely controlled cell seeding on functionalized electrode surfaces (cells cannot adhere sufficiently well on native gold surfaces, so they need to be coated either with artificial ECM or with a hydrophilic material like SiO_2 [24]).
Furthermore, optical imaging capabilities of ECIS are low, as cells are cultured on opaque electrodes which cover a large area of the culture. This issue has been somewhat mitigated by the use of transparent electrodes made from materials like transparent indium tin oxide (ITO) [26], but these electrodes are known to suffer

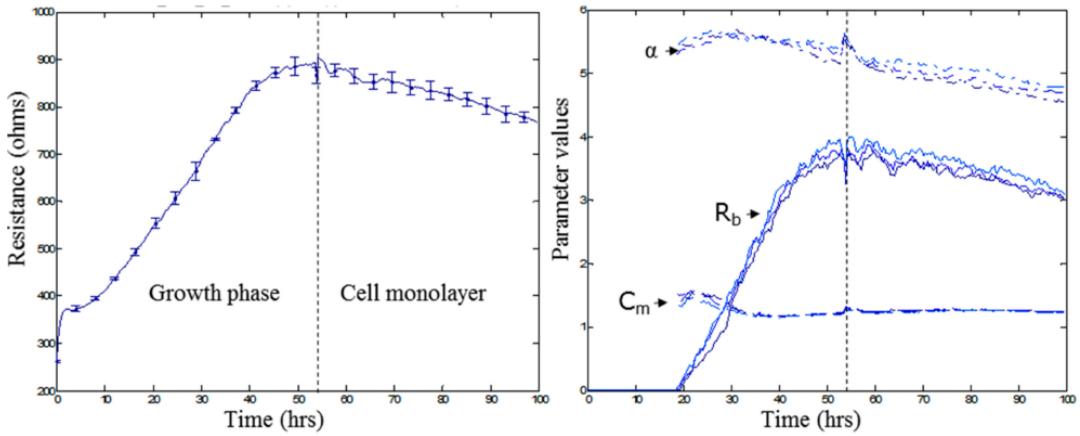

Figure 1.11: Example of a real-time ECIS measurement over a single frequency (left) and over a frequency spectrum which enables parameter extraction (right). Adapted from [25].

from poor conductivity as their transparency is increased as well as from performance variability due to fabrication. If a single cell culture is used, this drawback would not be as significant for biologists, but in cell co-cultures where cells are separated by a membrane, imaging of different cells is limited. For these reasons, ECIS measurements are best utilized if employed on single cell cultures with a non-porous stiff substrate [25].

1.5. Transendothelial/transepithelial electrical resistance (TEER)

Transendothelial/transepithelial electrical resistance (TEER) is defined as the electrical resistance across a cellular monolayer that exists due to tight junctions between barrier cells [27].
Using this definition, it is important to highlight the most important and often overlooked shortcoming of TEER measurements and that is that they cannot be used as an all-round solution for assessing barrier functionality as they are only indicative of tight junction formation [28], which is in the case of blood-brain barrier a marginal contribution to overall membrane transport. For this reason, TEER measurements are often combined with other barrier assessment techniques to gain better insight in barrier permeability.
Conventionally, TEER is measured in well plates with Transwell inserts (semipermeable membranes designed to fit inside well plates, as shown in Figure 1.12). Cells are then cultured either on one or both sides of the membrane. Once a confluent monolayer of cells is grown, electrodes are manually placed inside the well. A small voltage or current signal is applied across the two sides of the membrane and resistance is measured. An extra step is commonly employed prior to beginning the measurement, which is to measure resistance of cell medium before cells are cultured.
In this way the measured resistance is only a function of cell monolayer resistance (without considering any other error sources, which will be analyzed later):

$$R_{cell} = R_{measured} - R_{blank} \tag{1.4}$$

As wells of different sizes are used and measured resistance is dependent on the conductive area, TEER is usually normalized by multiplying resistance (in Ω) by membrane area (in cm^2) so that results are comparable across literature:

$$TEER = (R_{measured} - R_{blank}) \cdot A \tag{1.5}$$

To prevent electrode polarization and cell damage, a low-frequency square-wave AC current is applied (10μA at 12.5Hz for the most commonly used EVOM2 Voltohmmeter [27]). In analysis, this frequency is low enough that impedance measurement can be considered to be at DC and have a purely resistive nature.
As was already seen with other electrochemical measurement techniques, by expanding DC (or single AC frequency) measurements with impedance spectroscopy greater understanding of cell behaviour can be gained (in further text this will be referred to as electrical impedance spectroscopy (EIS)). Because of relatively large electrode distance from cells, in TEER measurements cells can be approximated as charged particles, instead of dipoles. This inherently limits the capabilities of TEER/EIS measurements compared to ECIS, so only paracellular resistance (TEER) and monolayer capacitance (C_m) can be measured [24].

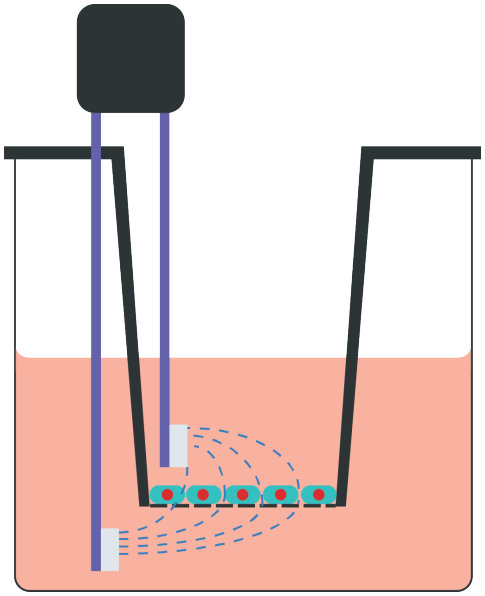

Figure 1.12: Transwell setup for measuring TEER.

1.6. Overview of notable OoC barrier models

In this section, an overview of important OoC models for physiological barriers will be given. Focus is placed on models which utilize TEER/EIS measurements with integrated electrodes, but it is not limited exclusively to blood-brain barrier as techniques regarding impedance spectroscopy are translatable across different physiological barriers. Models are ordered chronologically to illustrate development of OoC barrier models. Systematic recapitulation of different models is given in Table A.1 of the Appendix. This list is more extensive and it includes other reviewed models which are not necessarily significant for TEER/EIS improvements but introduce other novelties.

Two-channel OoC device with BBB cell co-culture - Booth *et al.*, 2012/2014

Figure 1.13a shows a BBB microfluidic model by R. Booth and H. Kim [29][30]. The device consists of two perpendicular microfluidic channels fabricated in PDMS with the channels connected through a track-etched 10μm thick PET membrane with 0.4μm pores. The device includes large Ag/AgCl electrodes produced by sputtering of Cr/Ag/Au and subsequent chlorination to achieve an electrochemically active surface. Electrodes are arranged in a four probe setup, where the current electrodes cover 75% of the culture area to ensure uniform current flow. Barrier assessment was done by measuring TEER using an EVOM2 Voltohmmeter (DC), by measuring permeability with fluorescent tracers (FITC-dextrans) and by immunostaining for tight junction proteins. All three assessment methods showed barrier formation. Due to large coverage by opaque electrodes, imaging capabilities of this configuration are low and limited to fluorescence microscopy.
This is the first two-dimensional BBB microfluidic model that included physiologically relevant flow-induced shear stress (in the second publication [30], first publication [29] used a low shear stress) and a relatively thin membrane which enabled cell-cell contacts. As can be seen from TEER values obtained in Figure 1.13b, the work successfully demonstrated the importance of cell co-cultures and fluid flow for achieving higher BBB integrity which paved the way for new microfluidic BBB models.

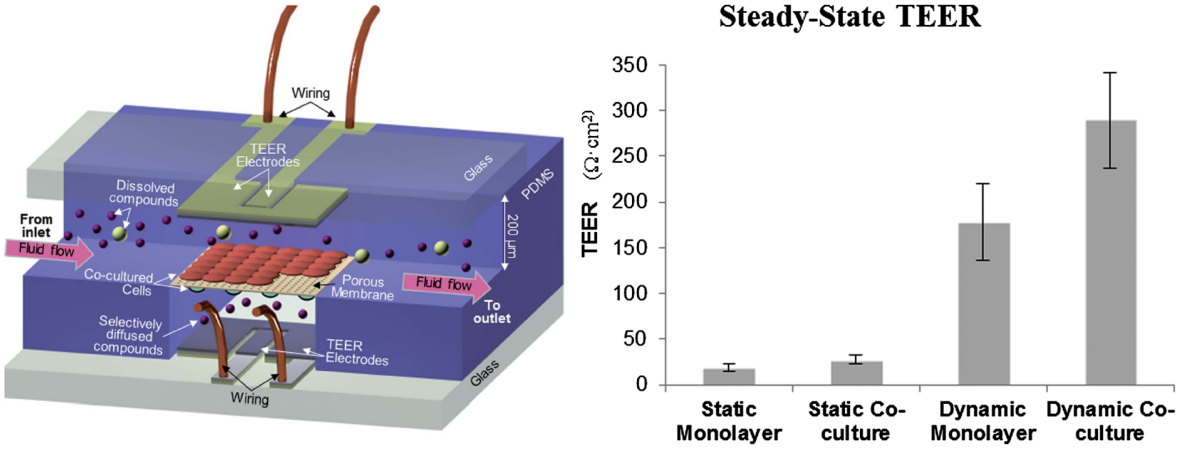

(a) 3D render of the model.

(b) Steady state TEER measured by the model.

Figure 1.13: μBBB by R. Booth and H. Kim. Adapted from [29].

Two-channel OoC device utilizing impedance spectroscopy for BBB analysis - Griep *et al.*, 2013

Figure 1.14a shows a BBB OoC device fabricated by L.M. Griep *et al.* [31]. Similarly to the previous model, the device consists of two perpendicular microfluidic channels fabricated in PDMS.

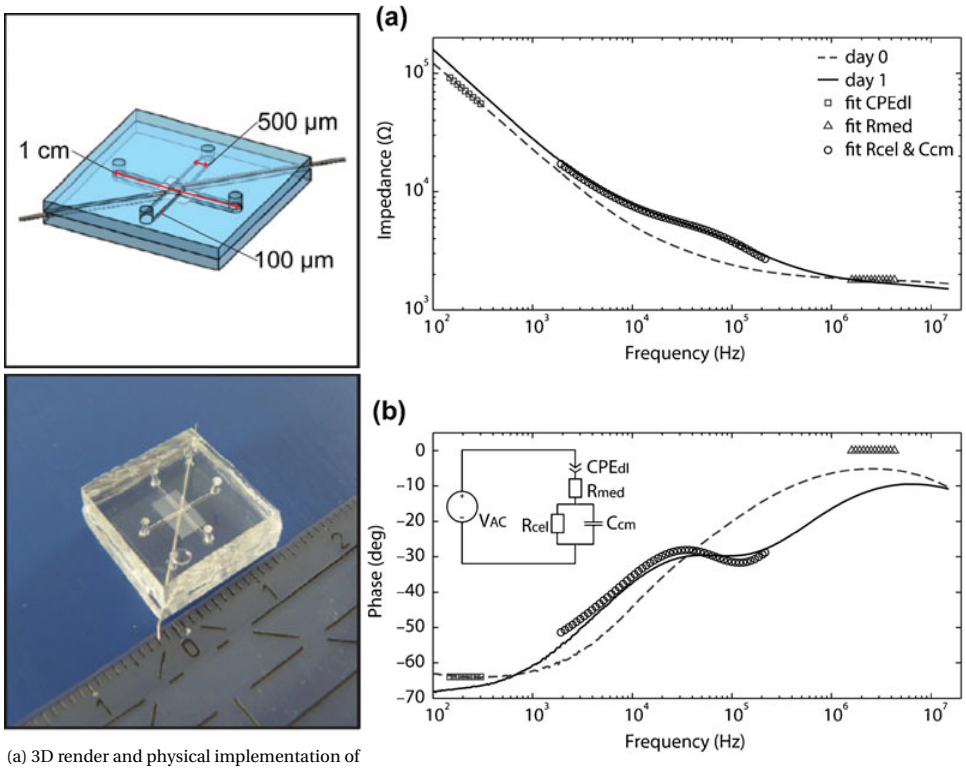

(a) 3D render and physical implementation of the model.

(b) Impedance spectrum measured by the model.

Figure 1.14: BBB on chip by Griep et al. Adapted from [31].

In contrast to the DC TEER measurements utilized in the previous model, here inert Pt electrodes are used together with EIS (shown in Figure 1.14b). Two wire Pt electrodes are fixed in PDMS on opposite sides of the membrane using glue. At low frequencies, the impedance measurement suffers from considerable offset due to the influence of double layer capacitance. Furthermore, as wire electrodes are placed manually inside the PDMS openings, measurement repeatability across devices is compromised, and authors suggest the use of

sputtered electrodes for better batch-to-batch control.
The hCMEC/D3 culture (immortalized human brain endothelial cells) was also tested for tight junction protein expression (ZO-1) with fluorescent staining and showed tight junction formation.

TEER measurement standardization in microfluidic OoC devices - Odijk *et al.*, 2015

In 2015, M. Odijk *et al.* published the first attempt of TEER measurement standardization. Through lumped element modelling of a two-channel microfluidic device, they introduced a correction scheme (shown in Figure 1.15a) which is used to normalize values measured in a microfluidic channel to that measured by an ideal Transwell setup (they assumed that Transwell measurements have a uniform current distribution which is only possible when using an EndOhm chamber). As they demonstrate in Figure 1.15b, if wire electrodes are placed at the channel openings, current distribution through the device is highly non-uniform and also dependent on the actual TEER values (which the cell culture would exhibit in a uniform current density device). Furthermore, they demonstrated a strong dependency of cell layer coverage to the measured TEER values, where a 0.4% defect in cell coverage area can decrease TEER value by 80%. The influence of a defect of this size is not measurable using other barrier assessment methods.

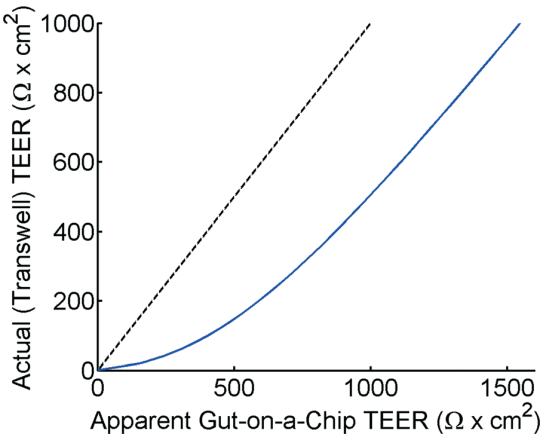

(a) Correction function applied to the measured values.

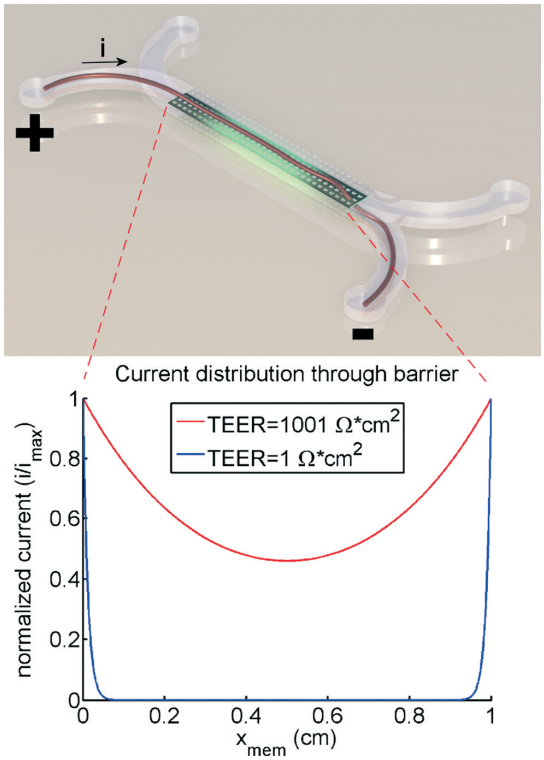

(b) Current distribution through the barrier dependent on actual TEER value.

Figure 1.15: TEER analysis by Odijk *et al.* Adapted from [32]

They implemented their theoretical analysis in studying gut barrier Caco-2 cells cultured on porous PDMS membranes using the same microfluidic design published previously [33]. The device was used only for DC measurements with Ag/AgCl electrodes, although their analysis is extendable to AC as well, which also enables use of alternative, inert electrode materials.

A versatile TEER measurement OoC device utilizing large electrodes, Walter *et al.* - 2015

As is already apparent from the previous models, TEER is commonly assessed using highly nonlinear measurements dependent on electrode positioning and electrode size. To reduce the influence of this, Walter *et al.* fabricated a 'versatile lab-on-chip' [34], which consists of two parallel microfluidic channels fabricated in PDMS.

The channels are separated by a low-porosity track-etched PET membrane (0.45μm pore size, 23μm thick). The low porosity membrane is chosen due to favourable optical characteristics, neglecting the physiological relevance. The channels are completely covered with glass slides on top of which a 25nm transparent gold film is sputtered and patterned to form a four-probe setup. Due to the relatively high transparency of electrodes (around 60% for 25nm gold film in the visible spectrum) both uniform current density and reasonably good visibility are achievable (under phase contrast microscopy). Device assembly schematic is shown in Figure 1.16.
The authors also report testing the use of ITO electrodes, but because of patterning difficulties in their laboratory they are only tested in a two-probe setup in which their performance is poor due to high intrinsic resistance.
The device was tested by culturing Caco-2 gut barrier cells, A549 lung epithelial cells and hCMEC/D3 brain endothelial cells (as well as a brain cell co-culture). In all cell cultures, barrier formation is verified through fluorescent staining for junction proteins, permeability measurement and by evaluating TEER at DC using an EVOM2 Voltohmmeter. As demonstrated in previous models, in their device a clear influence of shear stress on barrier integrity is shown.

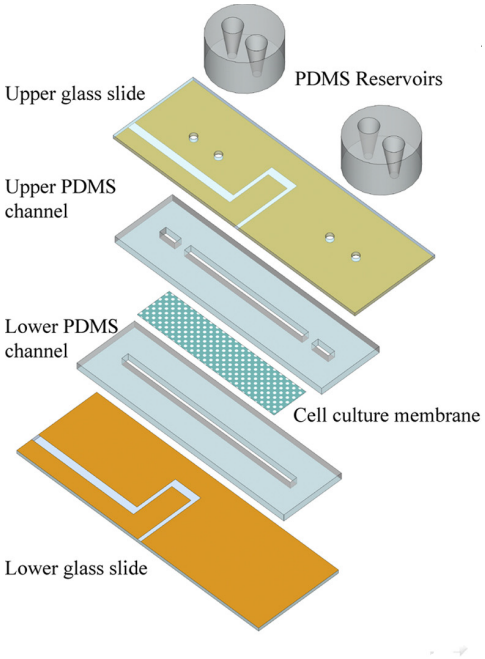

Figure 1.16: Versatile lab on chip fabricated by Walter *et al.* Adapted from [34].

Shear-free microfluidic BBB-on-a-chip - Wang *et al.*, 2017

In contrast to the previous models, Wang *et al.* developed a nearly shear-free microfluidic device through geometrical optimization of the channels (by modifying step chamber height h_{sc} in Figure 1.17b) [35]. This was done to illustrate the potential of BMECs derived from human induced pluripotent stem cells (hiPSCs) in forming a strong blood-brain barrier *in vitro*. Inspired by the EndOhm chamber they placed four Ag/AgCl electrodes directly above and below the membrane area. Gravity driven fluid flow was achieved by a rocking platform, such that it provides physiologically relevant perfusion.
After co-culturing BMECs (derived from hiPSCs) with rat astrocytes they have demonstrated highest obtained TEER values which consistently exceeded 2000 $\Omega \cdot cm^2$ (measured at DC with a Millicell-ERS Voltohmmeter), comparable to *in vivo* values. Fluorescent tracer permeability and immunofluorescence confirmed these values. Because of gravity driven flow, the device also does not suffer from potential air bubbles forming in the channel which are destructive to cells (a known issue in pump based systems).

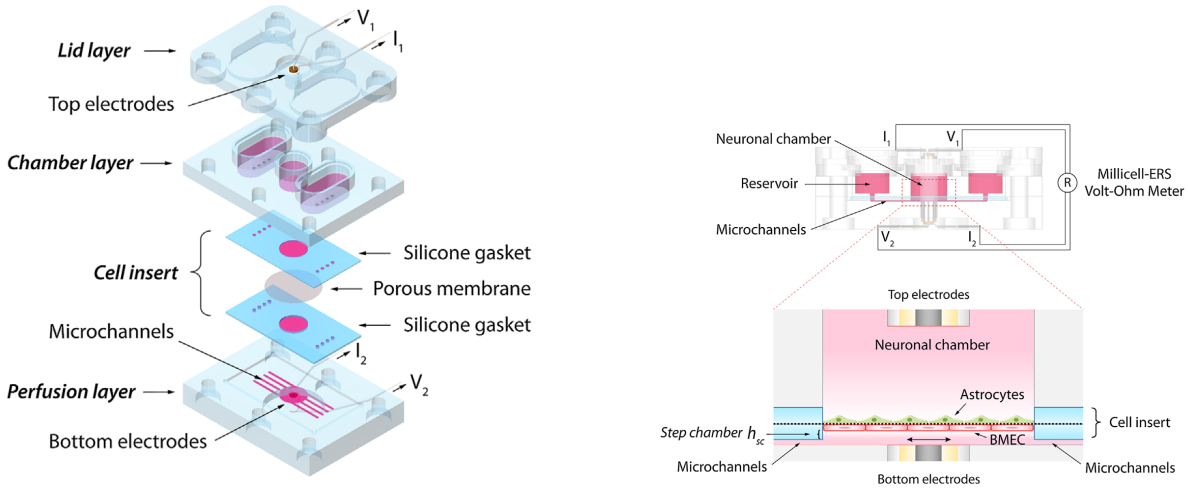

(a) Assembly schematic of the device.

(b) Cross section of the device.

Figure 1.17: Shear-free BBB device fabricated by Wang *et al.* Adapted from [35].

Integration of EIS for gut barrier assessment - Henry *et al.*, 2017

To address the need for repeatable TEER/EIS measurements, Henry *et al.* developed a gut barrier impedance spectroscopy device with integrated sputtered 25nm transparent gold electrodes [36]. The device channels were made from PDMS and they were separated by a porous 0.4μm pore size PET membrane. Device assembly is shown in Figure 1.18a.

The device was tested on human epithelial lung cells and Caco-2 gut epithelial cells. Impedance spectroscopy data was measured continously on both cell cultures and it was fitted to an equivalent circuit consisting of a paracellular resistance (TEER) and a constant phase element representing capacitive behaviour, as it better fitted experimental data. TEER was determined by subtracting total impedance (impedance at low frequencies) from medium resistance (impedance at high frequencies).

Authors report their TEER values in Ω and not the conventionally used $\Omega \cdot cm^2$ as they note that the current distribution through their device is non-uniform due to use of small electrodes and therefore simply multiplying resistance by membrane area would be erroneous.

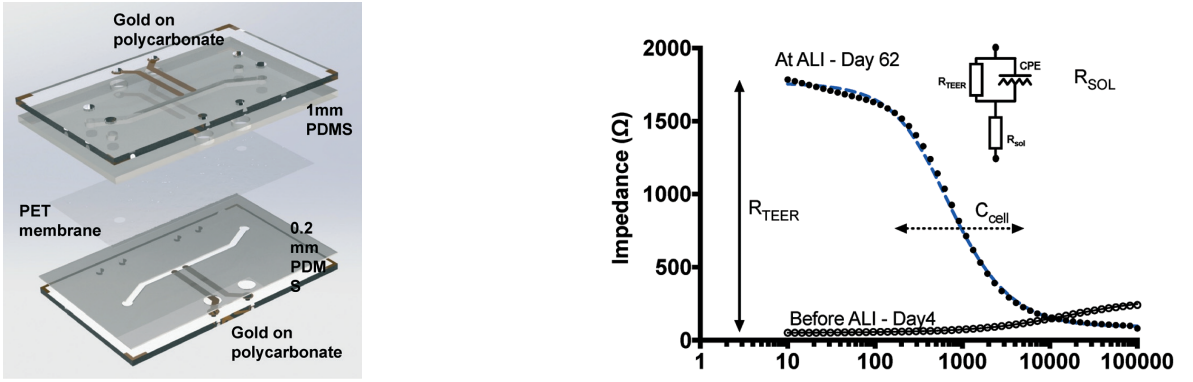

(a) Assembly schematic of the device.

(b) Impedance spectroscopy measurement of epithelial lung cells before and after exposure to air liquid interface (ALI).

Figure 1.18: TEER device fabricated by Henry *et al.* Adapted from [36].

Further work on TEER measurement standardization - van der Helm *et al.*, 2019

Continuing on the previous work regarding TEER standardization [32], van der Helm *et al.* extended the analysis to the work of Henry *et al.* (shown in Figure 1.18a) in order to correct the TEER evaluation error due to non-uniform current distribution in their device [37]. They proposed a lumped element electrical modelling scheme of microfluidic channels to study current, potential distribution and sensitivity distribution in order

to ultimately derive a calibration curve to normalize TEER (shown in Figure 1.19a). Using this compensation scheme, they arrive to values which are comparable to those of Transwell assays (shown in Figure 1.19b). The device design of Henry *et al.* was also extended to a six electrode configuration, as a proof of concept that their analysis can be extended to an arbitrary electrode configuration.

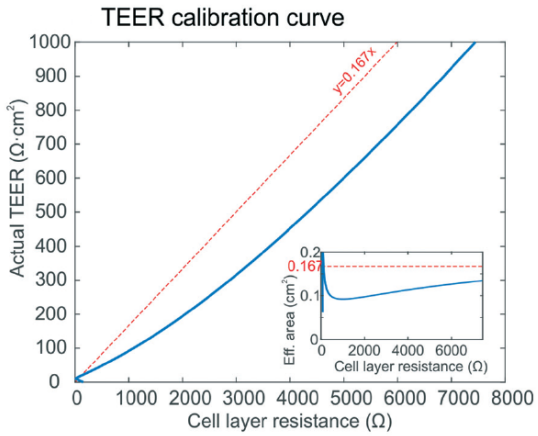

(a) TEER calibration curve (insert showing effective conduction area, dependent on TEER value).

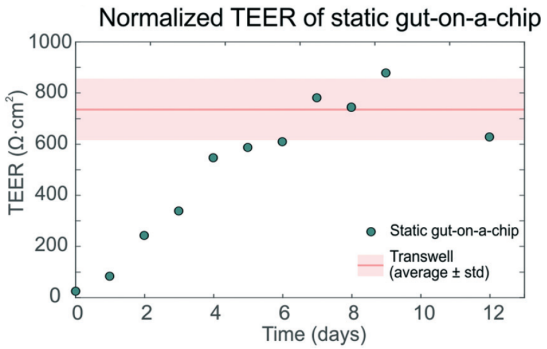

(b) Calibrated TEER shows similarity with Transwell assays.

Figure 1.19: TEER analysis results by van der Helm *et al.* [37]. Adapted from [37].

Silicon nitride based BBB model for studying nanoparticle transmigration - Mossu and Rosito *et al.*, 2019

To facilitate further research in endothelial barrier crossing mechanisms, Mossu *et al.* developed the first blood-brain barrier model which utilizes a nanoporous silicon nitride (NPN) membrane [38].

In the particular case of blood-brain barrier, previous models have shown the importance of cell co-cultures in order to form a functional neurovascular unit. When polymer membranes (either track etched or lithographically patterned) are used, their micrometer thickness is not physiologically relevant. Furthermore, the pore size in these membranes is on a micrometer scale with large pore spacing, creating 'artificial chimneys' [39] through which small molecules can pass through the membrane.

Their device consists of two perpendicular microfluidic channels separated by an NPN membrane. As they show, CD34+ stem cell derived ECs adhere on the membranes with the onset of flow and differentiate to brain microvascular ECs in presence of pericytes. However, due to their device configuration, TEER measurements were not conducted.

Other nanoporous membrane BBB models followed soon after this, including a dual-scale membrane model

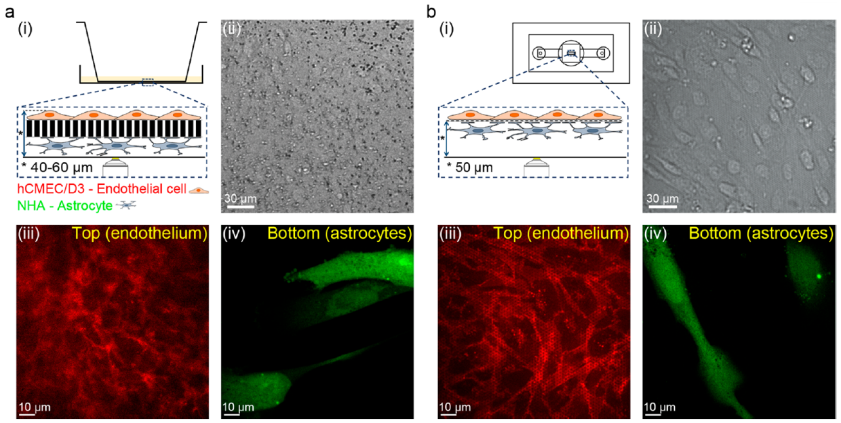

Figure 1.20: Comparison between imaging capabilities of a Transwell track etched membrane (a) and nanoporous nitride membrane (b). Adapted from [40].

(which incorporates both nanoscale and microscale pores) for studying leukocyte transmigration [39] and a model for studying nanoparticle transmigration [40] (as nanoparticles show a promising way for delivering remedies for neurodegenerative diseases), both with high resolution imaging characteristics, which are highly desired by biologists.

Influence of SARS-nCoV-2 on BBB using OoC technology - Buzhdygan *et al.*, 2020

Last but not least, Buzhdygan *et al.* fabricated a hydrogel based microfluidic BBB model which gives insight on how SARS-CoV-2 virus impacts the integrity of blood-brain barrier [41], a highly relevant topic at the time of writing. In their research they have assessed paracellular permeability by measuring TEER values (using an ECIS system) and using fluorescent tracers. They have discovered that BBB permeability is modulated by exposure to SARS-CoV-2 spike protein, which makes it possible for the virus to cross the endothelial barrier and infect brain tissue. Their research could give a possible explanation on neurological impact of COVID-19 reported in some clinical cases.

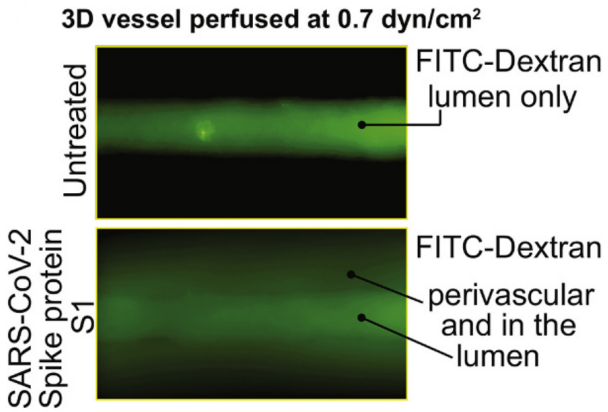

Figure 1.21: FITC-dextran (4kDa) passing through the endothelial barrier when exposed to SARS-CoV-2 spike protein. Adapted from [41].

Although not significantly relevant for impedance spectroscopy of physiological barriers, this research further shows the potential of OoC technology which can facilitate faster disease modelling and drug development, regardless of whether it is used for rare diseases requiring personalized medicine or widespread diseases affecting millions of people.

2

Design Aspects

As was already seen in Section 1.2, the goal of OoC technology is to create as accurate as possible in vitro tissue models so that they are effectively mimicking in vivo behaviour while still being able to incorporate other features that facilitate biological and pharmaceutical research (e.g. different sensors/actuators, optical transparency, etc.). Following this paradigm, a number of design aspects need to be taken into account when modelling physiological barriers. These can be divided into either design choices which ensure a physiologically relevant cell culture environment (choice of static or dynamic cell cultures and the choice of cell separation membrane) or design choices which ensure a high quality TEER measurement (choice of electrode material, size and position).
In this chapter, the different design aspects will be addressed in order to arrive to a set of design options and constraints which will be used for the device created in the scope of this thesis.

2.1. Design choices for modelling barriers

2.1.1. Static or dynamic cell cultures

As seen in Figure 1.12, traditional method for culturing cells is on stiff substrates which can be either porous (in the case of a Transwell substrate) or non-porous (for example a collagen or artificial ECM coated Petri dish [42]). In these conditions, cells can proliferate and adhere to the underlying coated substrate.
However, lack of fluid flow or other mechanical stimuli on cells (e.g. peristaltic movements in epithelial gut cells) creates a considerable dissimilarity compared to the in vivo counterpart. It has been repeatedly shown that cells of different tissues change their phenotype in response to mechanical stimuli such as shear stress [29][33]. In the case of vascular barrier cells, this corresponds to morphological changes, reorganization of cytoskeleton, proliferation, enhanced cell signaling, etc. [12]. In intestinal epithelium, shear stress on cells results in formation of villi (shown in Figure 2.1) which in turn increases the surface area that can be used for exchange of nutrients [33].

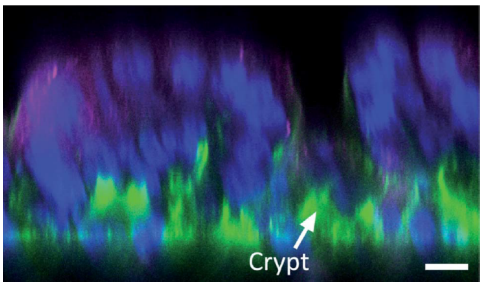

Figure 2.1: Villi formation in gut on a chip. Adapted from [33].

It therefore comes as no surprise that novel OoC devices that are used to model barriers are almost exclusively microfluidic devices in which wall shear stress determination is an important parameter.
In a channel with a rectangular cross section, shear stress can be calculated as [43]:

$$\tau_w = \mu\left(\frac{6Q}{wh^2}\right)\left(1+\frac{h}{w}\right)f^*\left(\frac{h}{w}\right) \tag{2.1}$$

where μ is the fluid viscosity, Q is the volume flow rate, h is the channel height, w is the channel width. f^* is defined as:

$$f^* = \left[\left(1+\frac{1}{x}\right)^2\left(1-\frac{192}{\pi^5 x}\sum_{i=1,3,5}^{\infty}\frac{tanh\left(\frac{\pi}{2}ix\right)}{i^5}\right)\right]^{-1} \tag{2.2}$$

In the case when the channel is much wider than it is high, i.e. $w >> h$, the shear stress expression simplifies to:

$$\tau_w = \mu\left(\frac{6Q}{wh^2}\right) \tag{2.3}$$

Nowadays, shear stress values are verified through finite element modelling (FEM), as microfluidic devices grow in complexity [35].
The value of shear stress that fluid flow exhibits on cells in OoC devices varies a lot in literature, although the common consensus is that shear stress on endothelial cells of the blood-brain barrier should be in the range of 0.3-2 Pa for accurate mimicking of brain microvasculature [12].

2.1.2. Membrane materials

One of the most discussed design questions in modelling physiological barriers is the choice of a separation membrane [44]. In the case of blood-brain barrier in vivo, an explicit membrane does not exist, rather the membrane functionality is performed by the basement membrane separating endothelial cells from glial tissue and it is formed by the cells themselves from a matrix of proteins [12].
Efforts have been made in cell sheet engineering to develop a method on cultivating cell sheets which are able to produce all of the in vivo features in vitro [45]. These cell sheets are then transferred and can be used as the closest in vivo replicate for research. Even though these solutions sound compelling, to this date they are hardly reproducible and are limited to small-scale laboratory use.
For these reasons, other artificially produced porous membranes are still used as they are based on proven technology that is able to produce membranes on a large scale.
In order to mimic tissue physiology, two main categories of materials are used as membranes nowadays: polymer membranes and silicon-based membranes. In the following paragraphs each of the two categories will be briefly explained. Additionally, even though they do not fall in the membrane category, the use of hydrogels for creating 3D cell cultures will be shown, in which cells are not separated by an artificial membrane.

Polymer membranes

Polymer membranes are the most commonly used membranes in biological research [46]. In static cultures cultivated in Transwells, membranes are most commonly created using ion track etching of polycarbonate (PC), an etching technique in which heavy ions bombard the surface of a polymer causing polymer chain degradation (called chain scission) in the places on the polymer sheet which were bombarded [47]. This makes the polymer's chemical etch rate increased, meaning that chemical etching can be used to open the pores. The size of the pores can be controlled by changing chemical etching parameters and the pore density can be controlled by controlling the ion-beam. This technique enables rapid and cost-effective production of porous membranes down to submicron pore openings, but as ion track etching is a stochastic process, pore density is limited before pore openings begin to overlap, as shown in Figure 2.2.
Pore-to-pore distance can also be an issue as non-porous openings can be so large that some cells cannot achieve uniform cell-cell communication with co-cultured cells on the other side of the membrane [39].
Therefore structured porous polymer membranes are gaining more popularity despite their more difficult fabrication. These membranes are made from materials like polydimethylsiloxane (PDMS), parylene, polymethyl methacrylate (PMMA), polycarbonate (PC) and more. From the mentioned ones, PC membranes are successfully commercialized and PDMS is used most recently, due to its favourable properties like optical transparency, similarity of mechanical properties to tissue (comparable Young's modulus in the range of kPa to MPa), low cost and ease of preparation using soft lithography [44].
A significant drawback of PDMS and other soft hydrophobic polymers is adsorption of different small molecules including drugs, making it difficult to use in drug studies without additional specialized surface coating [49].

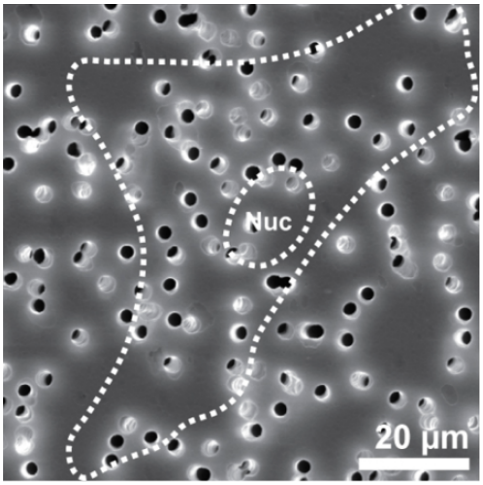

Figure 2.2: Overlapping 3.0 μm pores in a track etched membrane. Adapted from [48].

Silicon-based membranes

Silicon-based (polysilicon, silicon oxide, silicon nitride) membranes have been used extensively in micro-electromechanical systems (MEMS) for development of different transducers [50].
More recently, their use has been introduced in OoC applications, particularly for the modelling of blood-brain barrier. As free standing silicon-based membranes can be fabricated at nanometer-scale thicknesses while maintaining sufficient mechanical strength, they might represent a better in-vitro representation of the nanometer-scale thin basement membrane [51], enabling better cell-cell communication inside the neurovascular unit.

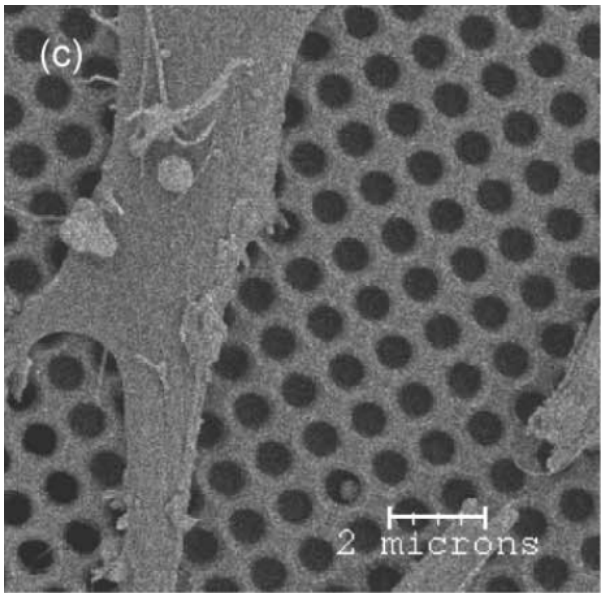

Figure 2.3: Astrocytes cultured on a 600nm pore size silicon nitride membrane. Adapted from [52].

Nevertheless, silicon-based thin film membranes also exhibit very high Young's modulus (in the order of hundreds of GPa), which is not physiologically relevant. However, an interesting effect was found in membranes which contain a large number of sub-micrometer scale pores with a high pore density, where endothelial cell layers start to express similar behaviour as if they were cultured on a PDMS substrate which has a considerably lower Young's modulus [48]. More specifically, cells on a nanoporous SiO_2 substrate exhibit lower number of cell-substrate focal adhesions and promote formation of tighter cell-cell junctions. In this way, pore density can modulate and promote tissue and barrier formation. Another consequence of using nanoporous

thin transparent membranes is that light scattering under microscopy becomes small compared to microporous polymer membranes, enabling superior studies of nanoparticle transmigration through BBB [40].

Hydrogels

Hydrogels form a group of materials characterized by a 3D-crosslinked hydrophilic polymer network, which makes them able to absorb and retain water [53]. In cell biology applications, they are gaining increasing interest as cells can be cultured in a 3D network, which if the hydrogel is made from a matrix of ECM proteins (such as collagen) presents the closest mimic to an in vivo environment [54]. The cells are typically embedded in a liquid hydrogel at room temperature which upon heating to 37°C forms a gel [55]. In certain cases such as studying of angiogenesis (formation of blood vessels), use of a 3D cell culture suspended in a hydrogel is the only viable way that the process will occur [56].
However, many technical challenges arise with use of hydrogels as cell retrieval from them is more difficult, imaging due to light scattering can in some cases be impossible (if the layer is very thick) and the models are significantly more difficult to replicate [57].
Nevertheless, by clever use of fluid mechanics hydrogels are enabling 3D microfluidic tissue models in which no membrane needs to be present. This is achieved through the use of phaseguides (capillary valves). A phaseguide is a line of material or a change in geometry that spans the complete length of a liquid–air boundary [58]. By applying phaseguides in a microfluidic channel, hydrogels (which may contain cells) can, once inserted in the microfluidic channel, be held only by capillary forces. In this way, cells can be constrained within the hydrogel and can freely interact with the perfusing fluid in a separate channel [59]. The use of this technology is commercialized by the biotechnology company MIMETAS and an example of the use of this technology for culturing Caco-2 cells in a membrane-free environment is given in Figure 2.4 (in the example no cell co-culturing is done, so ECM-gel does not have other cell types).

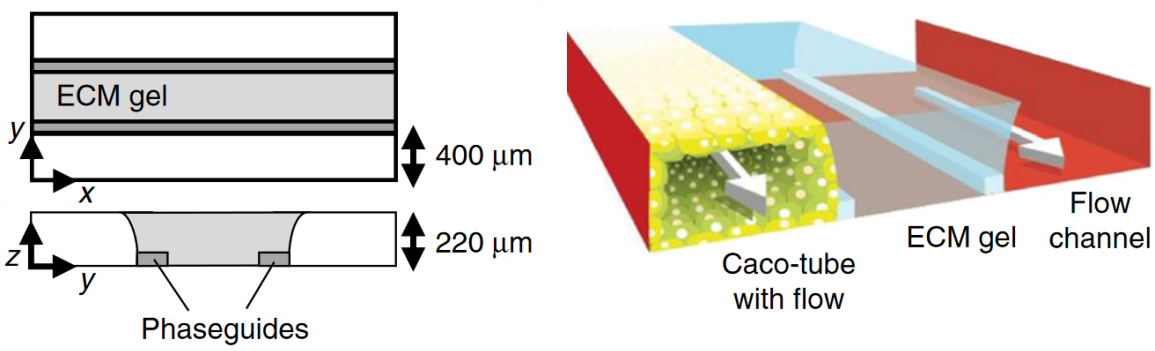

Figure 2.4: Culturing Caco-2 cells in a membrane-free environment through use of phaseguides and ECM-gel. Adapted from [60].

2.2. Design choices for monitoring TEER

2.2.1. Electrode materials

In order to achieve TEER measurement functionality, electrodes need to be placed inside a microfluidic device. Apart from the influence of size and position of electrodes shown in previous section, electrode material choice is also an important parameter to consider. In Figure 2.5 the formation of a double-layer capacitance at the electrode-electrolyte interface is shown and its parameters are directly dependent on the choice of electrode material. Due to its existence, a current can only flow if the double layer capacitance is bridged, either through an electrochemical interaction between the electrode and electrolyte (such as in Ag/AgCl electrodes), through the use of an AC signal (used in electrodes made of inert materials) or through EDL breakdown, which is generally an unwanted effect in sensing devices as it can interfere with measurements and potentially even be destructive to the measurand.

Ag/AgCl electrodes

The conventional setup for measuring TEER values in Transwell assays uses STX2 Ag/AgCl electrodes (also referred to as chopstick electrodes [27]) shown in Figure 1.12 for applying current through the cell layer and sensing the voltage.

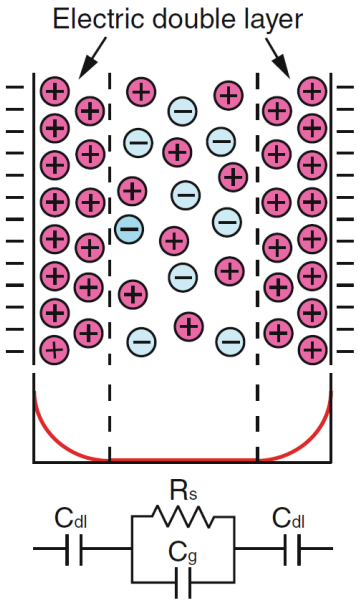

Figure 2.5: Formation of double layer capacitance. Adapted from [61].

Ag/AgCl electrodes are used since they are able to conduct DC current as there is (ideally) no formation of double layer capacitance normally present at the electrode-electrolyte interface i.e. they are non-polarizing. This effect is due to an electrochemical redox reaction happening at the electrode surface once it is immersed in an electrolyte [62]:

$$AgCl_{(s)} + e^{-} \longrightarrow Ag_{(s)} + Cl^{-} \tag{2.4}$$

which enables charge transfer from ionic conduction inside the electrolyte to electron conduction inside the metal conductor (faradaic current). The standard reduction potential of the electrode is also well defined and it is equal to $E^0 = 0.222V$.
Ag/AgCl are commonly used as (pseudo)reference electrodes in electrochemical systems as their potential when immersed in a solution does not change, which enables stable characterization of other materials [62].

Inert electrodes

Another group of electrodes that can be used in OoC devices are electrodes made of inert materials such as Au, Pt, TiN, etc. At the electrode-electrolyte interface no chemical reaction takes place when using these electrodes without a significant overpotential. If the potential is increased so that a faradaic DC current can flow (current due to redox reactions), there is a risk of water electrolysis and formation of bubbles, local increase of heat and change of pH value, all of which are undesirable effects in an OoC device as they can be detrimental to the cell culture.
However, if the device is used in AC measurements current can still flow as the double layer capacitor is effectively shorted [32]. Furthermore, electrodes made of inert materials are more common in standard cleanroom processing, making them a suitable alternative to the commonly used Ag/AgCl electrodes for microfluidic devices with integrated electrodes.

2.2.2. Error sources in determining TEER

Tetrapolar (i.e. four-probe) measurement systems are arguably the most commonly used systems in bioimpedance measurements as they eliminate most issues that arise due to intrinsic impedance of electrodes and formation of the double-layer capacitance at electrode-electrolyte interface [63].
However, due to a higher number of electrodes, positioning of current-carrying (CC) and pick-up (PU) electrodes relative to each other can have a significant influence on measurement results. In this section, a mathematical model will be explained that gives more elaborate insight on how electrode positioning influences bioimpedance measurement.

Sensitivity analysis

Figure 2.6 shows a four-probe measurement setup for measuring impedance of an arbitrary volume. If a current is applied between current-carrying (CC) electrodes and it flows through the volume, it will flow with varying current densities at different volume fractions dV. If the volume is of homogeneous resistivity, highest current density will be at the shortest path between the two electrodes (path of least electrical resistance) and dropping as the conduction path length increases. Measured voltage is then the potential difference that is sensed by the pick-up (PU) electrodes and is dependent on where PU electrodes are placed relative to CC electrodes.

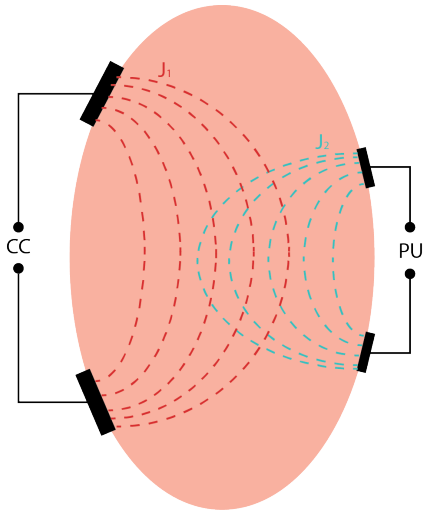

Figure 2.6: Four probe setup measuring an arbitrary volume. Inspired by [63].

To model this mathematically, a current $I_{applied}$ is applied between CC electrodes and its density J_1 is calculated in the volume. Then, a current of same magnitude is applied between PU electrodes and a new current density J_2 is calculated.
Sensitivity factor S is then defined as [63]:

$$S = \frac{\boldsymbol{J_1} \cdot \boldsymbol{J_2}}{I^2_{applied}} \tag{2.5}$$

and it represents the measure by which the two current densities are 'in line' with each other (normalized over applied current). The measured impedance is then:

$$Z = \int_V (\rho_R + j \cdot \rho_I) S dV. \tag{2.6}$$

where ρ_R and ρ_I are real and imaginary components of complex impedivity, respectively. As can be seen from Equation 2.6, measured impedance is dependent on sensitivity in the particular volume fraction, implying that not all volume fractions contribute equally to the apparent impedance. This equation also gives explanation to an interesting and perhaps counter-intuitive phenomena that can occur, where the the scalar product of two current densities in a volume fraction is negative, meaning that by applying a larger current, measured impedance of that volume fraction is decreased.
Another problem that can occur is that the two current densities are in opposite direction in a volume fraction. This would make the apparent impedance of the volume equal to zero, which does not mean that the volume is a good conductor, but rather that PU electrodes cannot sense the impedance contribution of that volume fraction.
In a two-probe system, CC and PU electrodes are physically the same meaning their current densities are the same (in direction and magnitude) so these unwanted effects cannot occur.
Equation 2.5 is in membrane-separated models commonly normalized to membrane area so that sensitivity is a unitless value, equal to unity in case the impedance contribution of the volume fraction is neither over- or underestimated:

$$S_{norm} = \frac{\boldsymbol{J_1} \cdot \boldsymbol{J_2}}{I^2_{applied}} \cdot A^2 \tag{2.7}$$

Geometric correction factor

In a TEER measurement device, resistivity between electrodes is not homogeneous as there is (in the simplest model) at least one cell type and the surrounding cell medium, with each have their own resistivities (TEER being the resistance of the cell layer). Depending on the cell type and the confluence of the layer it forms, TEER value changes which can result in a change of current density in different volume fractions, as current flows along the path of least resistance. Because of this, sensitivity can not only be dependent on electrode geometry, but also on the TEER value being measured. Influence of these parameters is shown in Figure 2.7. To compensate for errors that occur due to uneven sensitivity distribution, Yeste et al. [64] suggested the use of a geometric correction factor (GCF) for both Transwell and microfluidic models. The GCF is defined as:

$$GCF = \frac{TEER_t}{TEER_s} \tag{2.8}$$

where $TEER_s$ represents a TEER value measured by the electrode configuration (inside a simulation) and $TEER_t$ the theoretical TEER value which should be measured in the ideal case (input parameter for the simulation). The measured TEER value should be multiplied by GCF (which is also a function of measured value) in order to arrive to the correct TEER value:

$$TEER_{GCF} = (R - R_{blank}) \cdot A \cdot GCF \tag{2.9}$$

It is important to realize that in systems where sensitivity of cell layer is uniform and equal to unity, GCF is similarly equal to unity.

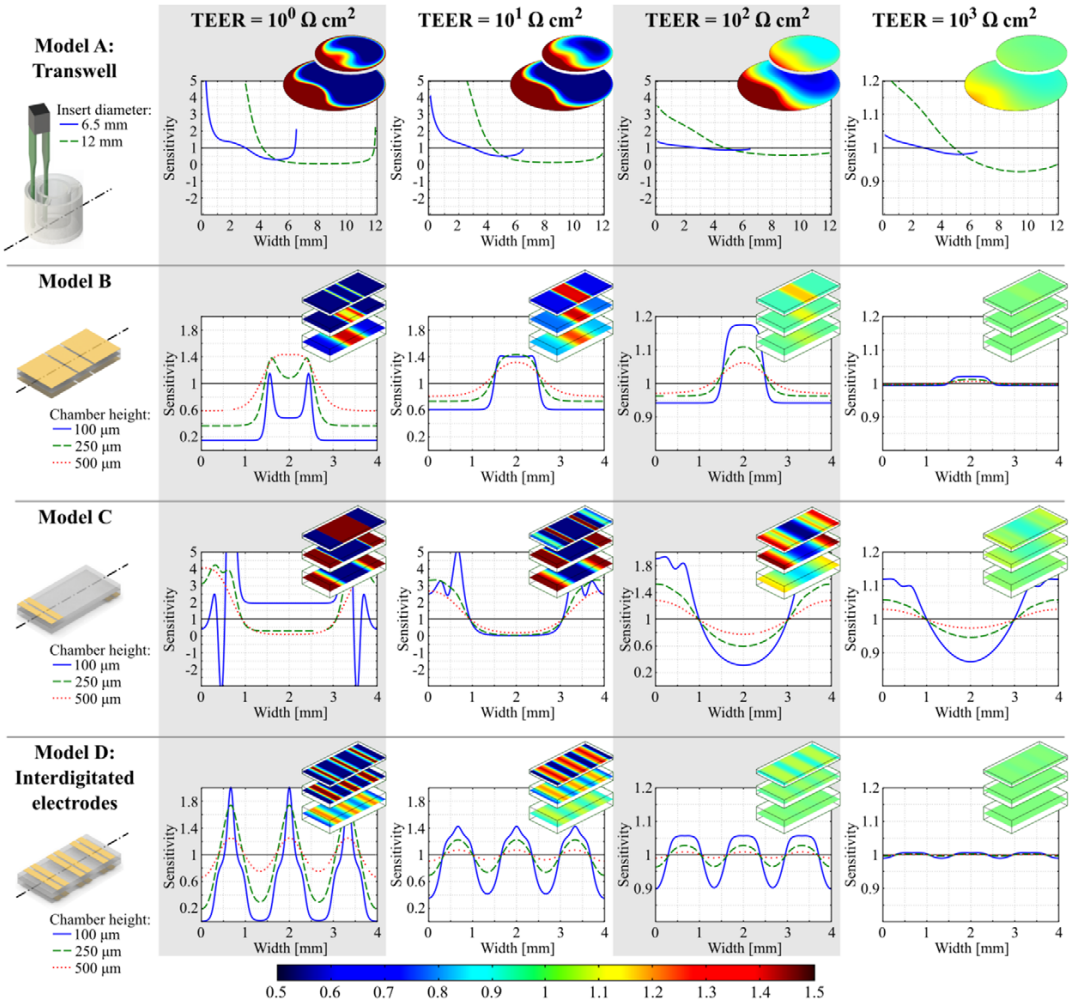

Figure 2.7: Sensitivity distribution dependent on electrode geometry, distance from membrane and TEER value being measured. Adapted from [64].

2.3. Research questions

Given the literature overview on differently designed BBB OoC models with their respective advantages and disadvantages, as well as an overview of design choices which can be taken when designing a TEER device for BBB integrity monitoring, two main points can be noticed:

1. All of the TEER/EIS measurement devices (specific for BBB or used for other tissue) reported have highly nonuniform sensitivity distributions due to poor electrode placement (which is more often than not overlooked) as shown in Figure 2.7.

2. Highly porous, ultrathin silicon-based membranes may present a better artificial mimic of the basement membrane constituting the blood-brain barrier.

The first point has been somewhat addressed by deriving correction functions specific to different electrode placements. These functions are however derived from finite element models where cell layers and the surrounding culture medium are perfectly uniform and invariant in time or space (for example a local change in cell packing density may render the correction function invalid). As cells may be subjected to different types of stimuli under biological experiments, which might change the conditions assumed when deriving correction functions (for example the cell medium conductivity or cell packing density), these functions might not be correctly used.
The second point is still a not fully answered problem in OoC development as research on silicon-based membranes (mainly silicon) for BBB-on-chip applications is scarce (presumably due to resource-intensive fabrication, compared to polymer-based membranes). Therefore, as the Else Kooi Laboratory (EKL) where the device will be fabricated has technological capabilities required for processing these materials, it was decided to further facilitate research in this domain.
With these observations in mind, several research questions can be formulated:

- How can a TEER/EIS measurement, microfluidic OoC device be designed with highly uniform sensitivity, without compromising transparency?

- How to fabricate a two-channel microfluidic device separated by a porous ultrathin silicon nitride membrane, in a reproducible, wafer-scale production flow? How to integrate TEER/EIS measurement functionality in such a device?

These broad research questions offer a lot of flexibility in design, but design constraints were placed and are summarized in Table 2.1. Out of these, only the choice of titanium nitride electrodes has not been explained in prior text. Titanium nitride is the only available electrode material in EKL which is chemically inert and is CMOS-compatible, therefore making it usable without any processing constraints.

Table 2.1: Design choices.

Aspect	**Type**	**Characteristics**
Membrane	Silicon nitride	nm-scale thickness, high porosity, sub-500nm pore size, high transparency, high Young's modulus
Electrode material	Titanium nitride	inert material, no conduction at DC
Electrode configuration	4-point	influence of EDL capacitance and electrode impedance is reduced, measurement dependent on positioning
Cell culture	dynamic	inclusion of shear stress on EC

3

Device Design

3.1. Electrode positioning

As was seen from the previous section on error sources in determining TEER, electrode placement is critical in any four-probe impedance measurement system. Without considering it, any comparison between TEER values obtained by different OoC devices is inherently invalid. What's more, even in several seemingly identical OoC devices, device-to-device values can be vastly different if the electrode positioning is such that it does not tolerate manufacturing imperfections. For these reasons, electrode positioning must be considered early in the design of a TEER measurement device.

As was seen in Chapter 2, measurement nonlinearity in four-probe systems can generally be solved by two methods: use of large electrodes which cover the whole cell culture [29] or use of small electrodes and a mathematical fitting function which corrects for the nonlinearity [37].

The first method is generally simple to implement in polymer-based models using electrodes deposited by physical vapour deposition (PVD), however it has a significant drawback of using semitransparent electrodes made from thin (usually few tens of nanometers) layers of Au or a similar material. These electrodes are limited in transparency making the device difficult to use in bright field microscopy.

The second method uses finite element modelling to develop a fitting function which corrects for nonuniform current distribution through the cell layer. Although it is an elegant solution with which the problem with transparency can be solved, it relies on modelling the cell culture as a single element with a distributed resistance. In an ideally uniform cell culture this would not present an issue, but in case the cell culture has any defects (which is expected in a cell culture used to model a disease), the influence of the defect might be over- or underestimated, depending on the location of the defect in respect to electrodes.

In the scope of this thesis, a goal was set to develop an electrode setup which would enable linear TEER measurements across a range of frequencies and cell culture resistances (as was seen previously in Figure 2.7, current distribution is also dependent on cell culture resistance). In order to achieve this, it is necessary to ensure a uniform current distribution at the cell layer level.

Conventionally, TEER measurement devices are made using different techniques for processing polymer materials such as injection molding, 3D printing, soft lithography, etc. As the fabrication of this device was planned to take place in the Else Kooi Laboratory, it is also possible to use a range of different techniques for Si processing, which would enable placement of electrodes in more flexible configurations.

One such configuration is the use of electrodes placed on microfluidic channel sidewalls as shown in Figure 3.1. In a microfluidic device, this construction would allow unobstructed view of the membrane and cell culture area, a highly sought-after feature in any OoC device.

A finite element model based on preliminary design (given in Figure 3.1) was developed using COMSOL. The model includes two parallel microfluidic channels (micromachined in Si) separated by a 150 nm thick SiN membrane. The membrane thickness is chosen such that it falls within the range of basement membrane thickness *in vivo* (up to 200 nm) while remaining sufficiently transparent and structurally sound. The verification of membrane stability will be conducted in Section 3.3. The microfluidic channels are 5 mm long, 300 μm high and have a variable width.

On top of the membrane a block is placed which is used to mimic the cell layer's TEER. The block has the same area as the membrane and a height of h_{cell}. Electric conductivity of the block σ_{cell} is deduced from the

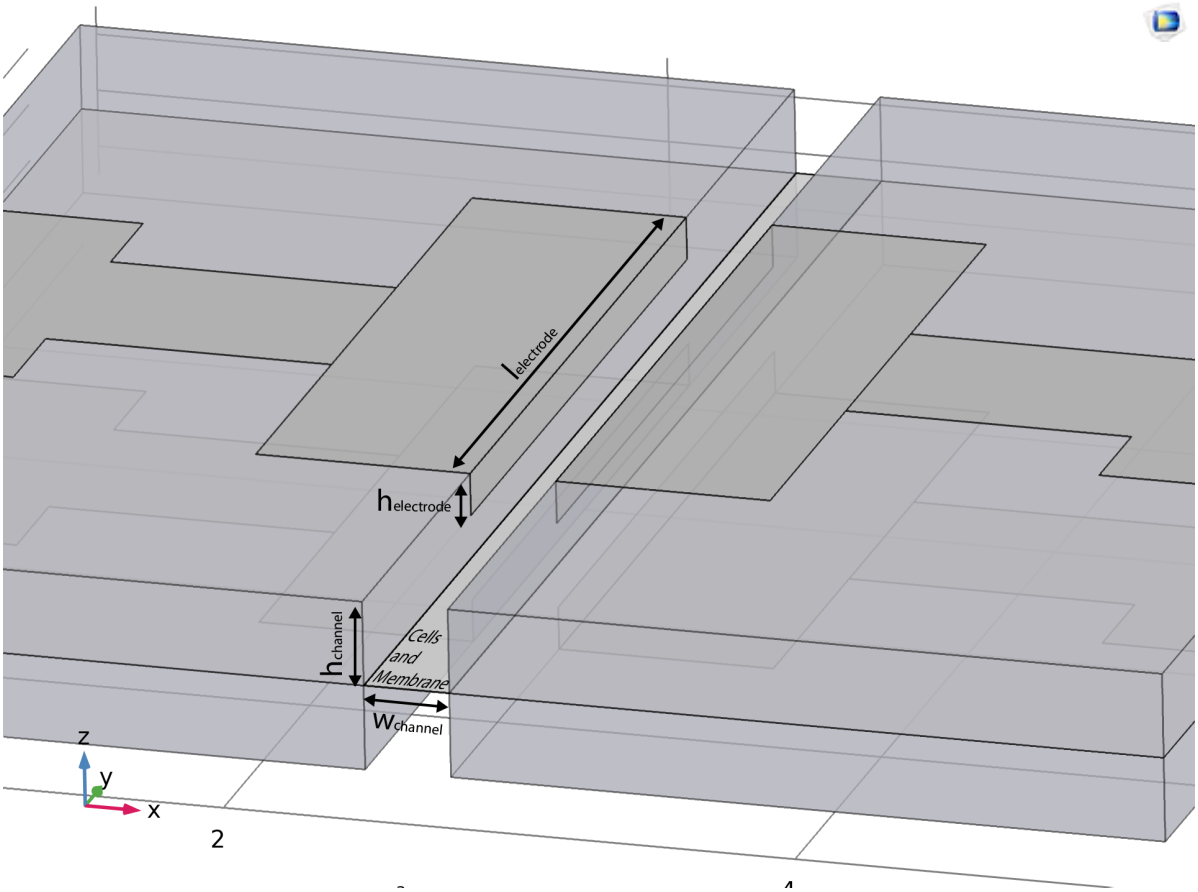

Figure 3.1: COMSOL model used for electrical simulations.

TEER value using Equation 3.1.

$$TEER = R_{cell} \cdot A_{membrane}$$

$$TEER = \frac{1}{\sigma_{cell}} \frac{h_{cell}}{A_{membrane}} \cdot A_{membrane}$$

$$\sigma_{cell} = \frac{h_{cell}}{TEER} \tag{3.1}$$

To model the capacitive behaviour at higher frequencies the relative permittivity of the block is approximated as relative permittivity of water and is equal to $\epsilon_{cell} = 80$.
Inside the channels, a custom medium is placed which electrically mimics Dulbecco's Modified Eagle Medium (DMEM), a commonly used cell medium for culturing mammalian cells. It has an electrical conductivity of $\sigma_{medium} = 1.67 S/m$ and a relative permittivity equal to water.
Once the base parameters for the model have been defined, it is necessary to derive a set of variable parameters which need to be optimized through simulation. In the case of the electrode configuration shown in Figure 3.1, these parameters are electrode height, electrode length and (as previously mentioned) channel width. As the electrodes are used in an X-shaped connection (current and voltage electrode pairs are on diagonally opposite sides respectively), the electrode width is not important as there is no conduction through silicon.
In order to quantify how well a certain electrode configuration performs, the sensitivity factor given with Equation 2.5 is used.
In the COMSOL model two Physics modules are used: Electric Currents (ec) and Electrical Circuit (cir). Electric Currents module is used for calculating the current density and potential distribution through the microfluidic channels. Electrical Circuit module is used to connect the device to a virtual circuit consisting of a constant current (CC) source (connected between current electrodes) and a voltmeter (connected between

voltage pickup electrodes).
In order to calculate the sensitivity factor, it is necessary to switch the electrode connections (current electrodes become voltage electrodes and vice versa) to obtain a dot product of their respective current densities. This is possible to do in two ways:

1. by running a single COMSOL Study which calculates the current density of one electrode pair, exporting the obtained current density matrix, manually changing the electrode connection, repeating the process and ultimately calculating the sensitivity factor from the two matrices

2. by running a single COMSOL Study which controls two other Studies. Each of the two Studies is configured to run its own electrode arrangement by changing the parameters of the Electrical Circuit module. The sensitivity factor is then automatically calculated by using the data from two different Studies.

In this thesis work, the second option was chosen as it is more automatized.
The model meshing is done in multiple steps, as dimensions of parts are different in many orders of magnitude. To simplify the simulation, reduce required computing power and time, electrical conductivity of the porous membrane is simulated as:

$$\sigma_{membrane} = \sigma_{medium} \cdot P \tag{3.2}$$

where P is equal to membrane porosity. Notice that electrical conductivity of Si_xN_y is neglected in the formula, as its conductivity is normally about ten orders of magnitude lower than that of the cell medium. By using this simplification it is not necessary to include pores in the COMSOL model of the porous membrane, thereby vastly reducing the rendering and meshing complexity of the simulation.
The simulation is executed both for a stationary case and a frequency dependent study. It is important to note that the stationary case result, although valuable for simulation purposes, cannot work in a realistic scenario as the model neglects the effect of EDL capacitance which would make conduction at DC impossible (in a safe manner). For this reason a frequency dependent study is conducted, as in that case the effect of EDL in a four-probe setup is negligible. The stationary case study is useful as a general indication of how well the setup will perform in a frequency dependent study (especially at low frequencies), as it is considerably faster to execute (few minutes compared to about one hour).
In Table 3.1 different settings for simulation are shown. The configurations are chosen as an illustration on how the three parameters influence sensitivity, in order to derive the final geometry.

Table 3.1: Choice of electrode configurations used for optimizing the sidewall electrode topology.

Configuration number	Electrode height (as percentage of channel height)	Electrode length (as percentage of channel length)	Channel width (as percentage of channel height)
1	1%	50%	100%
2	50%	50%	100%
3	99%	50%	100%
4	1%	100%	100%
5	1%	100%	200%

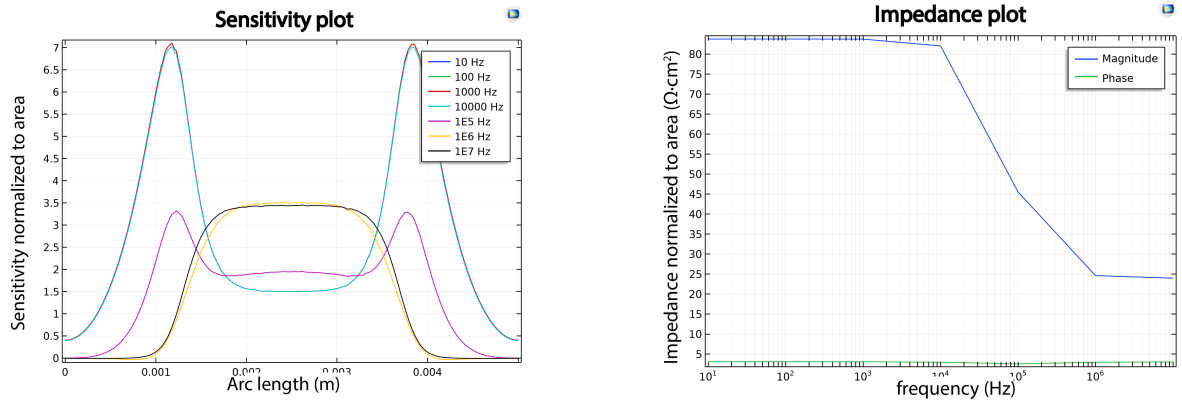

(a) (b)

Figure 3.2: Sensitivity and impedance plots (TEER = $50\Omega \cdot cm^2$) for Configuration 1.

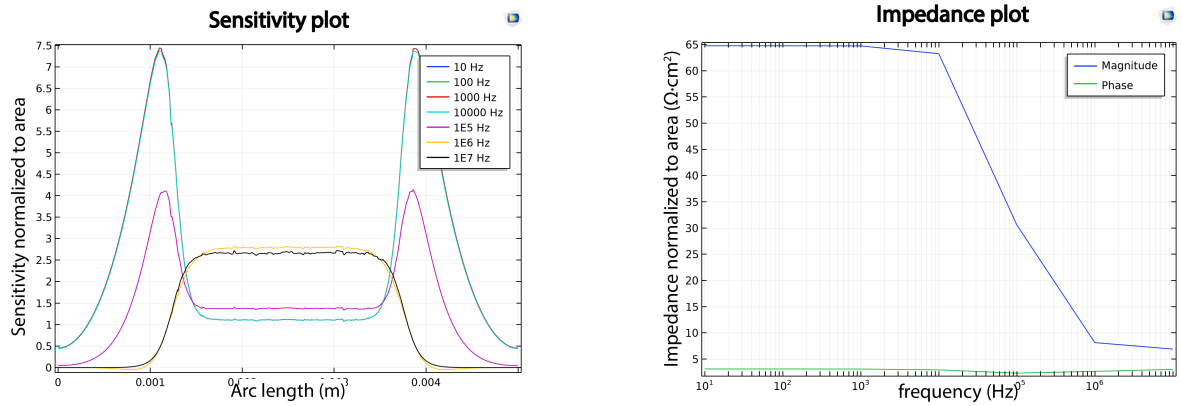

(a) (b)

Figure 3.3: Sensitivity and impedance plots (TEER = $50\Omega \cdot cm^2$) for Configuration 2.

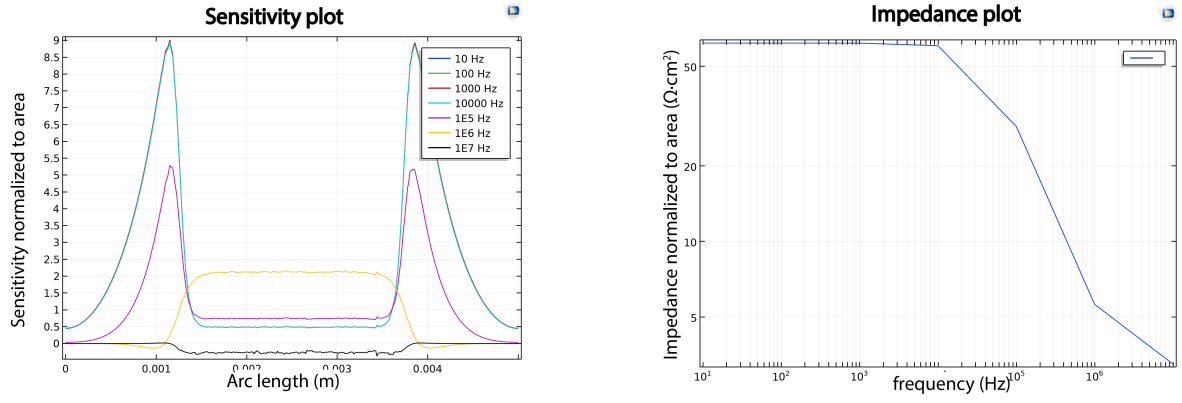

(a) (b)

Figure 3.4: Sensitivity and impedance plots (TEER = $50\Omega \cdot cm^2$) for Configuration 3.

In Configuration 1 to 3 (given in Figures 3.2 to 3.4), the influence of increasing electrode height is shown, whilst the electrode length is kept constant at half of channel length. In all three of the configurations, a large discrepancy between the curve shapes can be noticed across frequencies. Particularly, at lower frequencies (up to 100 kHz, in the case of the given curves) an increase in sensitivity is noticed in the area around the

electrode edges, in line with observations given in literature. Furthermore, with the increasing electrode height, an overall decrease in sensitivity can be noticed regardless of the frequency, due to the two current density vector fields having increasingly large horizontal components, which in a cross-connected system result in a lower dot product. With electrodes covering 99% of channel height (shown in Figure 3.4), at high frequencies the sensitivity drops below zero.
From these three configurations, two important conclusions can be taken away:

- Cells should ideally be placed in an area which does not include electrode edges as this will inevitably result in an impedance overestimation.
- Electrode height should ideally be as small as possible, whilst still having electrical contact with the cell medium, in order to minimize horizontal components in the current density distribution, at cell layer level.

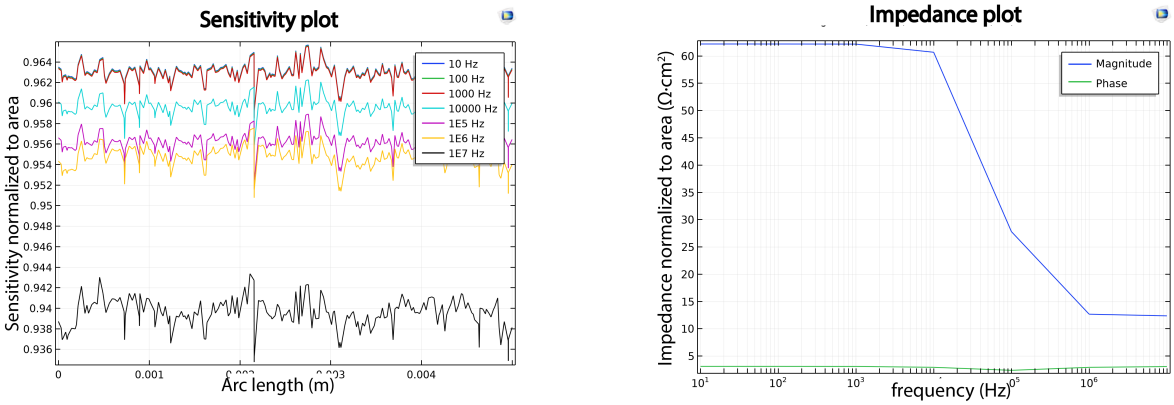

(a) (b)

Figure 3.5: Sensitivity and impedance plots (TEER = $50\Omega \cdot cm^2$) for Configuration 4.

The conclusions given above are verified in Configuration 4 (given in Figure 3.5). The electrodes extend through the full length of the channel and are placed at 1% of channel height. As can be seen, the sensitivity values are close to 1 (the ideal value) through the whole frequency range. The noise-like appearance of the curves is due to the finite meshing of the COMSOL model. This effect is also present in the previous configurations, however as the y-axis scale is larger it is hardly visible.

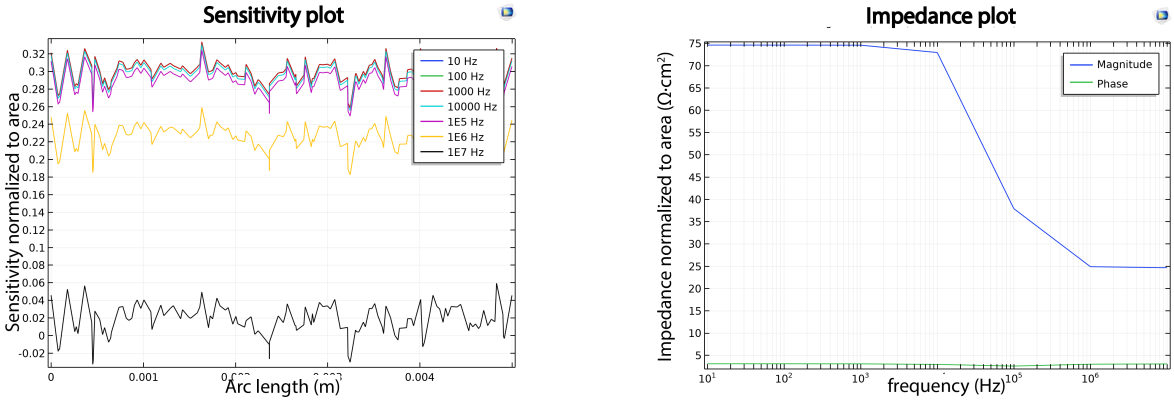

(a) (b)

Figure 3.6: Sensitivity and impedance plots (TEER = $50\Omega \cdot cm^2$) for Configuration 5.

In order to further verify the effect of horizontal current components reducing the overall sensitivity, instead of making electrodes higher, in Configuration 5 the channel's width was increased (thereby decreasing the

channel's aspect ratio ($\frac{h}{w}$)). Shown in Figure 3.6, a similar observation can be made as the one in Configurations 1 to 3, where the overall sensitivity at cell layer level is reduced approximately three-fold. However, as the electrodes extend through the full channel, the sensitivity is uniformly distributed.
Therefore, in addition to the two conclusions given above a third one can be added:

- Channel's aspect ratio ($\frac{h}{w}$) should be kept equal to or higher than 1 for achieving current density distribution with a predominant vertical component at cell layer level

Sidewall electrodes come with one main problem however, which is difficult fabrication. As illustrated in Figure 3.7, even if a defect-free transition can be achieved between the top surface and the vertical sidewall, due to limited overlay accuracy of lithography machines available in Else Kooi Laboratory (theoretical minimum for the wafer stepper is $0.5\mu m$), the feasibility of fabricating the electrodes (without destroying them in subsequent microfludic channel etching) is questionable due to small horizontal dimensions of the metal layer on the sidewall.

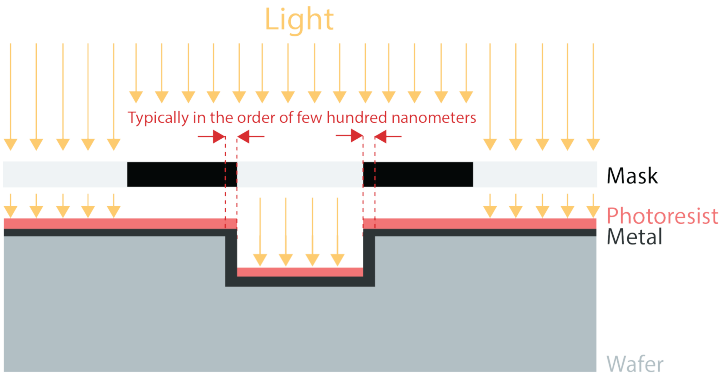

Figure 3.7: Fabrication issues associated with electrodes on vertical sidewalls.

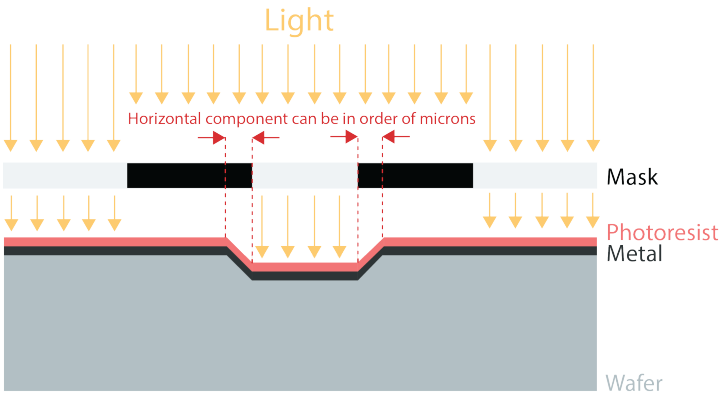

Figure 3.8: Fabrication of electrodes on slanted sidewalls.

In order to mitigate this issue, another study was done where the electrodes are placed at slanted sidewalls (shown in Figure 3.8). In this way electrodes can have a short vertical component as before (in order of a few micrometers) as well as a considerably larger horizontal component (in order of a few micrometers, instead of hundreds of nanometers), making them easier to fabricate using photolithography. The angle of the slanted sidewalls was chosen to be 54.7°in respect to the top surface. The reason for this is that this is the angle between <100> and <111> planes of crystalline silicon. If the opening is etched using anisotropic wet etchants of silicon such as tetramethylammonium hydroxide (TMAOH) or potassium hydroxide (KOH), sidewalls with these characteristics can be fabricated. As seen in Figure 3.9, the sensitivity distribution of this solution almost equal to the one given in Configuration 4 (shown in Figure 3.5) whilst ensuring a high fabrication feasibility.
The plots in Figures 3.2 through 3.9 are concerning only frequency dependent sensitivity which is calculated along a line that goes through the channel's center longitudinally, at the cell layer level. This is done to easily

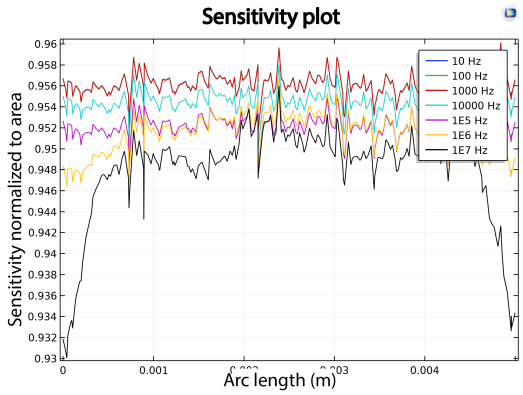

(a)

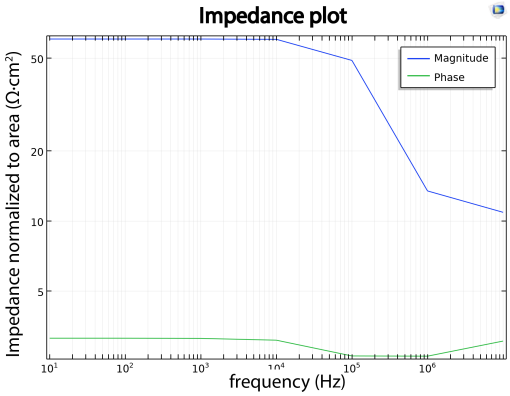

(b)

Figure 3.9: Sensitivity and impedance plots (TEER = $50\Omega \cdot cm^2$) for electrodes on slanted sidewalls.

illustrate the effect of increasing frequency, but does not show how the sensitivity behaves across channel width. In Figures 3.10 and 3.11, the sensitivity distribution across the full membrane area is shown. The sensitivity is again close to unity across the full area and across frequencies.

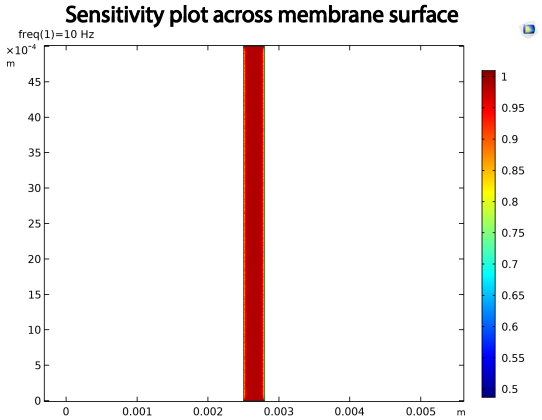

(a) Full membrane view.

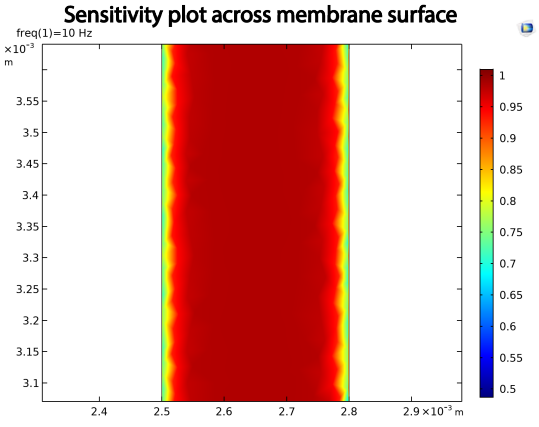

(b) Zoomed in view.

Figure 3.10: Sensitivity across the full membrane area for electrodes on slanted sidewalls at 10 Hz.

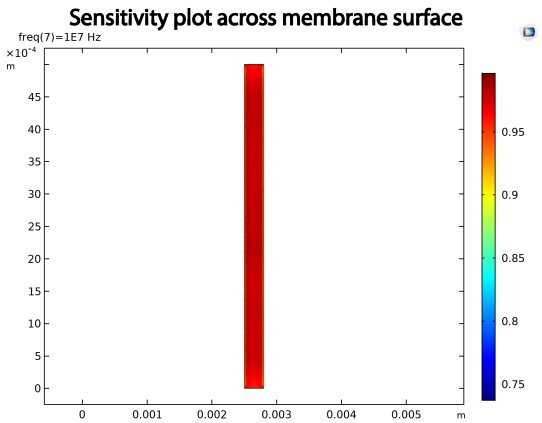

(a) Full membrane view.

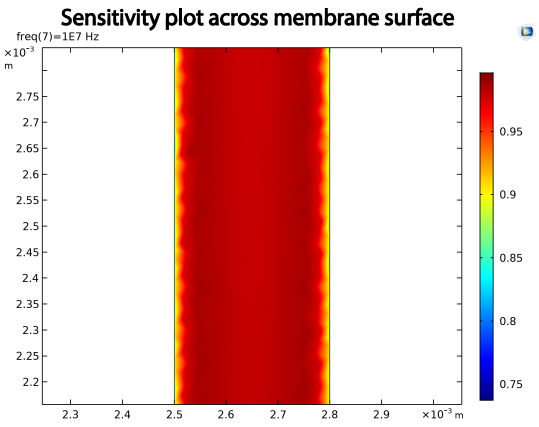

(b) Zoomed in view.

Figure 3.11: Sensitivity across the full membrane area for electrodes on slanted sidewalls at 10 MHz.

3.2. Fluid flow

After conducting electrical simulations to derive an optimal electrode and channel geometry, fluid flow simulations were conducted to verify whether shear stress values at the cell layer level in such a model fall in line with recommendations from literature (0.3 Pa to 2 Pa, as said in Section 2.1).
For this purpose, the model illustrated in Figure 3.1 was expanded with microfluidic inlets and outlets with a diameter of 1mm (shown in Figure 3.12).

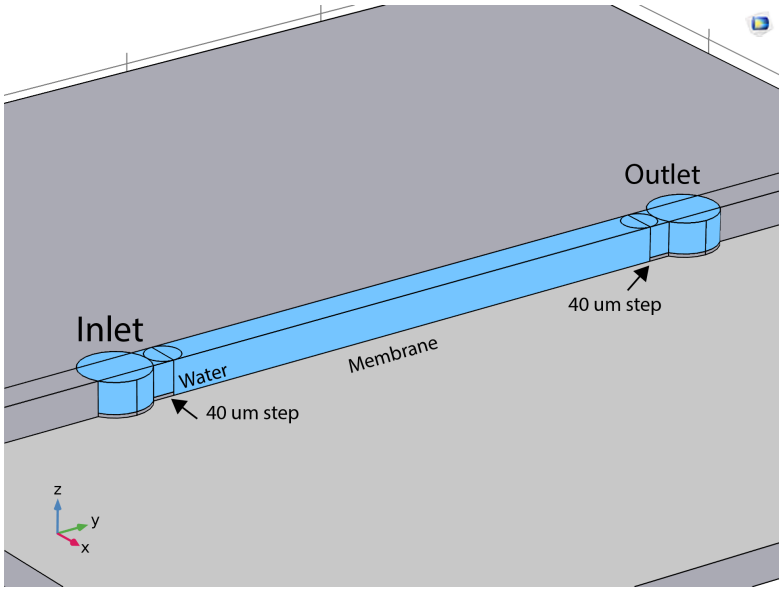

Figure 3.12: COMSOL model used for fluid simulations.

It is important to notice that the inlets and outlets are not directly above the membrane area. A 40 μm step (made of Si) was placed in between the inlet/outlet area and the membrane area to ensure that fluid which flows vertically through the inlets/outlets can change direction, therefore making only horizontal fluid flow present across the membrane/cell area. The step also ensures that membranes will not fracture as easily in case of mishandling while placing the fluidic connections.
Water (viscosity of $\mu = 1 mPa \cdot s$) was simulated inside one of the microfluidic channels and using the Laminar Flow module in COMSOL, average flow rate of the fluid at the inlet was set as:

$$Q = \frac{\tau_w}{6\mu} w h^2 \tag{3.3}$$

which is derived from Equation 2.3 (this equation assumes $w >> h$, but it was still used for simplicity as the actual values will anyways be calculated using COMSOL). A shear stress (τ_w) value of 0.5 Pa was used. A no-slip boundary condition was imposed on the walls of the microfluidic channel.
Fluid velocity profile at half of channel width can be seen in Figure 3.13a. As can be seen, velocity profile shows a higher fluid velocity around the center of the channel and reducing velocity towards the channel walls, as expected during laminar flow. Upon closer inspection (shown in Figure 3.13b), a small amount of dead volume (deep blue color) can be noticed at the step between the inlet/outlet area and membrane area. This issue can be fixed by smoothing out the transition between inlet/outlet area and the membrane area, which is possible to do during fabrication.
The shear stress levels across the membrane can be seen in Figure 3.14 (calculated by multiplying the shear rate with water's viscosity). The shear stress values do fall in range with the values recommended in literature for endothelial cells, thereby verifying that the channel geometry required for uniform sensitivity during TEER/EIS measurements is also suitable for dynamic cell cultures. It can be noted however that the shear stress values are not equal across the channel width meaning that once cells are seeded on the membrane, a shear stress gradient across them could be expected. Nevertheless, a uniform shear stress is impossible to achieve without using a channel with a circular cross-section. A very low aspect ratio ($\frac{h}{w}$) rectangular channel might help to ensure a more uniform shear stress distribution, but as was seen in Figure 3.6a, decreasing the channel's aspect ratio results in a lower sensitivity, so this option was not selected.

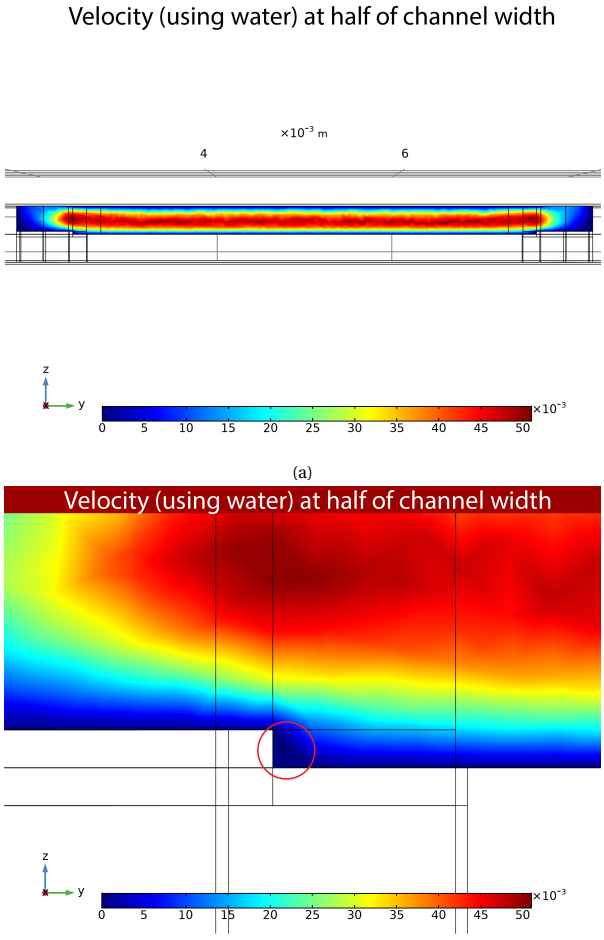

Figure 3.13

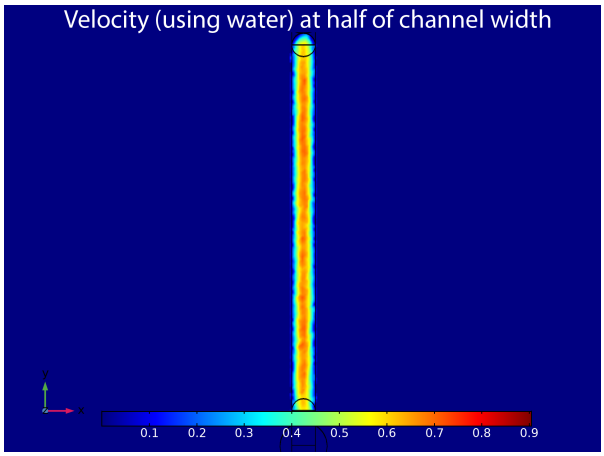

Figure 3.14: Shear stress values across the membrane area.

3.3. Membrane stability

The final aspect which needs to be verified through simulations is the membrane's mechanical strength. When designing a porous membrane, many aspects need to be considered to ensure mechanical strength and fabrication feasibility. The mathematical modelling and calculation involved in accurately determining how parameters such as pore size and interpore distance (which can be related to porosity in case the distribution

of pores is spatially periodic, for example in square or hexagonal packing) or membrane shape determine the membrane's maximum strength fall in the discipline of fracture mechanics and go beyond the scope of this thesis. Nonetheless, for fundamental understanding of how pores influence mechanical strength Griffith's law of crack propagation in brittle materials can be used [65]:

$$K_{Ic} = \sigma_{total} Y \sqrt{\pi a} \tag{3.4}$$

where K_{Ic} represents material's fracture toughness, σ_{total} the total stress in the material (inclusive of intrinsic stress and stress caused by external factors), Y a dimensionless correction factor dependent on the geometry of the crack and a the half width of the crack (in this case the pore radius). The law essentially states that the fracture toughness of a material is proportional to the square root of the crack size. Furthermore, it explains that cracks in a brittle material under stress will propagate as long as the reduction of potential energy by cracking is greater than the increase in free surface energy caused by the increase in surface area (a practical real-world example of this is how cracks propagate in glass).
This model in itself is difficult to use as total stress and the correction factor are parameters which are ultimately governed by the chosen membrane design and fabrication method. A more practical law which can be used as a rule of thumb for estimating the strength of rectangular nanoporous Si_xN_y membranes is given as [66]:

$$\sigma_{ultimate,porous} = \sigma_{ultimate}(1-P)^{\epsilon} \tag{3.5}$$

where $\sigma_{ultimate}$ represents the ultimate tensile strength of Si_xN_y (highest reported values found are in the neighbourhood of 6 GPa [67]) and P the membrane's porosity. ϵ is a factor determined empirically and can be approximated as 2 [68] [66]. With the goal of fabricating a membrane with 20% porosity, this gives:

$$\sigma_{ultimate,porous Si_xN_y} = 3.84 GPa \tag{3.6}$$

which will be used as an approximate value to verify fabrication feasibility of sub-500nm pores.
The COMSOL model was therefore expanded using the Solid Mechanics module to include an array of 500 nm diameter pores arranged in a hexagonal lattice forming a 20% porous structure. In addition to the Si_xN_y layer, the membrane includes an SiO_2 layer forming a stack. This is necessary as the SiO_2 layer will be used as an etch stop layer during fabrication. Details on this procedure will be explained later, but for simulation purposes including this layer is important as it ultimately determines the fabrication feasibility. Similarly, due to the deposition methods used for fabricating these materials, intrinsic stress of the materials was included in the model and is equal to 250 MPa (tensile) for Si_xN_y and -300 MPa (compressive) for SiO_2 layer. The values for maximum first principal stress are given in Figure 3.15.

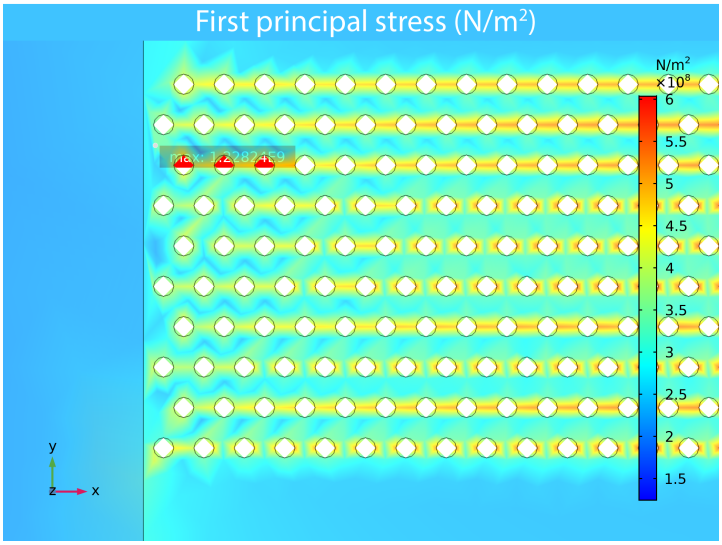

Figure 3.15: First principal stress in the membrane caused by pore distribution and fabrication method.

The maximum first principal stress does not exceed the ultimate tensile strength approximated as 3.84 GPa. Stress concentration is as expected occurring around the pores and the maximum value is reported at the

membrane edge in the porous area. Following the maximum normal stress theory [69], it is therefore expected that membranes should not fracture due to the deposition method or high porosity. Shown in Figure 3.16 it is expected that membrane buckling can occur due to the existence of an SiO_2 layer (which is compressively stressed).

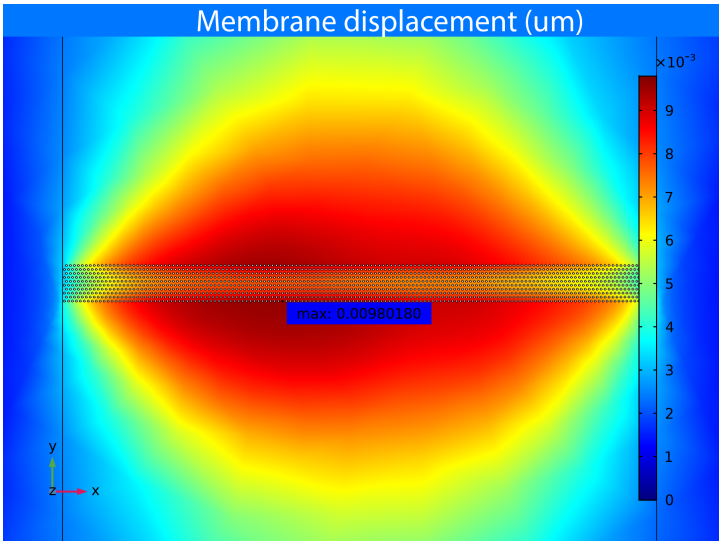

Figure 3.16: Displacement (buckling) of the membrane caused by pore distribution and fabrication method.

Unfortunately, as the pores are significantly smaller than other parts of the geometry, model meshing becomes very complex when the pore array exceeds dimensions of approximately 10 by 150 (150 pores cover the channel width) and results in the solution being uncomputable. Therefore, as can be seen in the figures, solution of a smaller array of pores (not fully covering the channel length wise) was taken as an approximate value.

Summary and conclusion

In this Chapter, an FEM-based optimization was conducted to derive an electrode geometry which enables uniform sensitivity for impedance measurements across the whole cell layer. The slanted sidewall electrode geometry was shown to be optimal for achieving this as well as having a promising fabrication feasibility. Following the electrical simulations, rudimentary fluid flow simulations were conducted to verify that levels of shear stress across a cell layer fall in range of literature recommendations. Ultimately, a membrane strength simulation was conducted, to verify that pore size, porosity and intrinsic stress that forms in the membrane layers (Si_xN_y/SiO_2) during fabrication cannot cumulatively cause the membrane to break.
Following successful optimization and verification through simulation, a fabrication process was conceived which will be explained thoroughly in the next Chapter.

4

Device Fabrication

Process overview

A broad fabrication process overview for the device designed in Chapter 3 is shown in Figure 4.1. As illustrated, the process consists of five major steps. A slanted sidewall is firstly fabricated on the top surface of an Si wafer, over which electrodes are deposited along with bonding pads. The microfluidic channel is then partially opened using two-step etching to produce a stepped structure between channel inlets/outlets and membrane area. A porous membrane is then patterned on one of the wafers and two wafers (one with and one without a silicon nitride membrane) are then bonded. Finally, the membrane is released by removing the remaining silicon from both sides of the bonded wafer. In the following Sections, each of the major steps will be thoroughly analyzed.

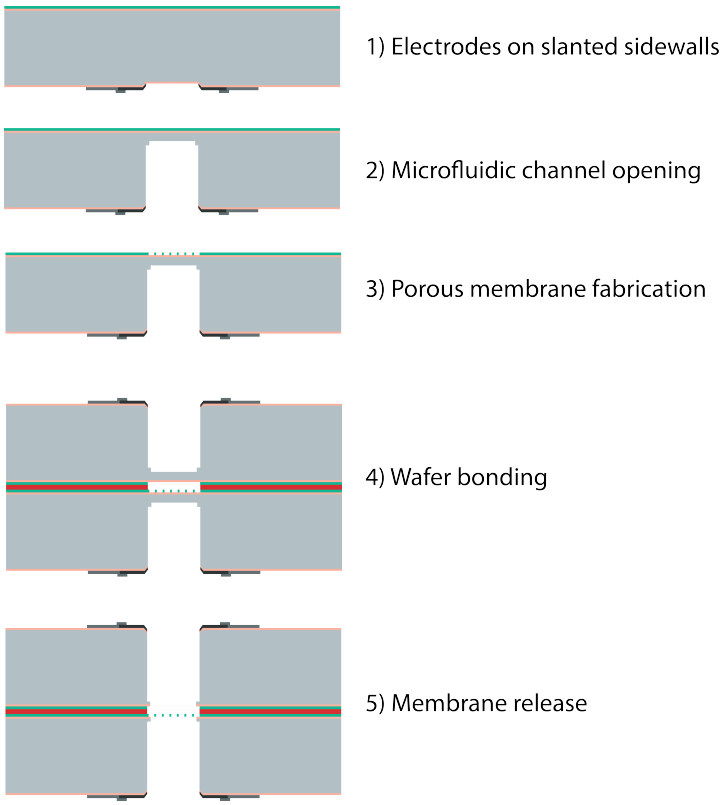

Figure 4.1: Overview of the process flow for the fabrication of the proposed OoC device.

4.1. Mask design

Based on the device topology optimized through FEM simulations (given in Chapter 3) and the fabrication flowchart, a set of photolithography masks was designed using Tanner L-edit. In total five masks are used and they contain five different device designs, which differ only by the channel length (spanning from 1mm to 5mm). The masks are designed to be used with a contact aligner. This means that each mask contains the photolithographic pattern which needs to be patterned across the full wafer (unlike a wafer stepper mask where the mask contains the design for an individual die). On each of the dies the design is placed in the center and is axially symmetric across the vertical axis (shown in Figure 4.2a). Similarly, the arrangement of dies with different designs across the full wafer is also symmetric across the vertical axis (shown in Figure 4.2b). By designing the masks this way, all of the wafers can be processed together until the wafer bonding step. During wafer bonding, one of the wafers is flipped over, but because of axial symmetry channels with the same length will be positioned on top of each other.

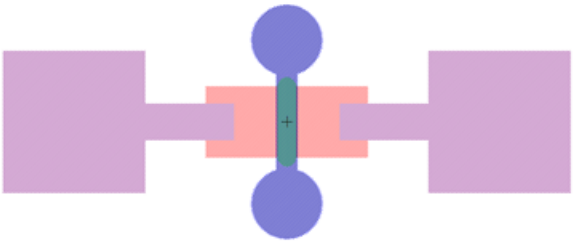

(a) Single die with a 1mm channel length.

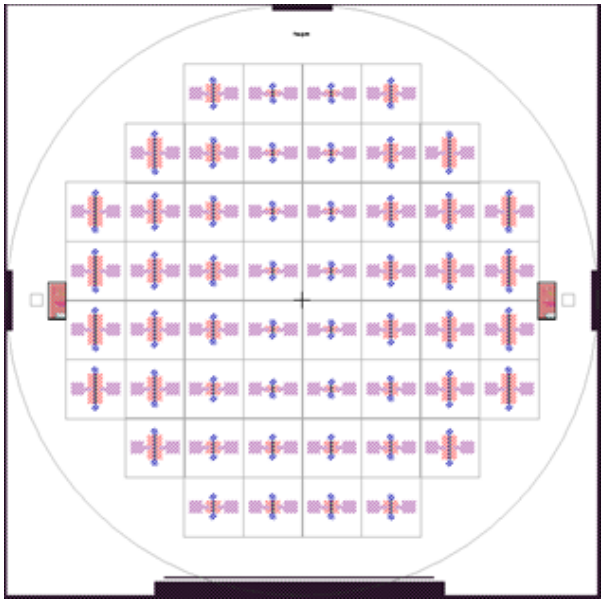

(b) Full wafer mask.

Figure 4.2: Mask set used for device fabrication (each color represents a different mask).

As the smallest feature sizes on the masks are in the order of hundreds of micrometers, PET film masks were purchased instead of quartz masks. Due to limited fabrication accuracy of such masks (typically around 10 μm), a margin between structures of overlapping masks was set to 10 μm, ensuring that masks used later in the processing cannot damage the previously fabricated structures (for example, in the mask used for microfluidic channel opening the edges of the opening are at a 10μm distance from the electrode edges).

Fabrication of lithography and bonding alignment markers

As a prerequisite for further processing, alignment markers need to be fabricated on 300μm thick <100> double-side polished (DSP) high-resistivity wafers.
The procedure for fabricating the lithography alignment markers is as follows:

- Spin coating of 1.4 μm of SPR3012 photoresist using EVG120 automatic spin coater (recipe: `1-Co-3012-1.4um-noEBR`)
- Exposure of `zefwam` job in the ASML PAS5500/80 wafer stepper using an exposure dose of 140 $\frac{mJ}{cm^2}$
- Single puddle development using MIF322 developer in EVG120 (recipe: `1-Dev-SP`)
- 120 nm Si etch using Trikon Omega ICP-RIE etcher with the program `URK_NPD` (60 mTorr, 80 sccm Cl, 40 sccm HBr, 500W ICP, 20W RF) for 40 seconds

Subsequently the photoresist is stripped off the wafers using a TePla Plasma 300 oxygen plasma asher and cleaned with EKL's standard Si cleaning procedure (10 min in 99% HNO_3, DI water rinse, 10 min in hot 69% HNO_3, DI water rinse, drying). In further text this cleaning procedure will be referred to as Si cleaning. The above process steps are repeated for the other side of the DSP wafers as well.
As the process involves wafer-to-wafer bonding, it is also necessary to fabricate alignment markers for the AML wafer bonder at the beginning of the process. These alignment markers are used for in-situ alignment within the bonder and are placed at a distance of 3.5 cm from the wafer center, in the same line as lithography markers. Two exposure jobs are used in the stepper for this purpose: `zeaml_up` and `zeaml_down`, one for the wafers which will be used as top wafers during bonding and one for the wafers which will be used as bottom wafers during bonding and the exposure is done on backside of the wafers. These alignment markers need to be etched deeper than the standard lithography markers (about $0.5\mu m$) as they need to be visible with the wafer bonder's infrared cameras (standard 120 nm depth is too shallow to make them visible, when viewing through a 300 μm wafer). The etching process `LEON1` for these markers is the same as the one for lithography markers (60 mTorr, 80 sccm Cl, 40 sccm HBr, 500W ICP, 20W RF), however they are etched for 6 minutes in order to fabricate deeper holes.

4.2. Electrodes on slanted sidewalls

The fabrication process for making electrodes on slanted sidewalls is schematically shown in Figure 4.3. Briefly, the process constitutes of fabricating an SiO_2/Si_xN_y layer stack which serves as a hard mask for slanted sidewall fabrication (and later as the porous membrane). Once the sidewall is fabricated, an SiO_2 insulation layer is deposited over which a TiN/Ti layer is deposited and patterned. Aluminum bonding pads are deposited and patterned subsequently.
In the following paragraphs, each of the steps will be explained in more detail along with all of the determined process parameters.

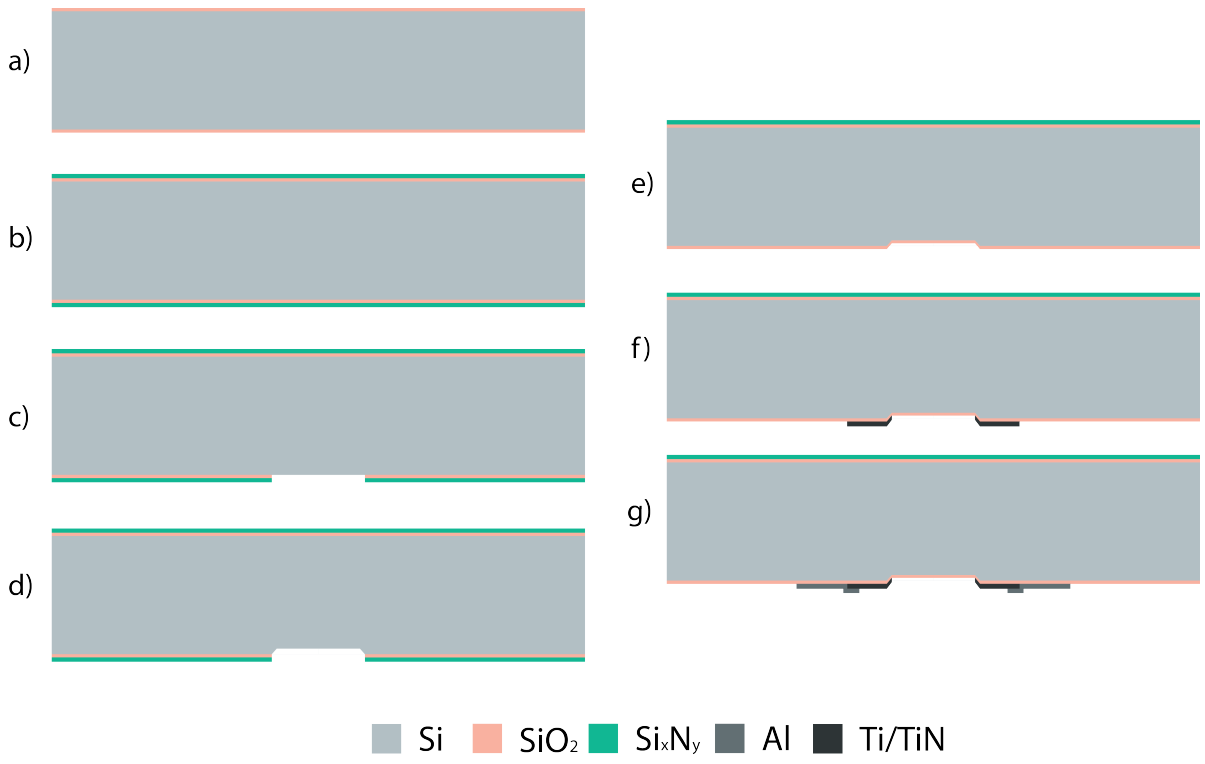

Figure 4.3: Fabrication flow for electrodes on slanted sidewalls. a) growth of SiO_2, b) LPCVD LS Si_xN_y deposition, c) Si_xN_y/SiO_2 hard mask opening, d) TMAOH anisotropic wet etching for slanted sidewall fabrication, e) removal of the hard mask and deposition of 200 nm thick PECVD SiO_2 isolation layer, f) deposition and patterning of TiN/Ti electrode, g) deposition and patterning of AlSi bonding pads.

Thermal oxidation and deposition of low-stress silicon nitride

The process starts by growing a 150 nm thick SiO_2 layer using wet oxidation of Si in a Tempress furnace at 1100°C for 5 minutes and 40 seconds (illustrated in Figure 4.3a). This silicon oxide layer will be utilized only at the very end of the process, when releasing the Si_xN_y membrane using deep reactive ion etching (DRIE).
Thermal oxidation is followed by a deposition of a 150 nm thick Si_xN_y layer using low pressure chemical vapour deposition (LPCVD). LPCVD deposition is highly favoured in comparison to plasma enhanced chemical vapour deposition (PECVD) for membrane applications as the layer quality in terms of mechanical properties is much higher (lower porosity, higher uniformity).
The process conditions for the thermal oxidation and LPCVD deposition are a critical decision, as the two layers have opposing intrinsic stresses (compressive stress in the oxide layer and tensile stress in the nitride layer). The resulting stress of the layer stack can be detrimental to the membranes released by DRIE in case it is not considered early in the process.
In the case of wet thermal oxidation, the stress can be tuned only by growth temperature as shown in Figure 4.4. As the stress figure is the lowest at 1100°C, oxidation is done at this temperature.

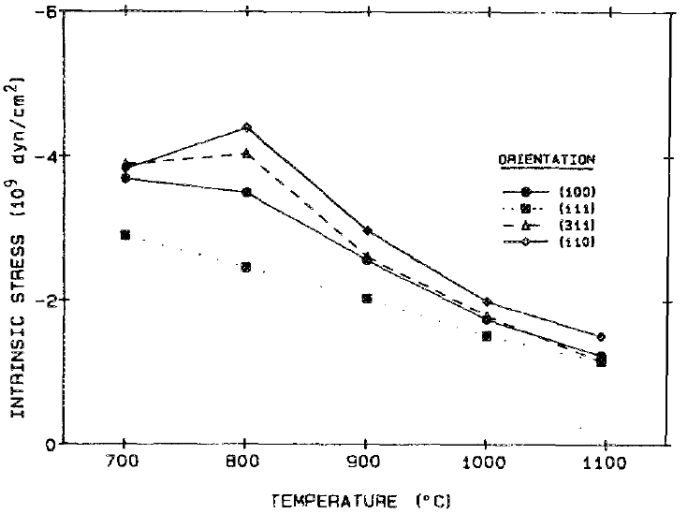

Figure 4.4: Stress in SiO_2 layer depending on temperature and wafer's crystal orientation. Adapted from [70].

An alternative to thermal oxidation would be to use LPCVD deposition of SiO_2 from tetraethoxysilane (TEOS), which has similar properties to silicon oxide and can be used as an etch stop layer. However, due to the deposition method it is possible to tune the intrinsic stress of the layer. In this way low compressive stress (-50 MPa) silicon oxide layers can be deposited, which would reduce possible membrane buckling [71]. Unfortunately, at the time of processing, TEOS LPCVD furnace was out of operation, so thermal oxidation was used.
In the case of LPCVD deposition of Si_xN_y, the layer stress can be tuned by changing the ratio of precursor gases (dichlorosilane and ammonia). Depending on the gas ratio, the silicon nitride layer changes from stochiometric (Si_3N_4) to non-stochiometric (higher concentration of Si atoms) and the intrisic stress can be tuned from low compressive stress (-50 MPa) to high tensile stress (GPa range). Although a high tensile stress would be wanted in order to mitigate membrane buckling issue, it is known that inclusion of pores in the membrane will result in high stress concentration points around the pores where the stress value may easily exceed tensile strength of the material resulting in crack propagation and membrane fracture [66] (see also analysis in Chapter 3).
For this reason it was decided to tune the stress in the layer to 250 MPa knowing that light buckling can be expected, yet minimizing the risk of membrane fracture due to high porosity. Using EKL's Si_xN_y LPCVD furnace stress-to-gas ratio diagram shown in Figure 4.5 (the 'New' in the legend denotes the use of a new furnace tube), the required gas ratio was determined to be 0.2698 (315 sccm SiH_2Cl_2, 85 sccm NH_3) with a deposition time of 16 minutes and 30 seconds (illustrated in Figure 4.3b).

Slanted sidewall fabrication

Slanted sidewalls in silicon are conventionally fabricated by anisotropic wet chemical etching using potassium hydroxide (KOH) or tetramethylammonium hydroxide (TMAOH). Owing to different etch rates between

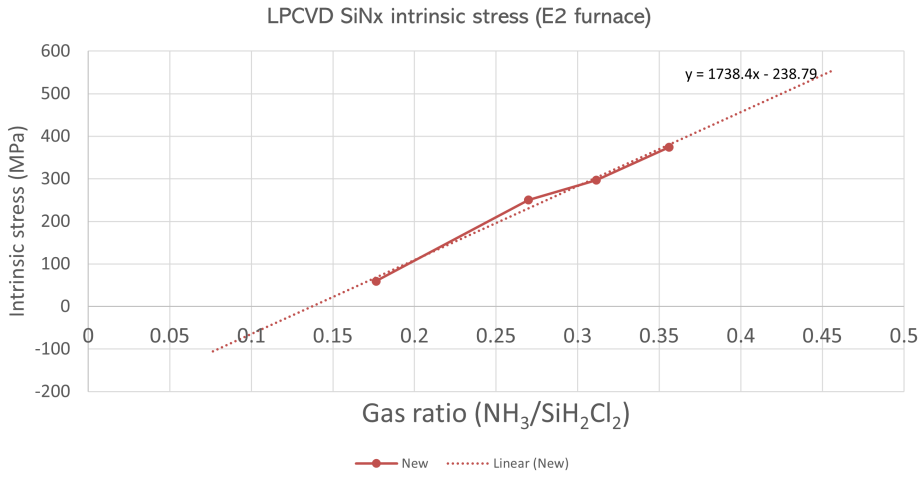

Figure 4.5: Stress in Si_xN_y layer deposited by EKL's LPCVD furnace.

crystallographic planes, where the <100> plane is etched in orders of magnitude faster than the <111> plane, sidewalls with an angle of 54.7°with respect to wafer surface (<100> plane) can be made (as shown in Figure 4.6).

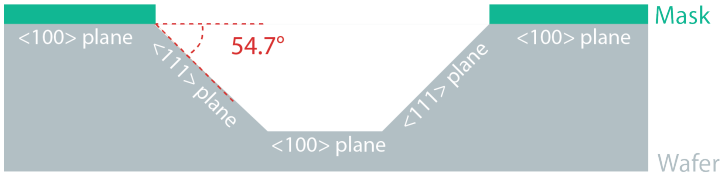

Figure 4.6: Characteristic sidewall obtained by bulk micromachining of Si using anisotropic wet chemical etching.

Depending on the etchant used (KOH or TMAOH): the etch rate, crystallographic plane selectivity and the type of masking material are changed. As a consequence of etch rate, sidewall surface roughness is also dependent on the etchant used (high etch rate results in rougher sidewalls).
Through previous work of ECTM's OoC subgroup it was determined that TMAOH is a better choice for fabricating sidewalls with low surface roughness, an important requirement for subsequent electrode fabrication. As both TMAOH and KOH are basic chemicals, photoresists cannot be used as a mask since they would get dissolved. Instead, a hard masking material such as SiO_2 or Si_xN_y needs to be used (and in the case of KOH, only Si_xN_y is applicable). Because the wafers at this point have a layer stack of SiO_2 and Si_xN_y on both sides, an opening needs to be created on the front side to expose the silicon surface (illustrated in Figure 4.3c). For this purpose the following photolithography process was used:

- Spin coating of 1.4 μm of SPR3012 photoresist using EVG120 automatic spin coater (recipe: `1-Co-3012-1.4um-noEBR`)
- Exposure through `KOH_Channel_Opening` mask in the SUSS Microtec MA8/SA8 contact aligner
- Single puddle development using MIF322 developer in EVG120 (recipe: `1-Dev-SP`)

The required exposure time was determined to be 16 seconds. Taking into account the exposure power of the contact aligner which was measured as 14.4 $\frac{mW}{cm^2}$, this results in an exposure dose of 230 $\frac{mJ}{cm^2}$. This value is considerably higher than EKL's recommended exposure dose for this photoresist thickness (150 $\frac{mJ}{cm^2}$). The increase in exposure dose is required as the underlying layer of Si_xN_y absorbs UV-light and normally the exposure dose for the used machine is calculated for the broadband exposure power (no light filters are installed in the machine). The openings in the PR mask were etched using Drytek Triode dielectric etcher. Firstly, the silicon nitride layer was etched in a C_2F_6 plasma (250W RF, 130 mTorr, 65 sccm C_2F_6) for 40 seconds. This removes the full silicon nitride layer. Subsequently, the oxide layer was removed in a C_2F_6/CHF_3 plasma (300W

RF, 180 mTorr, 36 sccm C_2F_6, 144 sccm CHF_3) for 30 seconds. Photoresist was then stripped off and the wafers were cleaned. As standard cleaning (and even exposure to atmospheric oxygen) develop an oxide layer on top of silicon surface, this layer needs to be removed prior to TMAOH etching in order to minimize issues with micromasking. For this purpose two options exist inside EKL: Marangoni passivation and HF 0.55% native oxide removal. Both options were tested and yielded similar results, however as HF 0.55% is faster and easier to use, it was chosen as the optimal method.
The etch rate of both KOH and TMAOH is dependent on temperature and it increases with rising temperature. At 85°C, the etch rate of TMAOH was determined to be about 0.56 $\frac{\mu m}{min}$ when using a bath with a freshly replaced chemical (the etch rate drops as the chemical is used more and as it ages). A total etch time of 18 minutes and 30 seconds was used in order to etch approximately 10 μm deep holes (illustrated in Figure 4.3d). After cleaning the wafers, the remaining SiO_2/Si_xN_y layer stack that served as a hard mask was removed using the Drytek Triode dielectric etcher with the same procedure as before.

Electrode and bonding pad fabrication

Once the trenches with slanted sidewalls have been etched using TMAOH, electrodes on them can be fabricated. Prior to metallization however, it is important to isolate the silicon surface, in order to minimize any possible electric conduction through silicon (illustrated in Figure 4.3e). For this purpose, a 200 nm thick SiO_2 layer was deposited using PECVD inside Novellus Concept 1 on the wafer's top side. The PECVD deposition is done using SiH_4/N_2O plasma at 400°C with the standard `.xxxsiostd` recipe.
The metallization for this process can in general be done in two ways:

- first deposition and patterning of TiN, then deposition and patterning of Al
- first deposition and patterning of Al, then deposition and patterning of TiN

Originally the second option was chosen, with the intent to pattern both metals using RIE. However, as plasma etching of TiN has little selectivity towards Al, it would be necessary to use an intermediate SiO_2 layer in between the two metals with only a small contact opening, which would prevent unintentional overetching and damaging of the Al layer.
In the case the first option is used, the Al layer can be patterned using wet etching instead of plasma in a mixture of phosphoric acid, acetic acid and nitric acid in a ratio of 77/19/04 (commonly known as PES etchant). PES exhibits infinite selectivity towards TiN, conveniently mitigating the need for an 'oxide-in-between' layer (TiN is generally a stable compound, unetchable in most commonly used wet chemicals). For this reason, this processing method was chosen as the optimal one.
Deposition of TiN was done using Trikon Sigma sputtering tool. Firstly, a 20 nm layer of Ti was deposited as an adhesion layer followed by a deposition of 300 nm of TiN at 6kW sputtering power and 350°C.
In order to pattern the TiN/Ti layer, photoresist was applied by using the following photolithography steps:

- Spin coating of 1.4 μm of SPR3012 photoresist using EVG120 automatic spin coater (recipe: `Co-Topo-3027-3.1um-noEBR`)
- Exposure through `Electrodes` mask in the SUSS Microtec MA8/SA8 contact aligner
- Double puddle development using MIF322 developer in EVG120 (recipe: `1-Dev-DP4`)

As can be noticed, regardless of topography present on the wafer surface (10μm deep trench) it was possible to apply photoresist using spin coating instead of spray coating, thereby considerably reducing the processing time. The way of achieving this was the use of a `Topo` type recipe in the EVG120 coater. In Figure 4.7 a comparison between the two coating recipes is shown.
During a `Topo` recipe the dispense arm moves across the wafer as it is spinning, dispensing a larger amount of photoresist uniformly across the wafer. In this way the effect of photoresist deposition only inside trenches is minimized. However, as the photoresist accumulates at slanted sidewalls (making the effective thickness at the sidewalls larger, shown in Figure 4.8), it is necessary to overexpose the photoresist. This will result in correct exposure energy for the sidewalls, however the topmost surface of the wafer will be overexposed as the photoresist there is thinner (nominal thickness). In the case of this process flow, electrode dimensions on the topmost surface are in order of hundreds of micrometers to millimeters, so overexposure does not reduce their size considerably to influence later device performance. The required exposure time was determined to be 40 seconds.

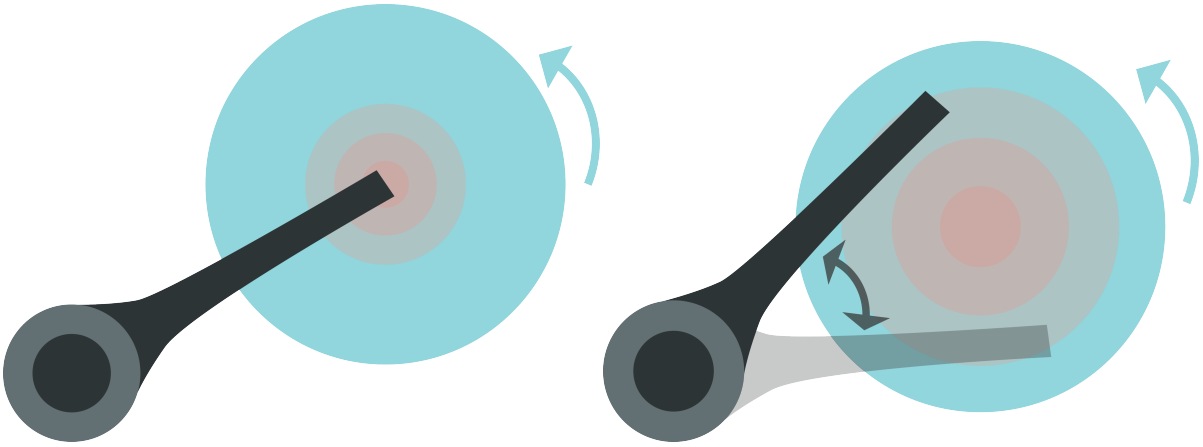

(a) Standard spin coating.

(b) Topo spin coating.

Figure 4.7: Comparison between standard spin coating and spin coating optimized for topography.

As for development, a double puddle process was used as single puddle development repeatedly resulted in residues of photoresist at the sidewall edges (shown in Figure 4.9). During a double puddle process, after the first development cycle, the developer is rinsed off using DI water and applied again. In case of thin photoresist layers this is not needed, however with accumulated thick photoresist layer at the sidewall double puddle development was shown as necessary.

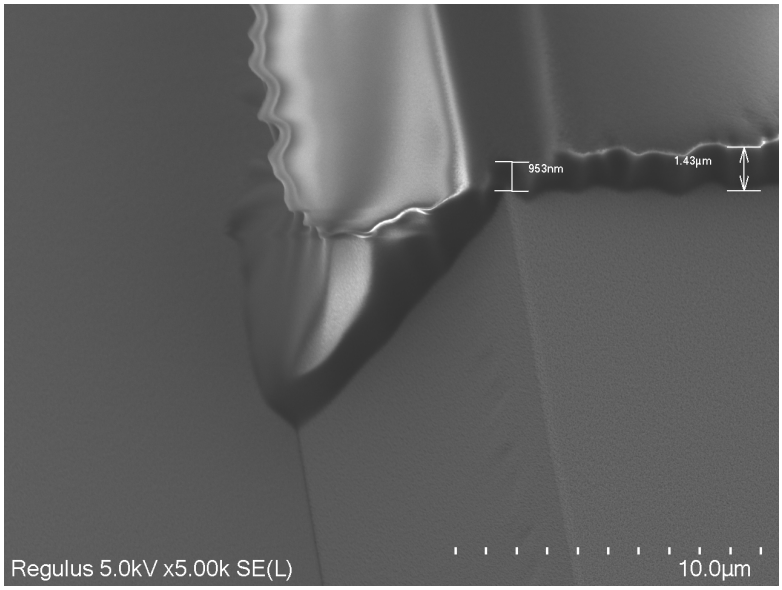

Figure 4.8: Photoresist accumulation at TMAOH-etched sidewalls.

TiN/Ti layer was etched using the Trikon Omega ICP-RIE etcher in a Cl/HBr plasma for 2 minutes and 25 seconds (5 mTorr, 30 sccm Cl, 40 sccm HBr, 500W ICP, 18W RF), in order to fully remove the layer (illustrated in Figure 4.3f). The sidewall electrode (after removing photoresist) is shown in Figure 4.10a.
After removing the photoresist and cleaning (HNO_3 99%, DI water rinse, drying, also known as 'green metal cleaning'), 675 nm of AlSi was sputtered on the wafer to fabricate contact pads. In order to pattern aluminum, same lithography process as for TiN/Ti electrodes was used, with the only exception being the use of `Interconnect` mask. Etching of the AlSi layer was as described previously done using PES for 4 minutes and 30 seconds (illustrated in Figure 4.3g). Since the layer also contains 1% of Si, a standard poly-Si etch bath (a mixture of HNO_3, HF and DI water) was used for 30 seconds to remove any potential Si residues. In Figure 4.10, the metallization of the whole device is shown.

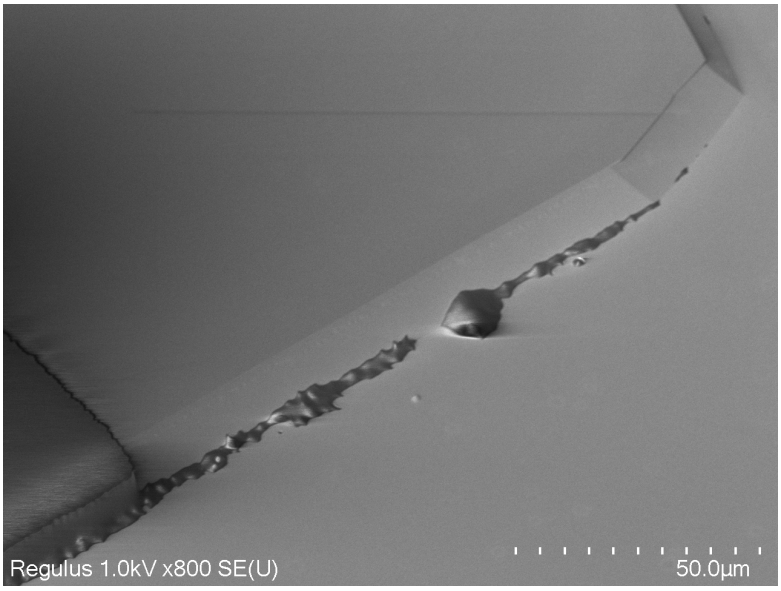

Figure 4.9: Residues of photoresist after a single puddle development.

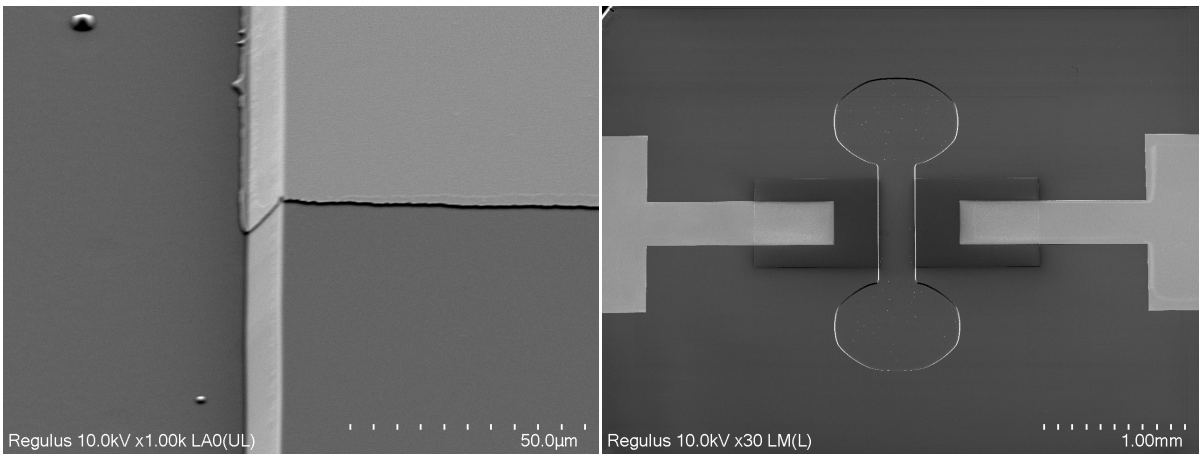

(a) TiN/Ti electrode coverage of the sidewall.

(b) Full wafer metallization.

Figure 4.10: Metallization after etching.

To verify that an electrical connection between the contact pad and sidewall electrode exists, a needle probe station was used. Resistance of 89 ± 4 Ω was measured across different dies and wafers proving that the electrode was indeed connected to the sidewall (no cracking at the edge, as shown in Figure 4.10a).

4.3. Microfluidic channel opening using DRIE

Prior to porous membrane patterning, the microfluidic channels are *partially* opened. The reason for such ordering of steps (which may seem unreasonable at first) is that the membrane patterning process which is explained in the following section, results in wafer contamination. Inside EKL, cross-contamination is prevented by restricting the use of many machines to only clean samples. One of the machines for which this is applicable is the SPTS Rapier. This machine is used for deep reactive ion etching (DRIE).
DRIE is a variant of RIE using which deep openings with high aspect ratio can be created in silicon. In the case of SPTS Rapier, a technique called Bosch process is used to achieve this. Conventional RIE relies on maintaining plasma of a constant gas composition (i.e. the ratio of all the gases used remains effectively the same), thereby providing a constant supply of reactive ions which can etch the material of choice at a stable etch rate. When deep or high aspect ratio features need to be etched in Si, as the plasma reaches deeper into Si and reacts with the Si surface, a part of the volatile compounds formed during the chemical etching process

redeposit on the Si surface. Because of this, the etch rate starts decreasing and the features are not etched as expected.

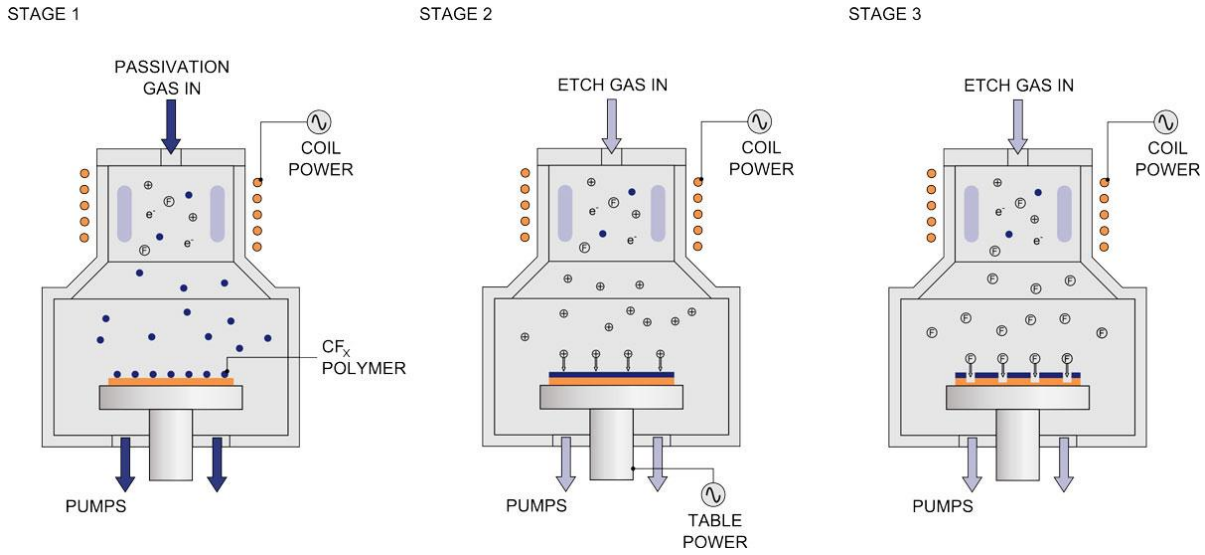

Figure 4.11: Bosch process illustration. Adapted from [72].

Bosch process (shown in Figure 4.11) uses a gas switching technique where firstly Si is etched using a high-density and highly accelerated plasma of SF_6, a normally isotropic dry etchant of Si. The high acceleration causes the etching to become more anisotropic. Instead of continuing the use of the same etching gas through the whole etching process, after a short time (typically a few seconds) the SF_6 gas supply is switched off and a passivation layer is applied on top of the substrate by using another gas which can form a polymer layer (typically C_4F_8). The passivation layer acts as an etch stop layer and if the substrate is exposed to unaccelerated SF_6 plasma again virtually no etching of Si would occur. However, once the gas supply again switches to SF_6 and a highly accelerated SF_6 plasma is created, it is able to (physically, not chemically) remove the passivation layer in a vertical direction. The passivation still however remains on the sidewalls of the etched structure, protecting it from isotropic etching. Therefore, by consistently switching the plasma composition, it is possible to etch deep structures in silicon with a vertical sidewall. However, as a consequence of gas switching, increased surface roughness on the sidewalls can be observed due to a 'scalloping' effect which is caused by a slight lateral etch during the SF_6 plasma etch step. As the Bosch process is dependent on many parameters (such as gas flow rates, chamber pressure, source and platen power, gas switching frequency and more), the technique is highly flexible in attainable etch profiles.
The process flow for opening microfluidic channels using DRIE is shown in Figure 4.12. As can be seen, the etching is done in two parts in order to produce a step profile between channel inlet/outlet and membrane area, as explained in Section 3.2.

Figure 4.12: Partial channel opening using DRIE. a) first DRIE etching step in the shape of the membrane, b) second DRIE etching step opening the microfluidic channel until 30 μm of Si is left.

As a masking material for DRIE, most commonly a thick photoresist layer or SiO_2 layer is used since the process involves highly accelerated ions which can even without chemical interaction remove thin masking materials.

Unfortunately, due to the use of TiN/Ti electrodes where Ti acts as an adhesion layer, SiO_2 cannot be used as a masking material. This is due to the way how SiO_2 mask would later be removed. The only viable option is the use of buffered hydrofluoric acid (BHF), which is also a strong etchant of Ti (HF acid etches TiO_2, but in an aqueous environment as soon as the TiO_2 layer gets removed, Ti is oxidized again and the process repeats). Because the Ti layer is only 20 nm thin, it is quickly removed causing the electrodes to peel off. For this reason, PR was chosen as the masking material.
As was seen in Section 4.2, it was found that spin coating using a `Topo` recipe is a feasible method for coating substrates that contain a trench with slanted sidewalls. Therefore, the photolithography process required for the first step is given as follows:

- Spin coating of 3.5 μm of nLoF 2020 photoresist using EVG120 automatic spin coater (recipe: `Co-Topo-nLoF-3.5um-noEBR`)
- Exposure through `Membrane_opening` mask in the SUSS Microtec MA8/SA8 contact aligner for 35 seconds
- Crosslink bake at 110°C for 90 seconds using the EVG120 (recipe: `X-link-bake`)
- Double puddle development using MIF322 developer in EVG120 (recipe: `1-Dev-DP4`)

The `Membrane_opening` mask was designed for use with a negative photoresist and accordingly AZ nLoF 2020 is used as an accepted standard negative photoresist in EKL. The photolithography process for negative PR is the same as the one for positive, except that it involves an additional crosslink bake step. Negative photoresists require this step to complete the chemical reaction in exposed areas which makes them insoluble in developer (in the case of some negative photoresists such as SU8, the crosslinked chemical bonds are sufficiently strong to make the photoresist even insoluble in common PR strippers such as acetone).
After developing the first mask for DRIE, a ~40 μm trench was etched in Si using SPTS Rapier. During etching it is important that the bottom-most surface (the one being etched) remains flat as the final goal is to land on a flat membrane with no residues of Si on the channel sidewalls. A recipe called `0EKL_FlatBottom` is optimized for this purpose (etch profile shown in Figure 4.13). The required numbed of Bosch process cycles with this recipe was determined to be 15, in order to achieve a ~40 μm deep trench.

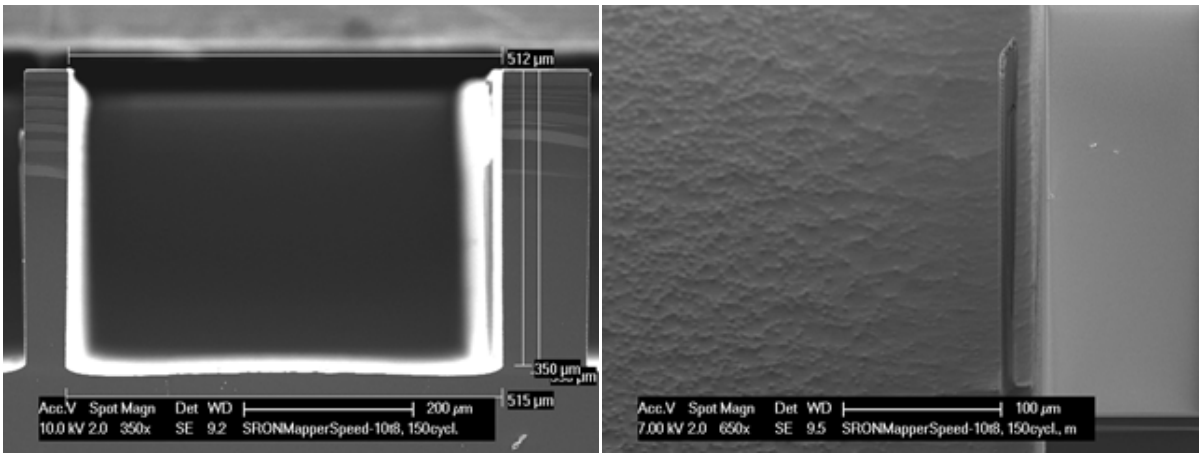

(a) 0EKL_FlatBottom side profile.

(b) 0EKL_FlatBottom bottom roughness.

Figure 4.13: 0EKL_FlatBottom recipe. Adapted from [73].

After the first DRIE step (illustrated in Figure 4.12a), the etched depth was verified and subsequently the photoresist was stripped off and wafers were cleaned.
For the second DRIE step (illustrated in Figure 4.12b), again a thick PR is used as a masking material. However, due to deep topography being present on the wafer, PR spin coating no longer presents a viable option so spray coating was used instead. During spray coating, PR is dispensed at a high pressure through a nozzle which creates a mist of photoresist droplets that uniformly cover the wafer surface regardless of present topography. As PR is normally a highly viscous substance it cannot be used 'out-of-the-box' for spray coating. Instead it needs to be diluted using propylene glycol methyl ether acetate (PGMEA) and methyl ethyl

ketone (MEK). The PR used for spray coating is AZ9260 and its dilution is already prepared by EKL for use with EVG101 spray coater. The following photolithography process was used to fabricate the DRIE masking for channel opening:

- Manual hexamethyldisilazane (HMDS) pretreatment using EVG120 or manual HMDS chamber for 10 minutes
- Spray coating of diluted AZ9260 photoresist using EVG101 spray coater in 8 layers (recipe: `HP-1000mbar-2mL-8layers`)
- Soft bake for 1 minute
- Repeat the previous two steps two more times, increasing the final bake time to 3 minutes
- Exposure through `Channel_opening` mask in the SUSS Microtec MA8/SA8 contact aligner for 40 seconds
- Manual development using AZ400K developer diluted in a 1:2 ratio with water, until all of the features are exposed

As can be seen, the spray coating process is repeated in a total of three times (24 photoresist layers). This is done because the photoresist does not form a perfectly uniform layer when it is spray coated and because it has a lower thickness when baked due to an increased amount of evaporated solvent which is added to reduce viscosity. When the photoresist mask is fabricated, DRIE etching can be repeated using SPTS Rapier. During the second etching step it is necessary to reach a total etch depth of 250 to 270 μm in the deepest trench, leaving approximately 30 to 50 μm of Si below the membrane patterning area which is necessary for the next fabrication step.
Similarly to before, the same `0EKL_FlatBottom` recipe was used, except for 75 cycles as a deeper etch is necessary. This resulted in a ~270 μm deep trench. However, an interesting issue occured during the second etch. Due to the combined effect of redeposition of Si and micromasking during DRIE etching, a barrier of Si pillars was created around the membrane area (shown in Figure 4.14a), which would in the final device create a blockage in the microfluidic channel (shown in Figure 4.14b).

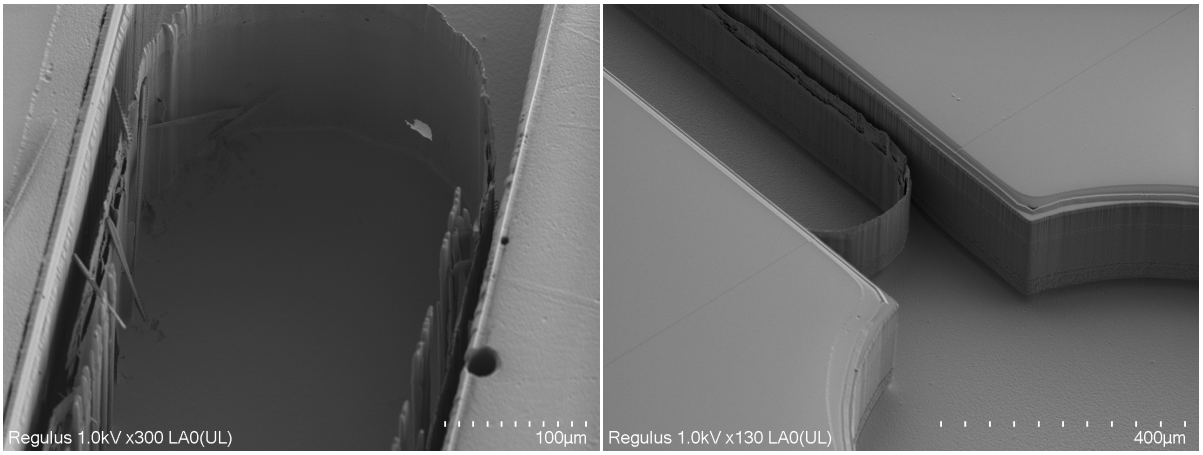

(a) Pillars of Si formed after the second DRIE step.

(b) Pillars of Si blocking the membrane area entrance.

Figure 4.14

An isotropic Si etch was used in SPTS Rapier to remove the pillars and smoothen the transition of the stepped structure, which is expected to solve the potential issue of dead volume at the step between the inlet/outlet area and membrane area discussed in Section 3.2 (shown in Figure 4.15). The recipe for this is `0EKL_IsoEtch` and it was used for 120 seconds.

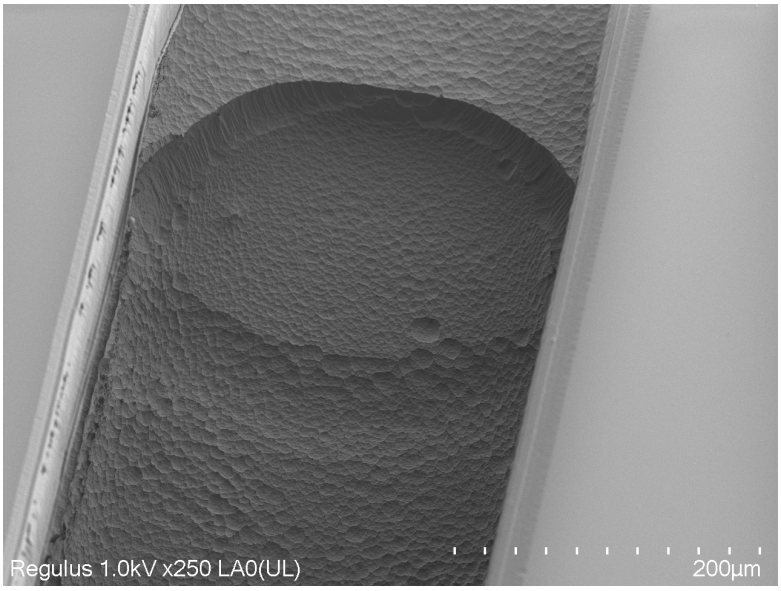

Figure 4.15: Membrane area entrance after pillar removal using isotropic Si etch.

4.4. Porous membrane

One of the goals of this thesis was to fabricate a highly porous, ultrathin membrane with sub-micrometer size pores. As was seen, it is hypothesized that a high porosity and low separation distance between endothelial cells and astrocytes may induce more accurate in vitro behaviour of the blood-brain barrier. For this reason, silicon nitride was chosen as the membrane material owing to its high mechanical strength even at nanometer-scale thickness. Fabricating a thin Si_xN_y membrane is a relatively simple process by using LPCVD and controlling it's intrinsic stress. Patterning membrane openings with a small feature size is a much more difficult task.
Conventional photolithography using a contact aligner available in EKL puts a resolution limit to about 2 μm. A feasible alternative to this (in EKL) would be the use of a wafer stepper, however even then the theoretical minimum pore size is limited to 500 nm. As the membrane sizes on the wafer span from 1 mm to 5 mm in length this would require five separate wafer stepper masks (two physical quartz masks as some designs can be combined on a single mask), thereby increasing the material costs considerably, with the benefit of ensuring a well known, repeatable procedure. Other options such as electron beam lithography or nanoimprint lithography were also considered, but due to unavailability of tools they were not used.
Instead of adopting a traditional top-down approach in pore fabrication, several different bottom-up approaches were considered which predominantly rely on self-organization of different materials in periodic structures with which ultimately pore arrays can be fabricated. In the next subsection, these will be briefly reviewed and at the end a comparison between the options will be given to justify the choice made in this work.

4.4.1. Bottom-up methods for pore fabrication

Block copolymer self-assembly

Block copolymers (BCP) are macromolecules comprised of two or more monomers (known as copolymers) in which distinct homopolymer subunits (known as blocks) are covalently chained together [74]. The subunits are always arranged in a periodic manner. For example, if a polymer A can be bonded to the start and end of polymer B the following arrangement can be made AAAAABBBBBAAA. In this example a triblock copolymer is given with three distinct blocks: AAAAA, BBBBB and AAA.
Block copolymers have the ability to self-assemble into various periodic structures through microphase separation, where distinct homopolymer regions are created (similarly to phase separation of oil in water, at a much smaller scale). The pattern in which they self-assemble is dependant on the type of BCP, deposition surface, ambient conditions, etc. The pattern can also be destroyed reversibly by increasing in temperature (shown in Figure 4.16a).

In microfabrication, the microphase separation of block copolymers presents a viable alternative to photolithography for producing large area periodic micro/nanostructures. Specifically in the case of porous membrane fabrication, polystyrene-b-poly(2-vinylpyridine) (PS-b-P2VP) diblock copolymers have been used [75] (process flow shown in Figure 4.16b). The block copolymer was self-assembled on top of an a-Si/Si_xN_y layer stack. A porous template was created by etching PS in O_2 plasma. Once The porous template (mean nanopore diameter of 95 nm) was transferred into a-Si, fabricating a-Si nanopillars. Cr was evaporated over the a-Si nanopillars and the pillars were effectively lifted off, leaving a porous membrane template. After this, using RIE the pores in the Cr hard mask were transferred into Si_xN_y.

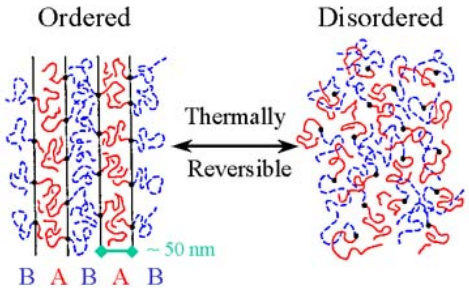

(a) Thermally reversible arrangement of BCP. Adapted from [74].

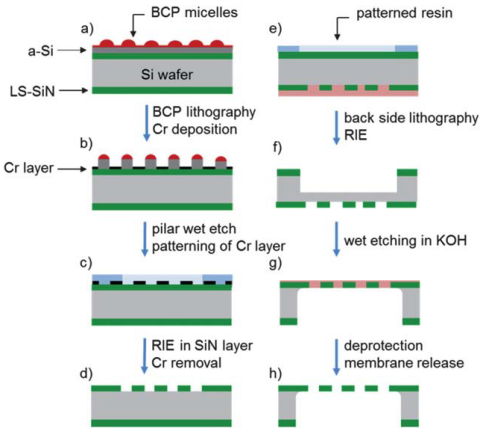

(b) Membrane fabrication using BCP lithography. Adapted from [75].

Figure 4.16: Block copolymer lithography.

Anodization of aluminium

Anodization of aluminium is a process used to grow aluminium oxide (alumina). Aluminium (solid piece, thin film, etc.) is used in an anodization bath filled with sulphuric acid and is connected as an anode in an electrochemical cell. Another electrode (typically from a different inert material such as Pt) is placed as a cathode. Once a current is applied between the electrodes, an oxidation reaction happens at the surface of aluminium, which consumes aluminium and transforms it into alumina.
The alumina layer grown in this manner forms a porous, honeycomb lattice structure. By controlling the conditions in which anodization is done (anodization voltage, acid concentration, etc.) it is possible to control the pore size and distribution.
When used in microfabrication, it is possible to produce porous alumina membranes using this technique. Similarly, it is possible to use the porous alumina template as a mask for making porous membrane of other materials such as SiO_2 or Si_xN_y (shown in Figure 4.17b).

Crystallization of a-Si

A method for fabricating nanoporous SiO_2/Si_xN_y membranes was developed by DesOrmeaux et al. [76] that uses rapid thermal annealing (RTA) in order to transform a-Si into poly-Si (shown in Figure 4.18). The method relies on depositing a Si_xN_y/a-Si/SiO_2 stack, where the a-Si upon short exposure to high temperatures (between 950°C and 1050 °C for 60s) crystallizes and (as it is constrained by the Si_xN_y and SiO_2 layers) forms poly-nano-crystalline silicon (pnc-Si). The pnc-Si layer is porous with a constant pore size of about 50 nm. The porosity can be tuned from 1% to 22%, by altering the annealing temperature. As the masking material for Si_xN_y is pnc-Si, a poor hard masking material for this purpose, during RIE it is also being removed so the Si_xN_y membrane thickness is ultimately limited by the pnc-Si thickness. Therefore, although the method is an elegant solution for creating highly porous membranes, pore size and membrane thickness are virtually fixed and determined only by the thickness of the pnc-Si layer (which also has an upper limit of about 50nm).

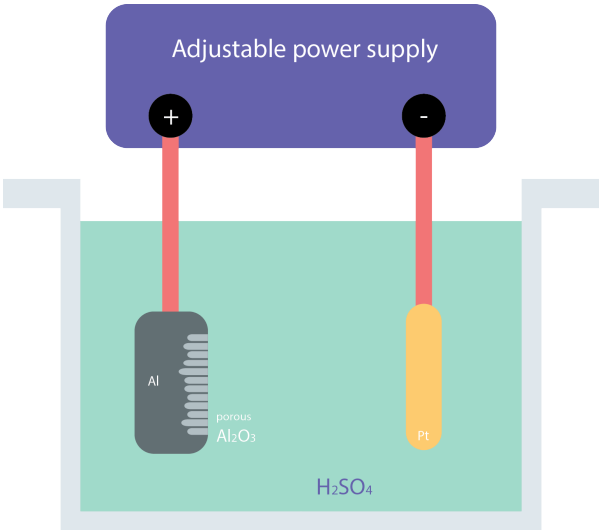

(a) Anodization of aluminum in a sulphuric acid bath.

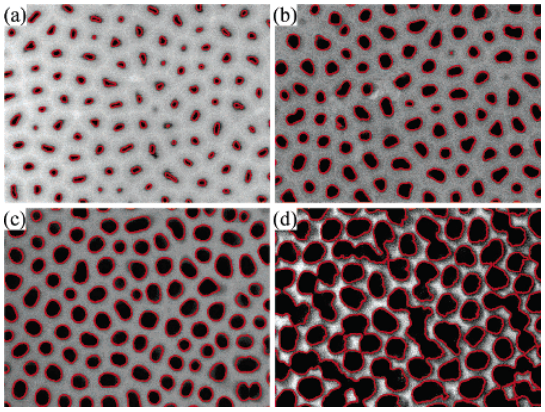

(b) Si_xN_y membrane made from a porous alumina template. Adapted from [77].

Figure 4.17: Membrane fabrication by alumina anodization.

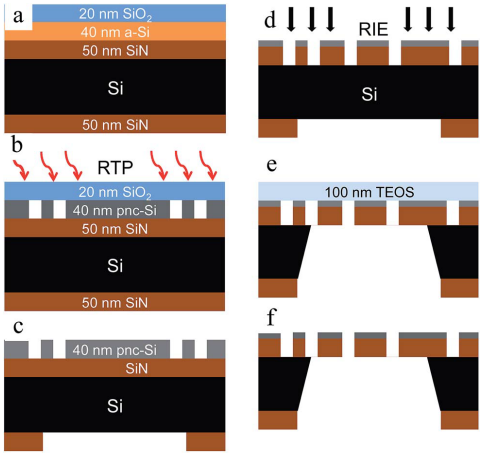

(a) Process flow for membrane fabrication using a-Si. Adapted from [76].

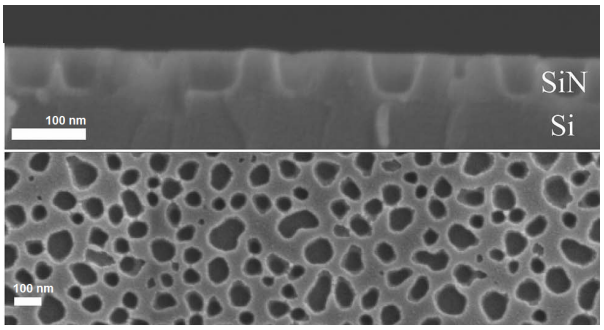

(b) Si_xN_y membrane made from a pnc-Si template. Adapted from [76].

Figure 4.18: Porous membrane fabrication using RTA of a-Si.

Nanosphere lithography

Nanosphere lithography (NSL) is a bottom-up patterning method which relies on self-assembly of colloidal suspensions of (micro/nano)particles into ordered arrays (the method is sometimes also called colloidal lithography or natural lithography). By combining the particle self-assembly with conventional microfabrication technologies such as RIE or PVD, the patterns made by the ordered arrays of particles can be modified and transformed into different geometric shapes. These can then be transferred to the underlying substrate to create ordered arrays of triangles, pyramids, pores, pillars, etc. Since the method is principally reliant on self-assembly of particles which can be produced in nanometer-scale dimensions, feature sizes of patterns fabricated using this method can have the same order of magnitude, significantly smaller than the feature sizes obtainable by photolithography. Particles used for NSL are most commonly made from polystyrene (PS) or silicon dioxide (SiO_2) and can be readily purchased as aqueous suspensions. The physical phenomena governing self-assembly are complex in nature and are dependent on many different variables such as the deposition method which is used for substrate coating (for example dip coating or spin coating) or the particle suspension used (for example, concentration of surfactants added to the water-based suspension). Consequently, although the method is highly flexible and cost-effective for fabricating periodically arranged

structures it is also highly vulnerable to any factors that might hinder the process of self-assembly.
In the case of porous membrane fabrication, because the feature sizes in NSL are governed mainly by the particle size, membranes with a flexible range of pore sizes and porosity can be made.

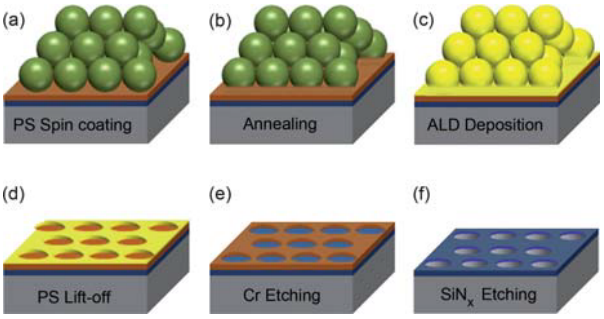

(a) Process flow for membrane fabrication using colloidal self-assembly and ALD. Adapted from [78].

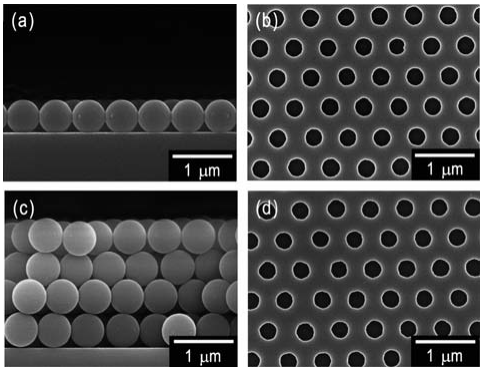

(b) Al_2O_3 deposition using ALD over a particle multilayer. Adapted from [78].

Figure 4.19: Fabrication of a porous membrane using colloidal self-assembly and ALD.

In Figure 4.19, an example of combining colloidal self-assembly with atomic layer deposition (ALD) is shown. On top of a Cr/Si_xN_y/Si layer stack, a layer of PS particles is deposited by spin coating. The particles are annealed just above glass transition temperature of PS (100°C), thereby increasing their contact surface area with the Cr layer (effectively reflowing the particles). Using ALD, an Al_2O_3 layer is deposited. Since ALD is a gas phase deposition method, no shadowing occurs in the case of a particle multilayer and Al_2O_3 layer forms on the substrate following the shape of the first layer of particles (as seen after particle lift off, shown in Figure 4.19b). The porous Al_2O_3 layer is transferred in the Cr layer using Cl_2-based RIE and subsequently the porous pattern from the Cr layer is transferred to Si_xN_y. The pores fabricated using this method have a circular shape and a high degree of orderliness, unlike the ones fabricated using anodization of aluminum or crystallization of a-Si.

Comparison between bottom-up methods

A comparison between the methods is given in Table 4.1.
As can be seen, due to the material and equipment availability, relatively low cost, flexibility in pore sizes and range of attainable porosity, nanosphere lithography is chosen as the best method for fabricating sub-500nm size pores.
Nanosphere lithography has not been previously used within EKL/ECTM meaning that until now, documentation of the technique does not exist tailored specifically to the machines available inside EKL/ECTM. Therefore, an in-depth process flow was developed and will be given in the subsequent Section.

Table 4.1: Comparison between reviewed bottom-up membrane fabrication methods.

Method	**Material cost (and availability)**	**Required equipment (and availability)**	**Pore size**	**Porosity**	**Note**
BCP lithography	Relatively inexpensive (if available), but often manually synthesized	Spin coater (available in EKL)	Typically between 10nm and 100nm	Flexible (tunable by modifying BCP chemistry or dry etching time)	Scalable to wafer-scale with spin coating
Anodization of aluminum	Inexpensive (commonly available chemicals)	Anodization bath (available in EKL)	Typically between 10nm and 100nm	Flexible	Scalable to wafer-scale, but use of aluminum hard masks is not allowed in RIE machines inside EKL
Crystallization of a-Si	None	RTA furnace (unavailable in EKL)	Up to 50 nm	Flexible (between 1% and 22%)	Scalable to wafer-scale, but an RTA machine is not available in EKL
Nanosphere lithography	Relatively inexpensive	Spin coater (available in EKL), doctor blade coater (available in ECTM)	Flexible (from tens of nanometers to micrometers)	Flexible (depending on deposition method and post-deposition processing techniques)	Difficult to execute on a wafer scale without using spin coating or a large blade for drag coating

4.4.2. Pore fabrication using nanosphere lithography

The porous membrane fabrication flowchart is shown schematically in Figure 4.20. In the rest of this subsection the process flow will be briefly explained with the goal of giving the reader a 'big picture' understanding on why each of the steps is done.

The process starts by depositing a layer of polystyrene particles on top of Si_xN_y surface. As the goal is to fabricate highly porous membranes, the particles must be assembled in a close-packed formation across large areas (in the order of cm^2), implying that the deposition needs to be done in a highly controlled manner. Two coating options exist within EKL/ECTM facilities which can be used for this purpose: spin coating and doctor blade coating.

Spin coating is undoubtedly the most commonly used substrate coating method in cleanroom processing. The reason for this is its intrinsic simplicity, where the layer thickness of any viscous substance that is being coated (such as photoresist) can be controlled by only changing the rotation speed (and potentially acceleration), as long as the environmental conditions are kept constant. A considerable downside of spin coating is large material waste as most of the material is spun off the edge of the substrate (in the case of photoresist spin coating, final deposited resist can be only 3% of the originally dispensed photoresist). Therefore this coating method was not attempted as it would ultimately require large volumes of particle solutions.

Doctor blade coating (or drag coating) is an alternative coating method, not commonly used in microfabrication, in which a small, droplet-sized amount of a liquid material (typical volume is in the order of tens of microliters) is dispended on a substrate and subsequently dragged over the substrate's surface. As the water (and other potential solvents) evaporate from the surface of the liquid which had been dragged, a dry film

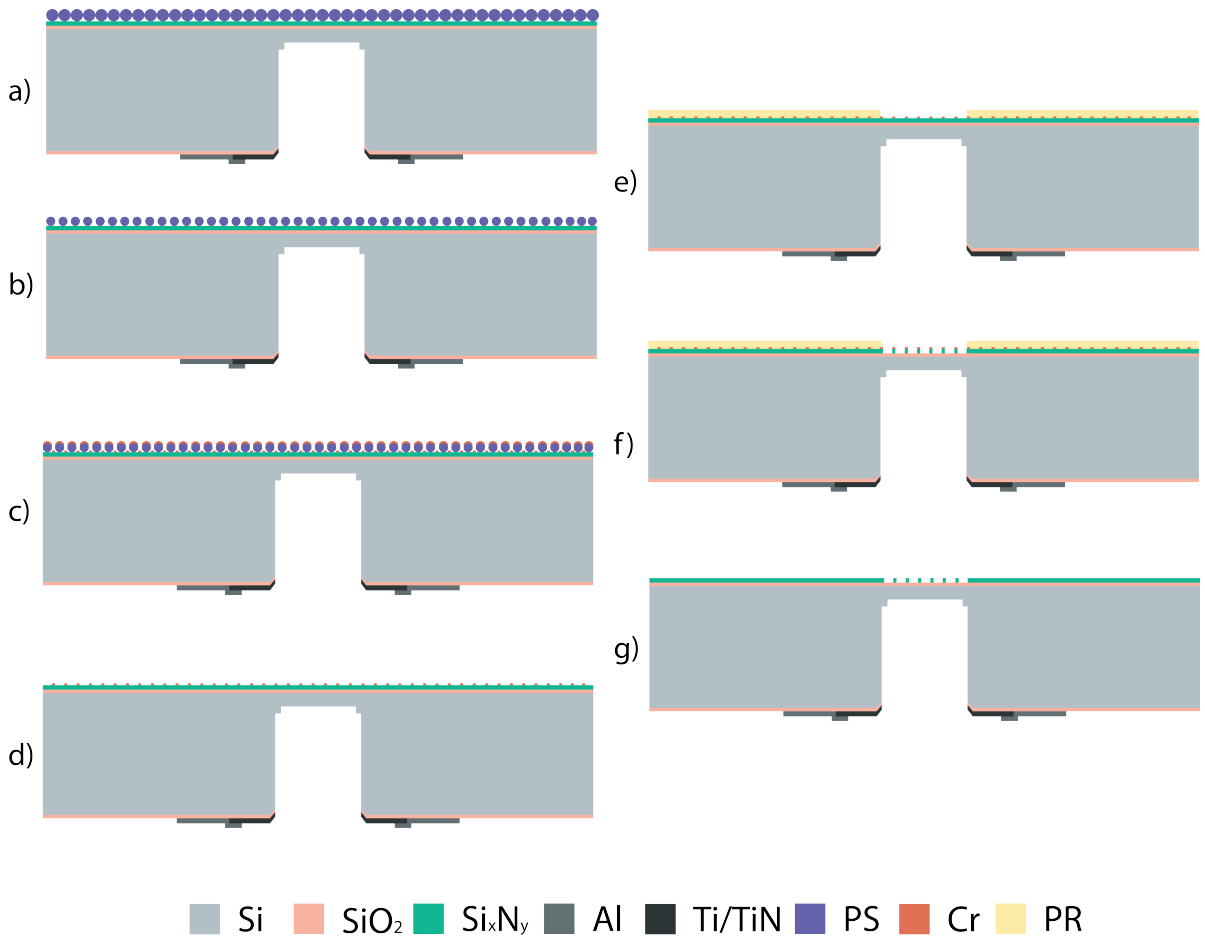

Figure 4.20: Membrane fabrication flowchart using nanosphere lithography. a) a layer of PS particles is deposited Si_xN_y using doctor blade coating, b) PS particles are reduced in size using O_2 plasma etching, c) Cr is evaporated over the wafer, d) PS is lifted off leaving a porous Cr mask, e) a PR mask is applied opening the membrane area, f) Si_xN_y layer is etched through the combined Cr/PR mask, g) PR and Cr layers are removed.

is left. Dragging speeds associated with doctor blade coating are quite low, making this method inherently slower to use than spin coating. Moreover, upscaling the method to wafer level is not as straightforward. However, this method enables an almost wasteless use of material. Additionally, colloidal self-assembly through doctor blade coating is considerably more covered in literature, thereby making it easier to use previous research as a base for process development. For these reasons, doctor blade coating was chosen as the method for coating.

After the particles are successfully deposited using doctor blade coating, they should ideally form hexagonally close-packed (HCP) monolayer crystals. However, their size needs to be reduced in order to form hexagonally non-close-packed monolayers (HNCP), as the membrane requires controlled pore-pore spacing to achieve sufficient porosity while retaining mechanical strength. For the purpose of particle size reduction, O_2 plasma is used as it can etch polystyrene.

Once a HNCP monolayer is formed with acceptable particle size and interparticle distance, chromium (Cr) is evaporated over the substrate. Chromium is a well-known hard masking material which can be used as a mask for Si_xN_y etching. Unfortunately, it is also a CMOS-incompatible material due to its diffusion through Si lattice. Because of this, inside EKL special precautions need to be undertaken. As polystyrene particles act as a shadow mask during evaporation, once they are lifted off, a porous Cr mask is left over the substrate. On top of the Cr hard mask, photoresist is deposited and patterned so that photoresist openings are created only in the designated membrane areas on the wafer. With the Cr/PR dual mask, using RIE the pattern is transferred into Si_xN_y layer.

Following the brief overview used to illustrate the overall process flow, a more detailed explanation of each of the steps will be given in the following sections.

Choice of particle size

Particle size is an important parameter which governs the final membrane's pore size and porosity. As was seen in Chapter 3, these parameters influence the membrane's mechanical strength. The goal was set to fabricate a membrane with a porosity in the range of 10%-20% with a sub-500 nm pore size. This includes a safety margin for what is achievable theoretically using Si_xN_y membranes, but it is used so that there is a higher likelihood of successful fabrication. With nanosphere lithography chosen as the method of fabrication and doctor blading as the particle deposition method, a hexagonal close-packing of the particle monolayer can be assumed (as shown in Figure 4.21a).

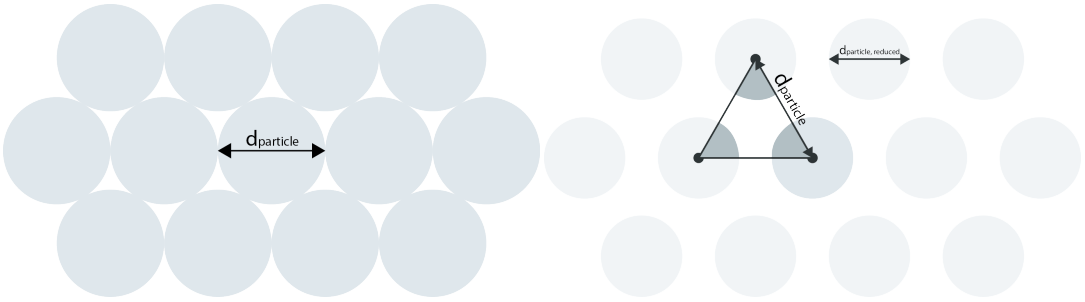

(a) HCP monolayer.

(b) Schematic used for calculating porosity of NHCP layer.

Figure 4.21: Hexagonal close packing (HCP) of polystyrene particles.

Each of the particles has a diameter of $d_{particle}$. In an HCP monolayer this also means that the distance between centers of neighbouring particles is equal to $d_{particle}$. As the particles are exposed to O_2 plasma, their diameter is reduced interparticle distance $d_{interparticle}$ increases. The porosity of the final membrane can then be calculated as:

$$P = \frac{A_{covered}}{A_{covered} + A_{uncovered}} \tag{4.1}$$

where $A_{covered}$ is the area covered by the Cr layer after PS lift-off (and similarly $A_{uncovered}$ is the uncovered area exposing the Si_xN_y layer). If lines are connected between centers of three neighbouring particles an equilateral triangle is formed (shown in Figure 4.21b) making it simple to calculate the porosity as:

$$P = \frac{A_{covered}}{A_{covered} + A_{uncovered}} = \frac{\frac{1}{2}\left(\frac{d_{particle,reduced}}{2}\right)^2 \pi}{d_{particle}^2 \frac{\sqrt{3}}{4}} \tag{4.2}$$

where $d_{particle,reduced}$ is the diameter of a particle after O_2 plasma etching. If we express this parameter as a fraction of the original diameter ($d_{particle,reduced} = F_{reduction} \cdot d_{particle}$) and rearrange the terms, we can obtain the necessary particle reduction factor $F_{reduction}$ as:

$$F_{reduction} = \sqrt{P \cdot \left(\frac{2\sqrt{3}}{\pi}\right)} \tag{4.3}$$

If we set the goal of a 20% porosity, this results in $F_{reduction} = 0.469$, which would require a particle diameter of $d_{particle} \approx 1\mu m$ to achieve sub-500nm sized pores.
With this calculation it was decided to purchase $1.1\mu m$ mean diameter polystyrene particles from Sigma-Aldrich in a 10% w/v concentrated suspension. The suspension already contains a sufficient (0.1% - 0.5%) surfactant concentration which prevents particle agglomeration and can be used as is or it can be further diluted/concentrated.

Particle deposition using doctor blade coating

Convective self-assembly by doctor blade coating is shown schematically in Figure 4.22. A droplet-sized amount of particle suspension is dragged across a substrate which needs to be covered. By examining the

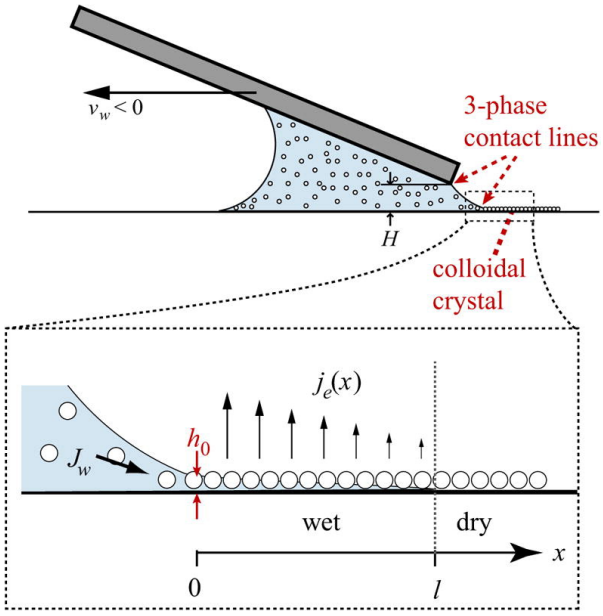

Figure 4.22: Doctor blade coating schematic. Adapted from [79].

coating macroscopically, as the suspension is dragged, at the three-phase contact line the solvent evaporates and particles are being deposited (not necessarily in a crystal form). The evaporation of the solvent (denoted by j_e) drives a convective fluid flow (denoted by J_W) with which new particles are being driven towards the contact line. In steady state, when the fluid evaporation rate matches the convective flow rate a steady amount of particles is deposited. The substrate which is being coated needs to be highly wettable by the suspension in order to form a thin deposition film thanks to the low contact angle at the receding three-phase contact line. In the drying region (further from the contact line, where no new particles are arriving through convective fluid flow), evaporation of the remaining liquid causes the particles to form dense structures due to capillary forces. Commonly, an equation derived by A. Dimitrov and K. Nagayama [80] is used to relate the dragging velocity with the film growth rate:

$$v_f = \frac{l_e \beta j_e \rho}{h_f (1-\epsilon)(1-\rho)} \tag{4.4}$$

where v_f denotes the film growth velocity, l_e the length of the wet film, β a coupling parameter which describes the particle-particle and particle-substrate interactions, j_e the evaporation flux, ρ the particle volume fraction, h_f the height of the wet film and ϵ the film porosity (0.605 in the case of hexagonal close packing). If all of the parameters required for solving this equation can be obtained and the substrate is withdrawn at the velocity v_f, a growth of a HCP crystal will occur. In practical cases however the velocities are obtained empirically as these parameters are difficult to measure. It should be noted that this relation was derived for dip coating, but it can be used for blade coating as the basic principle of convective self-assembly is the same.
The setup for doctor blade coating available in ECTM is shown in Figure 4.23. It consists of four main parts: a precise linear single-axis stage (actuated using a stepper motor) used to position the sample holder, a three-axis stage used to position the blade (glass slide), a light microscope used for real-time inspection and a substrate temperature controller (consisting of a Peltier heating/cooling element and a passive cooler). The linear single-axis stage for controlling the sample position and the light microscope are connected to a computer for easier control and visualization during coating.
The setup had thus far been used only for small samples and it was as such unsuitable for use over a wafer scale, especially considering the limited range of motion of the linear stepper-actuated sample positioning stage (maximum range of 52mm, with the wafer being 100mm in diameter). To mitigate this issue, an alternative holder was designed for the passive cooler which extends the linear axis' range of motion. The holder was placed on perpendicularly aligned aluminum rails which then allowed manual sample positioning in a second axis. With these two extensions it was possible to reach any point on wafer's surface. Additionally, a wafer holder was designed which mounts on top of the passive cooler and secures the wafer from accidental mishandling.

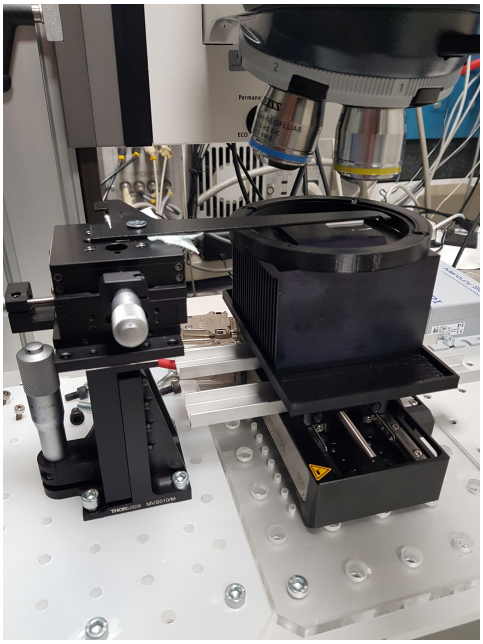

Figure 4.23: Blade coating setup.

As a preparation for blade coating wafers were cleaned for 15 minutes in 99% HNO_3, followed by a DI water rinse and drying. Just before the start of coating wafers were placed in an ATTO Diener O_2 plasma surface activation tool (75W, 0.25 mbar, 5 minutes). The surface activation tool is used to increase the surface energy of Si_xN_y and therefore make it highly hydrophilic.
Square shaped microscopy glass slides with a side length of 21 mm were used as a blade for the coating procedure. Once the substrate was placed in the holder, the blade was brought in contact with the substrate and the position was read out on the blade's height positioning screw. This was done prior to each coating as a rudimentary zero-level calibration. The blade was subsequently raised to different heights ranging from 0.6 mm to 1mm off the wafer's surface. A 65 to 75 μL droplet of the polystyrene particle suspension (10% w/v) was injected in the space between the glass slide and the wafer using an adjustable pipette.
With the droplet constricted between the wafer and blade, the linear stage was actuated (shown in Figure 4.24a) at a constant speed for which a particle monolayer is formed. These values typically ranged from 40 $\frac{\mu m}{s}$ to 60 $\frac{\mu m}{s}$ and were found to be strongly linked to room temperature and humidity (which is also suggested by literature [79]).
As was seen previously in the theoretical outlook on convective self-assembly, the solvent's evaporation rate plays arguably the most important role in quality of obtained particle films. Ambient conditions (pressure, temperature and humidity) determine the dew point of water which ultimately determines the evaporation rate. Using a battery-powered ambient temperature/humidity measurement tool during the coating it was noticed that the relative humidity (RH) in the room where the setup was placed (measurement laboratory of ECTM) fluctuates considerably in a range from 40% to 75%. The temperature was more or less constant at 22°C, and was not hence considered to be an issue in altering the evaporation rate.
By running tests across the span of multiple days (as the change in RH in the room was caused by different weather conditions), a fitting curve was derived (shown in Figure 4.24b) which gives insight to the approximately correct speed at which the linear stage needs to be actuated in order to assemble particles of $1.1\mu m$ diameter at a 10% w/v concentration. The distribution of obtained velocities was fitted to a linear curve and during each subsequent coating, an estimate for the correct speed was obtained with necessary changes in the range of $\pm 2um/s$ which needed to be adjusted manually.
After doing a single coating, coating quality was inspected. The coating quality can be easily assessed by visually inspecting the wafer under bright light, where the interference pattern caused by light scattering off the surface of monolayer particle film produces a characteristic quality, different from a multilayer particle film. If the coating was successfully done the blade was repositioned to the next position on the wafer and the coating was repeated (a successful coating implies a reasonably low number of voids and multilayers which inevitably happened). It was typically necessary to do between five to six times to coat the wafer sufficiently

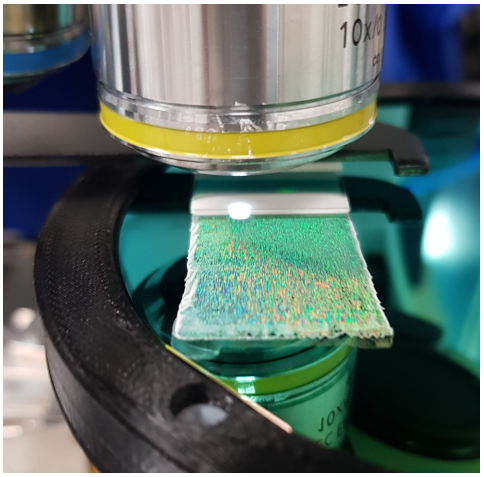

(a) Monolayer formation by the blade coating.

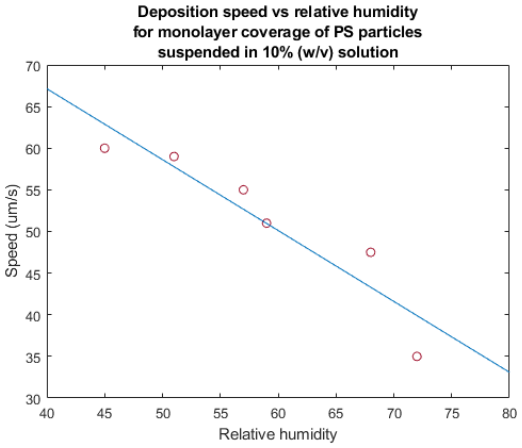

(b) Particle deposition speed as a function of ambient RH.

Figure 4.24: Blade coating.

(empty spots between the coatings will always exist using this method but as long as they are not in the areas covered with membranes the method is fine to use). The process per wafer typically lasted between two to three hours. Figures 4.25a and 4.25b show examples of successfully coated wafers. At one of the edges of each coating, thicker white stripes can be noticed. These happen due to increased evaporation on the sides of the blade, leading to formation of particle multilayers when the speed is adjusted for monolayer formation in the blade's center. On the other edge, this effect happened as well (visible in Figure 4.24a, on the right edge of the coating), but to a lesser extent due to uneven parallelism between the blade and the substrate. The influence on uneven parallelism overall caused a gradient in deposition across blade width with multilayers often forming on the left side and voids on the right side of the coating.

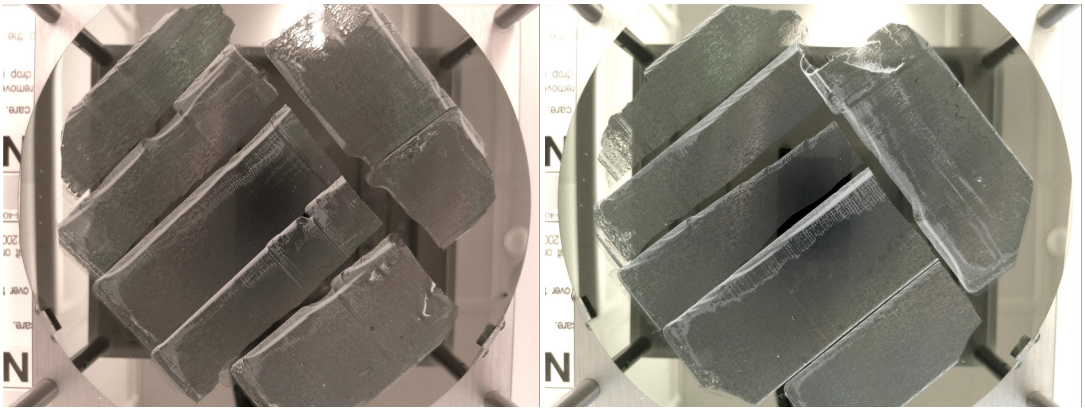

(a) (b)

Figure 4.25: Examples of wafer successfully coated with polystyrene monolayer films.

By using an SEM, additional points can be noticed on the particle monolayers. Firstly, as shown in Figure 4.26, particles show a high degree of orderliness and a hexagonal close packing, as was ideally expected. Upon zooming out and looking at the larger scale picture (shown in Figures 4.27a and 4.27b), it can be noticed that most of the defects come from missing single particles in the film. Additionally, particles form HCP layers in clusters separated by cracks in what would ideally be a uniform film. The cause of these cracks is hypothesized to be happening during the final stage of self-assembly as the film is fully drying, distantly from the meniscus.
Furthermore, as the suspension contains particles with a mean diameter of 1.1 μm, a tendency for particles larger than the nominal diameter to form individual clusters was noticed (therefore the self-assembly process has a size filtering effect). Around these clusters multilayers were formed (shown in Figure 4.28a).
Presence of impurities such as dust particles which can readily be from tens to hundreds of micrometers in

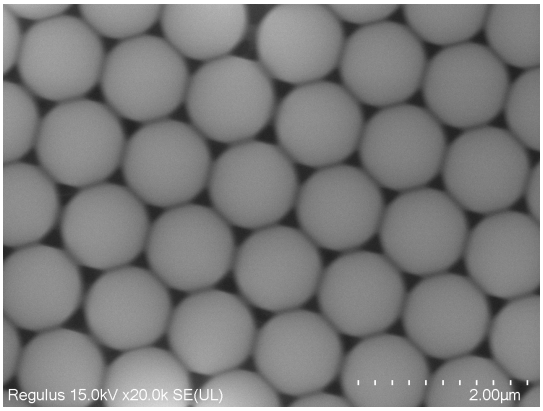

Figure 4.26: Hexagonal close packing of polystyrene microspheres.

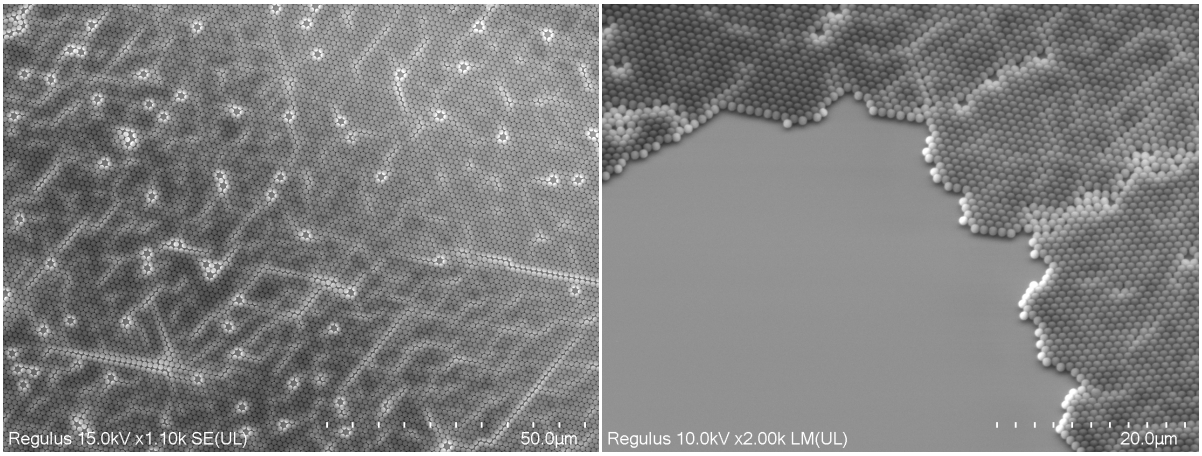

(a) Singular voids and cracks forming HCP clusters (polycrytalline structure).

(b) Evidence of a particle monolayer.

Figure 4.27: Particle monolayers

size (due to the coating being done outside of a cleanroom environment) at the wafer's surface also significantly impedes the self-assembly process and results in a large region around the dust particle being either uncoated or discontinuosly coated by a combination of particle monolayers and multilayers (shown in Figure 4.28b).

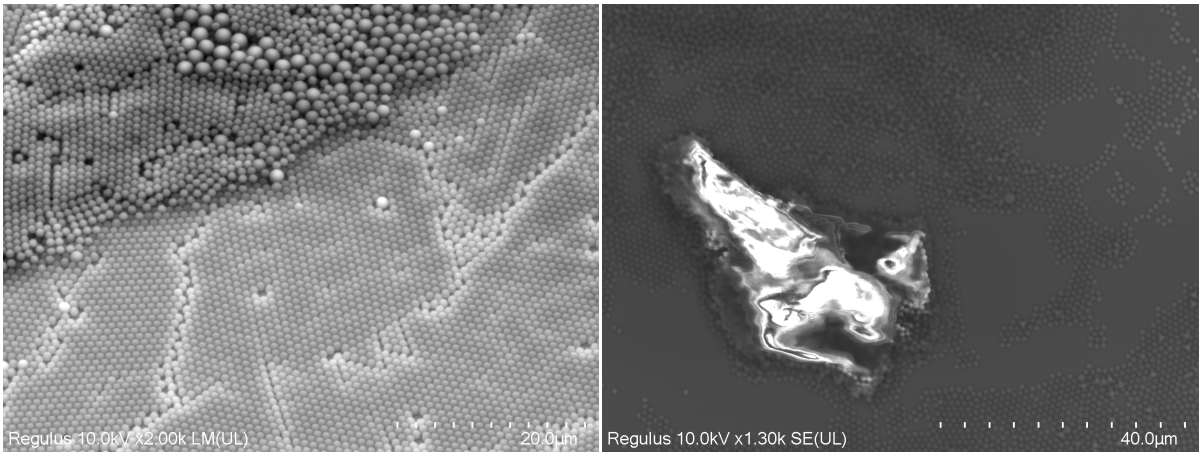

(a) Transition to multilayer around larger particles.

(b) Dust particle impeding assembly.

Figure 4.28: Particle multilayer formation.

Particle size reduction using O_2 plasma

As mentioned before, in order to reduce the particle size and create interparticle spacing O_2 plasma is used (illustrated in Figure 4.20b). O_2 plasma is commonly used in etching polymers and ashing/etching photoresist as the highly energized oxygen ions effectively break chemical bonds in organic substances and form volatile compounds such as CO, CO_2 or H_2O vapour.
Inside EKL, oxygen plasma is available in five different machines: Trikon Omega (RIE, but processing polymerrs is allowed each week from Friday to Tuesday), Alcatel AMS110 (RIE/DRIE, contaminated tool in which processing polymers is allowed), SPTS Rapier (DRIE, but processing polymers is not allowed), TePla 300 (O_2 plasma asher), Diener ATTO (low power O_2 plasma used for surface activation). In all of the RIE/DRIE machines, a 'directionalized' plasma is used (ions are accelerated towards the wafer) by which anisotropic etch profiles are created. Moreover, in all of the machines the wafer is placed on a chuck and there it is clamped (electrostatically). Since the particle coating has been done outside of the cleanroom (where contamination is not as tightly controlled), the risk of potential contaminants on the wafer's backside which would touch the chuck is high (potentially damaging the machine). Additionally, as the particles are etched anisotropically, a deformation of particles' spherical shape is expected.
This leaves a choice of two options. Both TePla 300 and Diener ATTO have a barrel type chamber in which plasma is created. Inside such a chamber, reactive oxygen radicals are present everywhere, but not necessarily with a uniform distribution, which could result in certain regions of the substrate being etched more than others. As TePla 300 is a high power plasma tool used for thoroughly removing photoresists, the non-uniformity is not a large issue as endpoint detection and overetching are used to ensure full removal of any organic contamination. This however makes it unsuitable for being repurposed as a controlled etcher of polystyrene across a 4-inch substrate.
Ultimately, the Diener ATTO tool was chosen to be tested as an etcher for polystyrene. The tool is capable of a maximum 200W, low frequency (40kHz) O_2 plasma generation in a barrel type chamber which would usually be considered as an unsuitable tool for etching. Therefore, it is used exclusively as a surface activation tool for increasing surface energy of materials (increasing hydrophilicity). Through a literature survey, it was found that this tool can in fact also be used as an etcher of polystyrene [81]. In this study, different aspects of O_2 plasma etching were examined (power, frequency, chamber pressure, gas mixture etc.) and it was concluded that through use of this tool, polystyrene can be etched in a controlled manner and without significant shape deformation (as is the case with anisotropic RIE), therefore making it an ideal choice for this purpose. The authors also noticed that a difference exists between the etching mechanisms of LF and RF plasma. They hypothesize that during LF plasma etching, O_2 radicals are able to transfer their kinetic energy to polystyrene particles, which increases their surface temperature resulting in isotropical melting and vaporization. As the particles cool down, by minimizing their surface energy they regain the spherical shape.
For the purposes of this thesis work, Diener ATTO tool was used at 130W power, with a chamber pressure of 0.25 mbar and the O_2 gas flow automatically controlled to maintain the chamber pressure (typically this resulted in gas flows between 8 to 10 sccm). The etching was done in 10 to 15 minute steps in order to determine the etch rate, as it was shown to be dependent on the wafer's positioning inside the chamber due to plasma non-uniformity. The obtained etch rates were in the range of 23 $\frac{nm}{min}$ to 35 $\frac{nm}{min}$, expressed as a reduction of

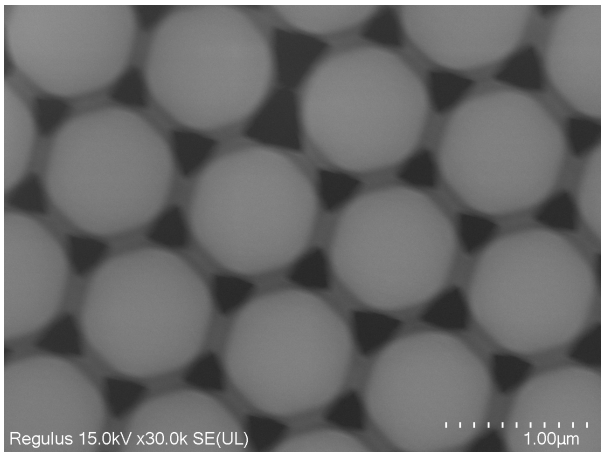

Figure 4.29: Formation of 'bridges' between particles at the start of etching (image taken after 6 minutes of etching).

particle diameter per minute. After determining the etch rate, the wafer was placed again in the chamber and the etching was done again until a particle diameter in the range of 450nm to 500nm was obtained, as not all particles have the same starting diameter. At the start of etching (within first 10 minutes), the particles apart from reducing in size tend to form 'bridges' between between them (shown in Figure 4.29). The formation of these bridges might be attributed to polystyrene particles melting and forming capillary bridges when exposed to O_2 plasma [82]. As the etching is continued, these 'bridges' are being removed and are ultimately broken with the particles being released. After this point, the particle etching continues but the particles also tend to lightly move from their original position (shown in Figure 4.30a). If the etching is continued for too long the hexagonal lattice shape can be completely lost (shown in Figure 4.30b). It was noticed that this effect happens to a significantly lesser extent if the wafer is placed vertically in the chamber on a quartz carrier, instead of horizontally in a glass Petri dish. It is speculated that this is due to better cooling of the wafer when it is not fully in contact with the glass dish (which was substantially heating up during the etching).

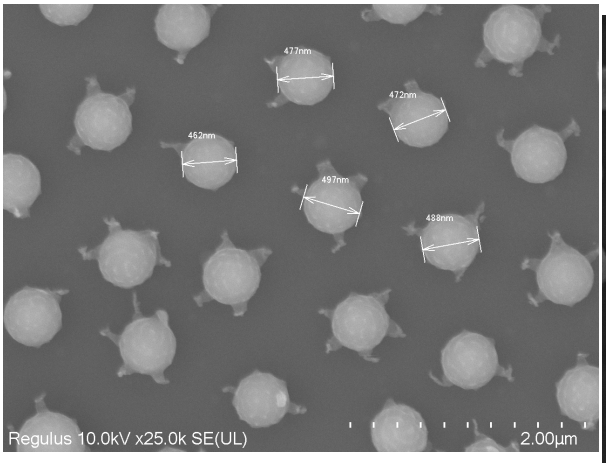

(a) Particles reduced to correct size after 16 minutes preserving hexagonal lattice ordering.

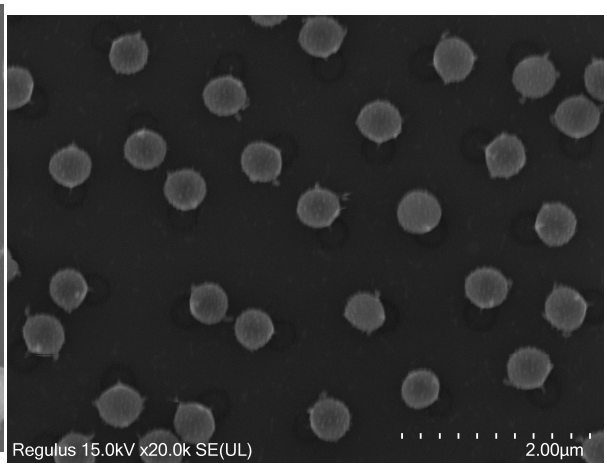

(b) Lost hexagonal packing.

Figure 4.30: Particles after size reduction.

Chromium hard mask fabrication

After reducing the particle size, in order to create a porous mask for etching the Si_xN_y layer it is necessary to deposit a material over the PS particles and the substrate (illustrated in Figure 4.20c), where the particles act as a shadow mask during deposition. For this purpose only a metal layer can be used in EKL (since no ALD machine exists) and it can be deposited either through electron beam evaporation or sputtering.

In the case of sputtering the deposition chamber pressure is high enough to make the mean free path of atoms sputtered off the target short enough to redeposit on the substrate in all directions equally (in the ideal case). With evaporation (thermal or electron beam), the chamber pressure is low which makes the atoms evaporated off the target move unidirectionally towards the substrate. In order to create a mask with controlled pore size evaporation presents a better choice, as the deposition of metal cannot happen in the area under the spherical particle. However, due to long down time of EKL's evaporation tool and the fact that use of the tool introduces contamination, at first sputtering was used. Sputtering gave unrepeatable and generally unsatisfactory results, on which more details can be found in the Appendix.

Therefore, it was ultimately decided to use electron beam evaporation of chromium for use as a hard mask. Cr is chosen as the best available material for use as a hard mask as it is not removed during the etching of Si_xN_y in a fluorine-based plasma. Conveniently, its chemical etchant which is used for Cr removal (a mixture of ceric ammonium nitrate and perchloric or nitric acid) is also highly selective towards Cr and cannot damage the Si_xN_y layer.

Therefore, 30 nm of Cr was evaporated using the CHA Solutions e-beam evaporator (shown in Figure 4.31a). Subsequently, the polystyrene particles were removed by sonication in acetone (at room temperature) for 10 to 20 minutes in order to lift off the Cr (illustrated in Figure 4.20d). A cleanroom swab was used during sonication to mechanically lift off the particles in case acetone was unable to reach an area (it is presumed that longer sonication would anyhow remove all of the polystyrene, but this was a quicker solution). After inspection, the wafers were cleaned in a dedicated HNO_3 bath for 10 minutes, rinsed in DI water and dried.

Through SEM inspection, it was verified that evaporation does not cause virtually any change in the pore diameter and that pore size is ultimately governed by the particle diameter, as was initially expected (shown in Figure 4.31b).

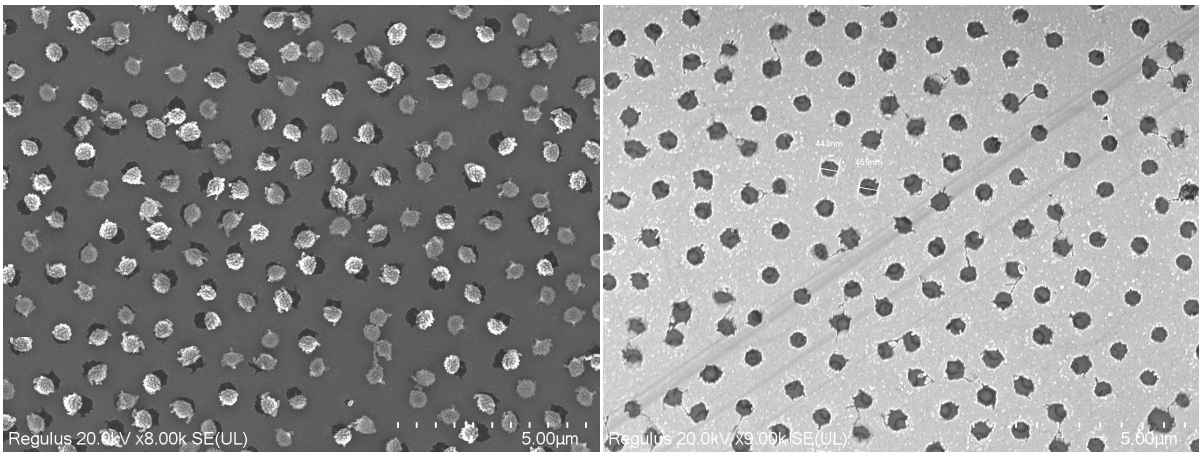

(a) Evaporation of Cr over the particles.

(b) PS particle lift-off.

Figure 4.31: Evaporation of Cr.

However, any particle multilayers completely shadow the Cr deposition, creating large holes in the Cr layer (shown in Figure 4.32). For mitigating this issue, atomic layer deposition (shown in Figure 4.19b) is the preferred option instead of evaporation, but it is an unavailable tool for metals in EKL.

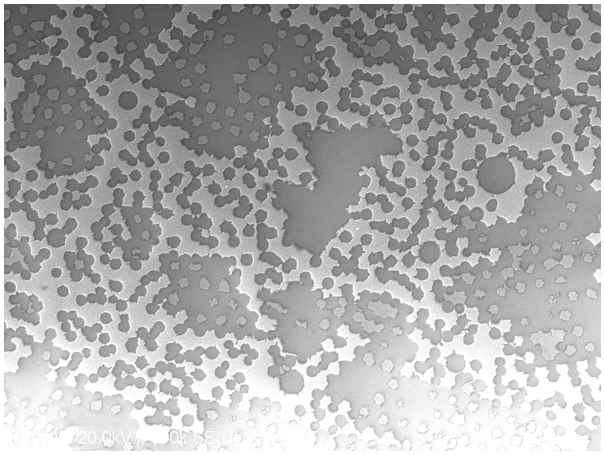

Figure 4.32: Cr layer holes in multilayer.

Pore transfer into Si_xN_y

With a fabricated hard mask it is finally possible to transfer the pore patterns into the underlying Si_xN_y layer. Prior to this step however, a second photoresist mask needs to be made on top which masks the area around the membranes (illustrated in Figure 4.20e). For this purpose, the following photolithography process is used (executed manually due to contamination):

- Manual HMDS pretreatment for 10 minutes to enhance photoresist adhesion
- Manual spin coating of 2.0 μm of nLoF 2020 photoresist using the Brewer Science manual spinner
- Exposure through `Membrane_opening` mask in the SUSS Microtec MA8/SA8 contact aligner for 15 seconds
- Crosslink bake at 110°C for 90 seconds using the manual hotplate

- Manual development using MIF322 developer for 60 seconds

The pore etching was conducted using the AMS110 contaminated RIE/DRIE etcher (illustrated in Figure 4.20f). As the machine is normally used for DRIE and has been repurposed as a dielectric etcher, it unfortunately does not have a CF_4 or C_2F_6 gas line installed, which would otherwise be used for etching Si_xN_y. Therefore, two options were possible for etching Si_xN_y: etching using CH_4 which is normally used for SiO_2 etching or etching using SF_6/C_4F_8 which is normally used for DRIE. Because the layer underlying Si_xN_y is SiO_2, the second option was chosen as it cannot chemically etch SiO_2.
To determine the necessary etching time a test wafer with only an SiO_2/Si_xN_y layer stack was used (with the same layer thicknesses as the process wafers). A time of 2 minutes was sufficient to fully remove the Si_xN_y layer. Use of a test wafer was necessary as precise height profile inspection of sub-500nm pores that should be 150 nm deep is impossible using any of the available measurement tools. For the process wafers, an additional time of 30 seconds was used to reduce the potential risk of not fully opening the pores.
After etching, photoresist was stripped off from the membrane side (using a combination of O_2 plasma and acetone) and the wafers were cleaned. Photoresist was then spray coated in 24 layers over the front side which contains the electrodes (same procedure as for microfludic channel opening in Section 4.3). The wafers were then placed in the commercially available Cr etchant until the Cr layer was fully removed (illustrated in Figure 4.20g). The photoresist coating on the front side was used as protection for the Al contact pad layer, as it can get etched by the Cr etchant (the exact etch rate is unknown, but for precautionary reasons this was done). After removing the Cr layer, the photoresist from the front side was stripped off using acetone.
The fabricated porous membrane pattern can be seen in Figures 4.33a and 4.33b.

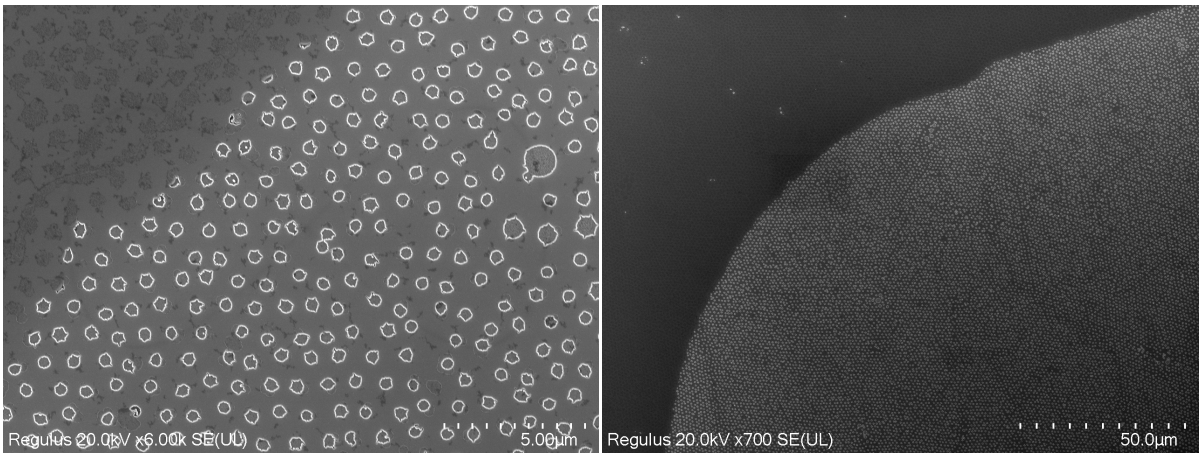

(a) Close up view of the pores, at the membrane edge.

(b) Pores at the membrane edge.

Figure 4.33: Pores after etching and Cr removal.

4.5. Wafer bonding and membrane release

Following the membrane patterning, the penultimate fabrication step of wafer bonding can be undertaken. To achieve this two options were considered: direct bonding (also known as fusion bonding) and adhesive bonding. Direct bonding is commonly utilized in bonding silicon (and silicon-based) surfaces without any intermediate layer. For this method to work, the surface roughness of the wafers needs to be kept below an RMS value of 0.5 Å. Through a literature survey it was seen that such low roughness levels are achievable only by chemical mechanical polishing (CMP) which is unavailable in EKL and potentially destructive to the membrane features or with unused wafers (exposure to any photolithographic process will lead to an increase in surface roughness). For this reason, this method was not attempted and instead only adhesive bonding was considered.
Adhesive bonding uses an intermediate bonding layer which effectively attaches to the surfaces of both substrates and acts as a glue between them. Many different materials can be utilized for this purpose, but it was found that SU-8 generally works best and shows the highest bonding strength out of all photo-patternable materials [83].
SU-8 is a biocompatible negative photoresist, often used in soft lithography for creating transparent structures or moulds. It is generally rarely used for typical photolithography purposes, as it is very difficult to

remove from a substrate if it is fully crosslinked. It is also thermally stable above 300°C, a feature typically unassociated with photoresist. Its chemical and thermal stability however makes it a great choice for wafer bonding applications, as the risk of debonding in subsequent wet processing steps is low (provided that the bonding process is executed well, without voids).
The flowchart for wafer bonding is shown in Figure 4.34.

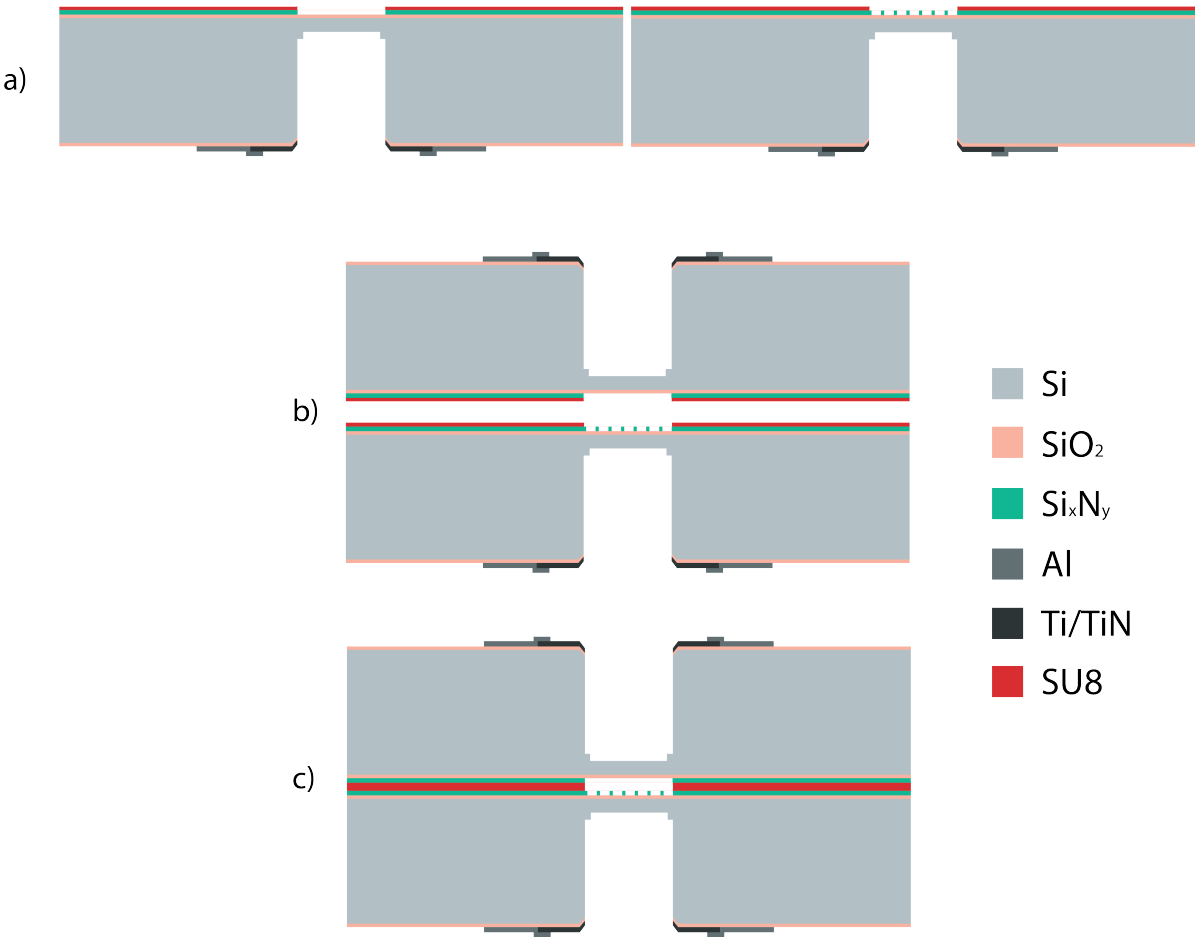

Figure 4.34: Wafer bonding flowchart using SU-8. a) 5μm thick SU-8 layer is applied to both wafers to be bonded, b) wafers are aligned using the AML bonder wafer alignment markers, c) wafers are brought in contact and a force is applied.

Firstly, the wafers were cleaned in a dedicated 99% HNO_3 bath, rinsed in DI water and dried. For applying the SU-8 layer the following photolithography procedure is used:

- Wafer baking at 200°C using a manual hotplate for 5 minutes. This is done to evaporate any water condensed on the wafer's surface which might reduce SU-8 adhesion
- Manual spin coating of a ~5 μm thick layer of SU-8 2005 (3500 rpm, accelerated at 500 RPM/s). Before the spin coating starts, a uniform layer must be applied by slowly pouring SU-8 over the wafer's surface, to minimize nonuniformity caused by inertial movement of SU-8 during the acceleration step
- Soft bake at 95°C using a manual hotplate for 2 minutes
- Exposure through the `Membrane_opening` mask for 25 seconds using the Microtec MA8/SA8 contact aligner
- Post exposure bake at 95°C using a manual hotplate for 3 minutes
- Manual development using PGMEA for 1 minute until all of the features are visible. Immediately afterwards rinse the PGMEA using the sequence IPA-acetone-IPA and dry the substrate using the manual dryer

SU-8 is applied on both wafers which will be bonded (illustrated in Figure 4.34a). In case, the processing of SU-8 is not done immediately before wafer bonding, the SU-8 layer should be rinsed again with IPA before bonding to remove any potential particles which could be detrimental to the bonding.
With the SU-8 applied and its surface cleaned, the wafers are placed in the wafer bonder. Firstly the top wafer is placed on the top chuck, the chamber is closed and the bonder's alignment cameras are aligned to its alignment markers. Once aligned, the chamber is opened again and the bottom wafer is placed on its chuck. The bottom chuck is now actuated in x-y directions until the bottom markers are roughly aligned with the top markers. The bottom wafer is then slowly raised and periodically it is realigned, as the bottom chuck movement is not ideally vertical. When satisfactory alignment is achieved at a close distance between the wafers (illustrated in Figure 4.34b), the wafers can be brought in contact (illustrated in Figure 4.34c).
During the first tests of wafer bonding, the bonding was done using a force of 1kN with the chucks heated to 120°C in atmospheric pressure over 16 hours. The quality of wafer bonding using this procedure generally bad results, with large areas being unbonded as evidenced by Newton ring patterns visible through infrared cameras (shown in Figure 4.35a). Two options were considered for improving the bonding quality: increasing the bonding force and executing the bonding in vacuum. The force was increased to 2.5 kN, 0.5kN below the force recommended for direct bonding in the AML bonder's manual and the chamber was evacuated to a pressure of $1 \cdot 10^{-6}$ mbar. The combined effect resulted in a nearly perfect bonding across the full wafer surface (shown in Figure 4.35b). After the bonding the wafer was baked from 80°C to 150°C on a hotplate, in increments of 10°C each 5 minutes followed by a 20 minute bake at 150 °C to ensure that SU-8 is fully baked.

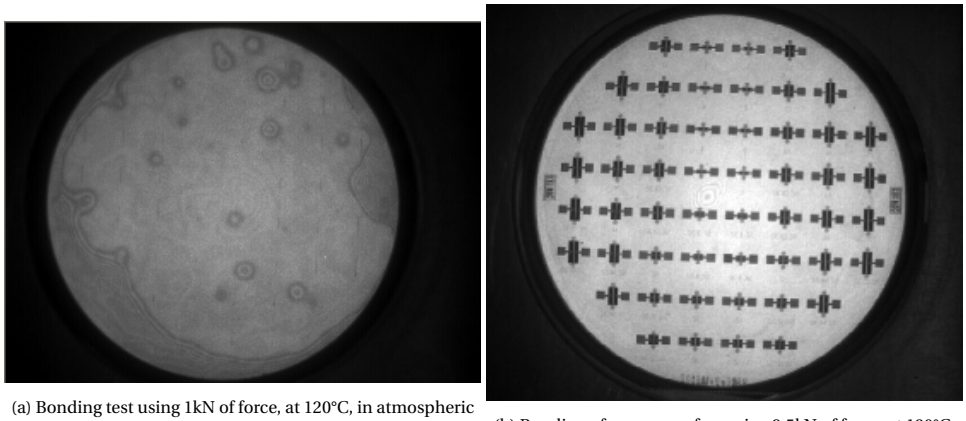

(a) Bonding test using 1kN of force, at 120°C, in atmospheric pressure.

(b) Bonding of process wafers using 2.5kN of force, at 120°C, in vacuum.

Figure 4.35: Examples of unsuccessful and successful wafer bonding.

Following the wafer bonding, the final step of membrane release was performed. The flowchart for this procedure is shown in Figure 4.36.
Due to wafer contamination, AMS110 needed to be used for this step. The same photolithography process involving spray coating was used as described in Section 4.3. The remaining ~30 μm of Si were then removed by careful DRIE etching in 30 second increments, unloading the wafer from the chamber after each etching. This was necessary because wafers are bonded by a poorly thermally conductive SU-8 layer, making the cooling of the wafer on the platen inefficient. This results in photoresist burning with any etch time longer than 30 seconds. Repeating the process six times (total of three minutes) results in fully etching the Si layer. Si residues were removed by short (typically 10 to 15 seconds) exposures to pure SF_6 plasma at 0W platen power, resulting in no additional acceleration of radicals which could damage the membrane.
Photoresist was then stripped off and the process was repeated on the other side of the wafer, until the Si_xN_y/SiO_2 membrane stack was fully released as illustrated in Figure 4.36b. (showing characteristic buckling due to compressive stress of the SiO_2 layer).
For removing the final SiO_2 layer, photoresist was now again applied to the other side of the wafer (without removing the layer that was used for last etching), this time being baked in a Memmert convection oven as direct contact with the hotplate is not possible. The exposure and development process was repeated the same as before (but using a carrier wafer on the contact aligner in order not to destroy the membranes by the vacuum chuck), being careful not to destroy the membrane by excessive turbulent flows during development and rinsing.

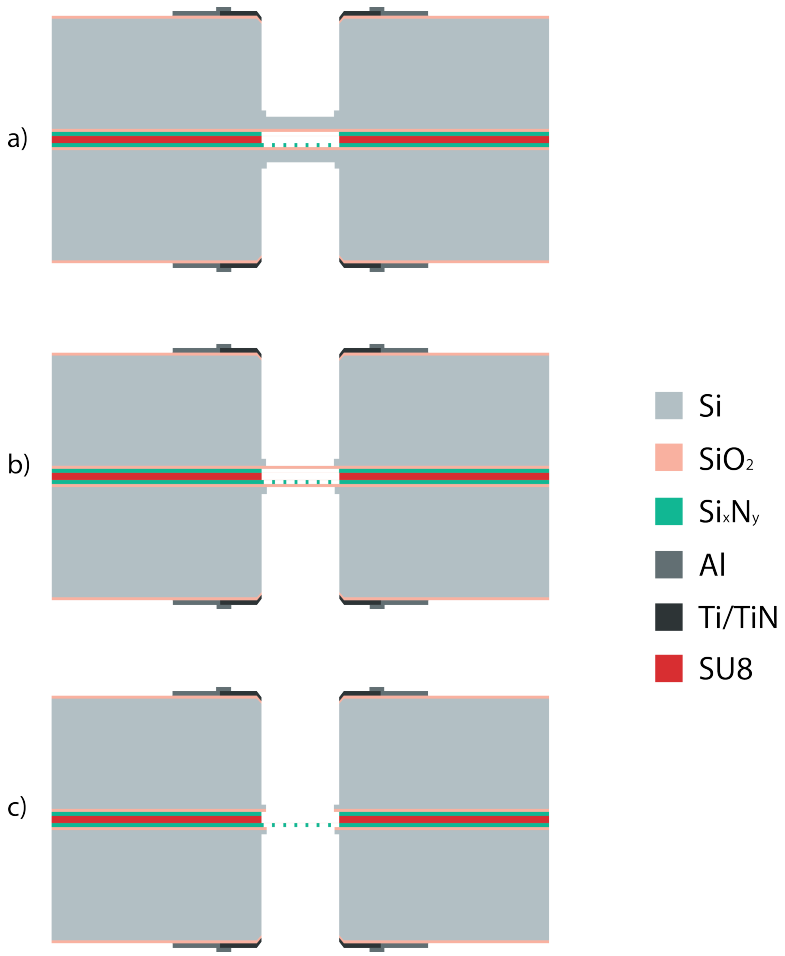

Figure 4.36: Membrane release flowchart. a) remainining silicon is removed using a combination of DRIE and dry isotropic etching, b) SiO_2 etch stop layer is removed using BHF, c) the membrane is released finishing the fabrication.

Finally, the wafers with photoresist applied on both sides were placed in a BHF 1:7 solution for 90 seconds to remove the SiO_2 etch stop layer, bringing the process to a finish. An example of a fully released membrane is shown in Figure 4.37.

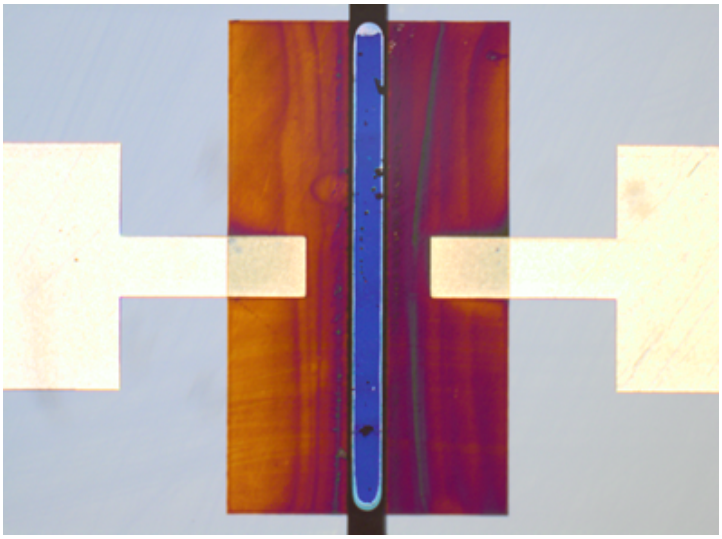

Figure 4.37: Fully released 150 nm thick, porous Si_xN_y membrane.

Summary

In this Chapter, the full fabrication flow required for making the device designed in Chapter 3 was given. The process was started by fabricating electrodes on slanted sidewalls. This involved first creating a slanted sidewall structure on the wafer's surface using wet anisotropic etching of silicon with TMAOH. On top of the sidewall structures a TiN/Ti layer was deposited and patterned for later use as TEER measurement electrodes. Al was deposited and patterned for wire bonding pads.
After fabricating the sidewall electrodes, the microfluidic channels were partially opened using a two-step DRIE process, which creates a stepped structure between channel's inlets/outlets and the membrane area. The membrane was patterned utilizing nano/microsphere lithography, a process previously unexecuted within EKL/ECTM for which each of the steps was thoroughly tested. The process flow resulted in sub-500nm pore sizes and a porosity between 10% and 20%, going beyond the limits of the available wafer stepper. The achievable feature size (in this case for pores) is limited mainly by the size of available polystyrene particles, making the method flexible for even lower feature sizes in case periodic structures such as pore arrays are desired. Ultimately, two wafers were bonded using SU-8 creating a two-channel microfluidic device. The membranes were released by a combination of DRIE and isotropic Si etching.

5

Testing

5.1. Enclosure and PCB design

The two-channel microfluidic chip fabricated in Si does not by itself present a functional device for conducting impedance spectroscopy measurements as the fluidic channels are not enclosed from their top side. For this reason an enclosure was designed that ensures that the membrane area stays transparent, while the channels are fully enclosed. The designed enclosure consists of two 0.5 mm thick laser cut polymethyl methacrylate (PMMA) parts which contain the fluidic inlets/outlet and cover the top and bottom microfluidic channel. To reliably attach these parts to the chip, 80 μm thick laser cut pressure sensitive adhesive (PSA) layers are used. The layers also contain a cutout in the shape of the channel to not introduce any additional opacity above the channel area. With these four layers the chip is enclosed but for easier later use during testing, two 3D-printed parts were designed and fabricated using a high resolution resin 3D printer. The 3D-printed parts enable microfluidic connections from a single side and contain screw openings for mounting stand-offs. Similarly, the PMMA-enclosed chip was sealed to the 3D-printed parts using PSA and the 3D-printed parts were sealed together using PSA, thereby ensuring that no fluid leakage occurs. A disassembled view of the enclosure is shown in Figure 5.1a.

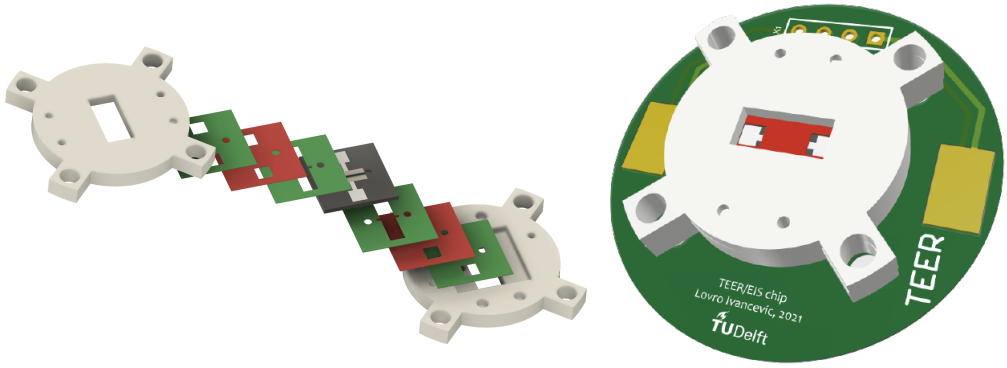

(a) Enclosure of the chip (white parts are 3D printed, green parts are laser cut PSA, red parts are laser cut PMMA).

(b) PCB designed for chip testing.

Figure 5.1: Parts designed for chip testing.

A simple PCB was designed for interfacing the enclosed chip with an impedance spectroscopy system (shown in Figure 5.1b). It contains, same as the chip, large wire bonding pads from both sides and it is mechanically secured with the enclosure through the same screw holes used for mounting stand-offs. The signals are routed to a four-pin header connector placed on the PCB's top side to enable easier use during measurements.

6

Conclusion and Future Perspective

Measurement of transepithelial/transendothelial electrical impedance offers a noninvasive and often real-time assessment of physiological barrier functionality. However, in all of the OoC models reported to date, little attention was given to electrode geometries through which linear measurements can be achieved without a need for correction functions. In this thesis, a goal was set to design and fabricate a microfluidic device for measuring impedance of blood-brain barrier cell cultures which has highly uniform measurement sensitivity, without compromising transparency. A sidewall electrode design was proposed, as it offers completely unobstructed view of the cell culture. Furthermore, the use of a nanometer-scale thin, highly porous and highly transparent silicon nitride membrane was proposed instead of a commonly used polymer-based membrane with the intent of enabling better cell-cell interactions in a blood-brain barrier cell co-culture model.

The design was optimized by determining optimal sidewall electrode and microfluidic channel geometry. Electrodes on short slanted sidewalls have been shown to give an almost unitary sensitivity value across the full cell culture area, whilst retaining fabrication feasibility. Fluid flow simulations were further conducted to verify that the proposed design, which was optimized mainly around electrode geometry, does not cause inadequate microfluidic behaviour which ultimately governs the growth and proliferation of cultured cells.

A full fabrication flow was designed and executed within the Else Kooi Laboratory. Fabrication flow consisted of many standard silicon MEMS processing steps, but also included utilization of nanosphere lithography through convective self-assembly for fabricating a sub-500nm pore size membrane. All of the aspects of the process were thoroughly tested until a final flowchart was derived. An enclosure for the microfluidic channel was designed together with a PCB enabling device testing.

The electrode fabrication flow was shown to be relatively quick and repeatable, especially due to optimized use of spin coating in a trench with slanted sidewalls and through use of a 'TiN-first' metal deposition scheme which enabled subsequent Al layer to be etched using PES. Two-step microfluidic channel opening was also shown to be a well-developed process and required only a short isotropic etch at the end to fully remove the residual Si pillars. Membrane patterning process using NSL was shown to be executable, but at this stage it cannot be considered a reliable production method for larger scale fabrication as achieving reasonably high 'self-assembly yield' across wafer scale using the current doctor blading setup requires large amounts of manual adjustments. The wafer bonding using SU-8 was shown to be effective when paying careful attention to wafer's cleanliness and when executed in a vacuum environment. Final step of membrane release was shown to be successful, but unfortunately it required multiple photolithography steps that are done with the sole purpose of protecting the TiN/Ti electrodes when removing SiO_2 using BHF. With this in mind, it should also be accounted that the photolithography steps for membrane release are just a repetition of the step done during partial microfluidic channel opening.

Unfortunately, due to unavailability of the DRIE tool used for the final processing step of membrane release, the process was not able to be brought to a successful finish. All of the aspects regarding the tool use were verified on other wafers, meaning that as soon as the tool is working again the process can be finished. This also implied that no testing was possible, although through theoretical analysis and simulation results the device is expected to work as anticipated. Ultimately, prolonged blood-brain barrier cell testing on silicon nitride membranes is necessary to verify device functionality and further facilitate research in the domain of ultrathin silicon-based membranes for OoC applications.

Future perspective

Device modification for other tissues The electrode topology obtained through simulations during this thesis work showed a remarkably uniform measurement sensitivity, meaning that in the future the device's use can be extended to other OoC-integrated barrier models where TEER measurement functionality is needed, such as a gut-on-a-chip. In this case a polymer membrane should instead be used due to known influence of mechanical stress on gut epithelial cells. If PDMS is used for this purpose, integration into the determined process flow should not present a significant issue.

Improvements in nanosphere lithography The use of nanosphere lithography for going beyond the limits of photolithography was proven possible. The acquired results show potential for technique's use in many different domains of microfabrication when periodic structure arrays are required. The coating setup is still not fully suited for wafer-level use, but it does prove useful for research-based fabrication. With upgrades like an improved blade holder and an automatized x-y movement stage the results are expected to be more repeatable and possibly upscaled to a wafer-level coating. Spin coating of polystyrene particles across 4-inch wafers could be investigated as it was shown to be possible previously although with a large material waste [84]. The use of a ring surrounding the wafer's perimeter (potentially made from photoresist such as in [78]), might aid in reducing waste.

Process flow improvements Improvements in other aspects of the process flow are unfortunately limited by contamination control. If the process is in the future executed in a cleanroom which allows use of contaminating materials (such as Kavli Nanolab), use of gold electrodes could significantly simplify the final steps of processing as discussed in Chapter 4 with virtually no repercussions to the already determined process flow. In case additional equipment is available, in order to improve device yield which is currently limited mainly by the self-assembly process, electron beam, laser or nanoimprint lithography could be utilized to fabricate smaller pores, as they are proven methods for repeatable larger scale fabrication.

Acknowledgments

I would like to express my most sincere gratitude to my daily supervisor Hande Aydoğmuş and my mentor dr. Massimo Mastrangeli. Hande's friendly attitude, curiosity and willingness to help in any step of the way, extending beyond the duties of a thesis supervisor, made the past year at ECTM a delightful experience, even during difficult times. Massimo's approachability and readiness to hear and give feedback to my ideas has motivated me to push my conceptions into reality. They have together sparked my interest in microfabrication and organ-on-chip technology, given me invaluable knowledge and allowed me to explore my ideas which I am truly thankful for.

The fabrication of the device presented in this thesis proved to be quite challenging. I would want to thank Paolo, who always went above and beyond to help me and whose immense effort to make EKL a better place for all users will always be appreciated. Paolo's quick and clever solutions helped me numerous times to solve different fabrication issues and his physics-based outlook on microfabrication has given me precious knowledge on how different machines work and what is possible to achieve with them. I would further like to thank Aleksandar and Bruno for their strong dedication to fixing cleanroom machines which has ultimately enabled the fabrication of this device. Together with them, I would like to thank the technicians of EKL, who have always been there to answer my questions on the use of machines and have helped me resolve issues quicker. I would also like to extend my gratitude to Pauline and Eugene from Kavli Nanolab for readily helping me with Cr etching.

My time at ECTM would not have been the same had I not met many wonderful people. I would want to thank Milica, Paul, Shriya and Nele for always being ready to help in and out of the cleanroom and raise my spirits when things were not going well. I would further want to thank Joost for his help with wafer bonding, Bjorn for his help on designing and fabricating the chip enclosure and Filip for helping out with any technical issues outside the cleanroom. I'd like to thank Sudiksh, Shivendra, Secil, Matthew, Thijs, Vieri, Jilian and Luutzen - my office and cleanroom buddies, for all of the interesting discussions and fun experiences we've had in the past year.

I would like to thank all of my friends in the Netherlands and back home in Croatia who were supporting me through every part of my studies at TU Delft.

In the end, none of this would have been possible without the unconditional love and support from my family. They have always encouraged me to follow my passions and taught me to always do everything to the best of my ability, a value I deem the most important in life. I would not be where I am today without them and I am eternally grateful for that.

Lovro Ivančević
Delft, October 2021

A

Appendix

A.1. Membrane rupture by DRIE

As was already seen in Chapter 3, in static conditions only the intrinsic stress of the SiO_2/Si_xN_y multilayer and pores significantly influence the membrane's mechanical strength. However during a plasma etching process, additional stress is generated in the substrate that is being etched (for example due to the substrate being charged), which is both theoretically and experimentally difficult to quantify and use as an input for simulation. For this reason, prior to starting the fabrication a test was done to examine whether a Si_xN_y membrane can be released using DRIE in the SPTS Rapier etcher.
On top of a 300μm thick <100> high resistivity DSP Si wafer, 150 nm of thermal oxide was grown and 150 nm of LPCVD low-stress (250 MPa) Si_xN_y was deposited. The layers were removed from one side of the wafer and a 6 μm thick PECVD SiO_2 layer was deposited and patterned using the `Membrane_opening` mask. No pore patterning was done on the Si_xN_y layer. After 350 cycles of etching using the `EKL_Smooth` recipe, the membranes across the wafer were almost released (as shown in Figure A.1a). As can be seen from Figure A.1b the etch profile of the `EKL_Smooth` recipe results in the membrane no being released fully from the sides (the etch profile resembles a U-shape). To mitigate this issue the `EKL_FlatBottom` recipe was used. Showing good results, it was decided to use only `EKL_FlatBottom` recipe for final processing (described in Section 4.3). Afterwards, the SiO_2 layer was removed by a 90 second BHF 1:7 etch.

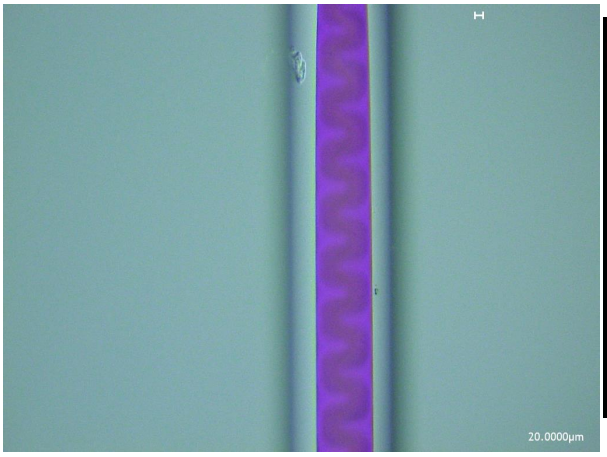

(a) Released membrane.

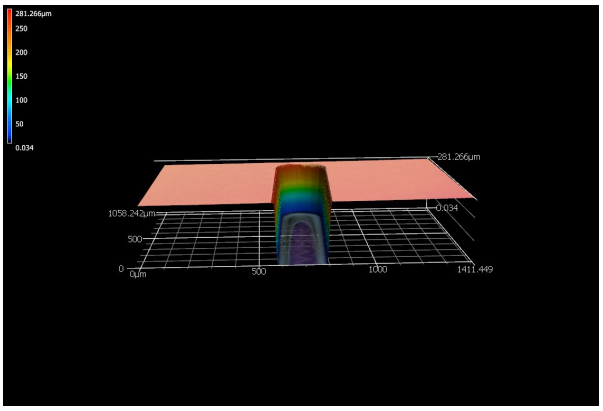

(b) Etch profile of the EKL_Smooth recipe leads to membrane being only partially released.

Figure A.1: Membrane release by DRIE.

To verify transparency of Si_xN_y layer, a rudimentary verification test was used by placing the wafer on a clean-room wipe and turning the focus knob of a bright field microscope until the focal plane reached the surface of the wipe as shown in Figures A.2a and A.2b.

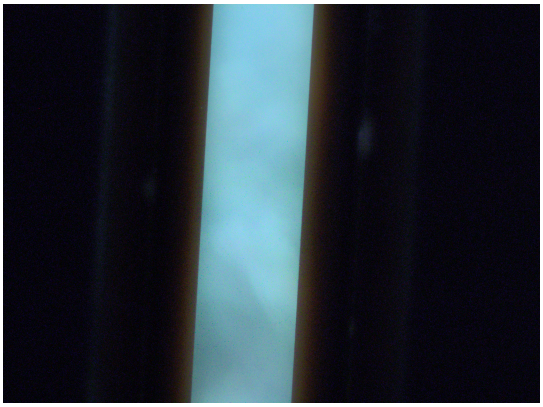

(a) Focal plane above the wipe surface, as viewed through the Si_xN_y membrane.

(b) Focal plane at the wipe surface, as viewed through the Si_xN_y membrane.

Figure A.2: Membrane transparency test.

A.2. Sputtering Ti over polystyrene

During the long down time of the CHA Solutions e-beam evaporator, many trials have taken place in order to try and utilize sputtering as an alternative method for creating a porous mask pattern. The metal that was chosen for this is Ti as it is a better 'green metal' choice for hard mask use than Al (which is not allowed to use due to it sputtering off and damaging the plasma etching chamber).
Firstly, a 50 nm thick layer of Ti was sputtered on a blank wafer using low power, low temperature DC sputtering (1kW, 25°C) to determine it's etch rate when exposed to a C_2F_6 plasma used for etching Si_xN_y in the Drytek Triode etcher. After 40 seconds (the etch time required for fully etching 150 nm of nitride as determined in Section 3.11b), approximately 15nm of Ti remained (determined through sheet resistance change), setting a lower limit for minimum thickness of Ti layer to be 35 nm (making the selectivity ratio to Si_xN_y about 5:1). To reserve a safety margin, 50 nm thickness was kept for the subsequent tests.
After depositing PS particles and reducing their size using O_2 plasma (as described in Section 4.4), 50 nm of Ti was sputtered using the same method as before. As seen in Figures A.3a and A.3b, after lift-off the results were mixed (lift-off was as expected difficult to do without mechanically scrubbing off the particles, which also damaged the Ti film). In certain areas of the wafer, the particle shape was relatively nicely transferred into the Ti layer (although the circular shape was largely lost). In other areas the Ti layer completely covered the area shaded by the particles resulting in too small openings. What's more, after etching such a layer using C_2F_6 plasma, the pore array pattern did not follow mask pattern and resulted in pores becoming larger and sometimes merging, presumably due to the etching not being ideally anisotropic and the selectivity of the masking layer not being high enough.

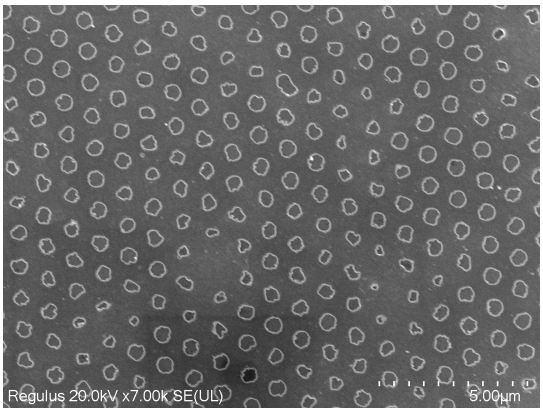

(a) Pores in Ti layer relatively closely following the PS particle deposition.

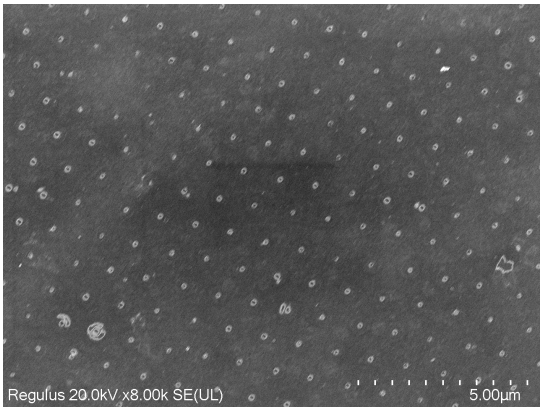

(b) Almost fully covered pores after Ti sputtering.

Figure A.3: Lifting off Ti sputtered over polystyrene.

In an attempt to improve the anisotropicity of sputtering, sputtering chamber pressure was kept lower to decrease the mean free path of Ti atoms and make the method resemble evaporation. The minimum attainable pressure in the machine was 8 mTorr (compared to 25 mTorr during normal sputtering), which was not enough to produce any noticeable difference in sputtering anisotropicity. Other methods, such as increasing the target power were not tested as they are not allowed to be used when sputtering over a polymer.
Viewing that there is little flexibility in sputtering over a polymer, it was attempted to heat up the particle-covered wafer with the intention of reflowing them which would increase their contact surface area. The wafers were for that purpose heated on a hotplate and convection oven at ~98°C in the range of 1 to 6 minutes. After multiple tests, it was concluded that this method does not produce any considerable improvement over any of the previous attempts i.e. there is virtually no change in surface area. This might be due to too low temperature used or incorrect temperature reading of the tools as it is important that substrate heating occurs just above the glass transition temperature of polystyrene. Since the evaporator tool was fixed at the time this process was being tested, no further use of sputtering was done (and hence the particle reflow). It still might present an interesting idea for future research as if this was possible to do, a contamination-free process would be achievable.

A.3. Extended list of reviewed physiological barrier models

Table A.1: Overview of the examined barrier models

Authors	**Year**	**Modelled barrier and used cell culture**	**Assessment methods**	**TEER** $[\Omega \cdot cm^2]$	**Tracer permeability** $[cm/s]$	**Membrane material (pore size and thickness)**	**Electrode configuration**	**Note**
Cucullo et al. [85]	2002	BBB (bovine aortic EC + glial cells)	TEER	500	X	Hollow fiber (0.65 μm pores with 200μm thickness)	two probe	First BBB TEER measurement in a dynamic device
Booth et al. [29][30]	2012	BBB (b.End3 EC + C8D1A astrocyte)	TEER, fluorescent tracers, TJ staining	>150	~$3 \cdot 10^{-6}$ (FD4)	PET (0.4 μm pores with 10μm thickness)	four probe	First 2D microfluidic BBB model with relevant shear stress
Kim et al. [33]	2012	Gut (Caco-2 EC)	TEER, fluorescent tracers,TJ staining	>3000	~$2 \cdot 10^{-7}$ (FD20)	PDMS (10 μm pores with 30 μm thickness)	two probe	Cyclic strain mimicking peristaltic movements
Achyuta et al. [86]	2013	BBB (RBE4 EC + glial cells)	fluorescent tracers, TJ staining	X	~25% of empty device permeability	PC (8 μm pores)	X	Open neural chamber for easy manipulation and imaging
Griep et al. [31]	2013	BBB (hCMEC/D3)	TEER/EIS, TJ/nucleus staining	>30	X	PC (0.4 μm pores)	two probe	Use of inert electrodes and EIS
Prabhakarpandian et al. [87]	2013	BBB (RBE4 EC + astrocyte conditioned medium (ACM))	fluorescent tracers, TJ staining	X	~10% of empty device permeability	silicon pillars	X	Use of silicon pillars for separating EC/ACM chambers instead of a membrane

Table A.1: Overview of the examined barrier models

Authors	**Year**	**Modelled barrier and used cell culture**	**Assessment methods**	**TEER** $[\Omega \cdot cm^2]$	**Tracer permeability** $[cm/s]$	**Membrane material (pore size and thickness)**	**Electrode configuration**	**Note**
Brown et al. [88]	2015	BBB (primary hBMEC + hiPSC neurons + primary astrocytes + primary pericytes)	TEER/EIS, fluorescent tracers, TJ staining	>30000	not given	PC (0.2 μm pores)	four probe	Remarkably high TEER values (higher than in vivo) due to a large number of cells and non-uniform current density
Odijk et al. [32]	2015	Gut (Caco-2 EC)	TEER	>1000	X	PDMS	two probe	Analysis on TEER nonlinearity
Kilic et al. [89]	2016	BBB (immortalized BMECs and iPSC-derived astrocytes and neurons)	TEER, fluorescent tracers, TJ staining	not given	not given	PDMS (5 μm pores with 10 μm thickness)	two probe	Analysis of chemotaxis
Walter et al. [34]	2016	BBB (hCMEC/D3), Gut (Caco-2), Lung (A549)	TEER, fluorescent tracers, TJ staining	>25 for hCMEC/D3	$\sim 1 \cdot 10^{-6}$ (FD4) for BBB	PC (0.45 μm pores with 23 μm thickness)	four probe	Use of large transparent gold electrodes
Adriani et al. [90]	2017	BBB (hCMEC/D3 + astrocytes and neurons in hydrogels)	fluorescent tracers, TJ staining	X	$\sim 2 \cdot 10^{-5}$ (FD10)	PDMS trapezoids	X	Hydrogel co-culture for drug screening and BBB crossing

Table A.1: Overview of the examined barrier models

Authors	**Year**	**Modelled barrier and used cell culture**	**Assessment methods**	**TEER** $[\Omega \cdot cm^2]$	**Tracer permeability** $[cm/s]$	**Membrane material (pore size and thickness)**	**Electrode configuration**	**Note**
Henry et al. [36]	2017	Gut (Caco-2 EC) and Lung Barrier	TEER/EIS	1500/cm^2	X	PET (0.4 μm pores)	four probe	Transparent gold electrodes partially covering the channel. Due to non-uniform current, values are reported in Ω
Wang et al. [35]	2017	BBB (hiPSC-derived EC + rat astrocytes)	TEER, fluorescent tracers, TJ staining	>2000	$\sim 1 \cdot 10^{-7}$ (FD4)	PET (0.4 μm pores)	four probe	Highest reported TEER values due to use of iPSCs. It was also shown that for iPSC-derived BMECs, shear stress does not influence barrier integrity.
vd Helm et al. [37]	2019	Gut (Caco-2 EC)	TEER/EIS	X	X	X	four probe	Lumped element analysis and correction factor for non-uniform current distribution with small electrodes
Mossu et al. [38]	2019	BBB (CD34+-derived ECs + pericyte conditioned medium (PCM))	fluorescent tracers, TJ staining	X	$\sim 5 \cdot 10^{-6}$ (Lucifer yellow)	SiN ($\sim 50nm$ pore size with $50nm$ thickness)	X	First use of SiN membrane for examining T-cell trafficking over BBB

Table A.1: Overview of the examined barrier models

Authors	**Year**	**Modelled barrier and used cell culture**	**Assessment methods**	**TEER** $[\Omega \cdot cm^2]$	**Tracer permeability** $[cm/s]$	**Membrane material (pore size and thickness)**	**Electrode configuration**	**Note**
Salminen et al. [91]	2019	Vascular endothelium (HUVECs)	TJ staining	X	X	SiN (dual scale, ~50nm and 3μm pore size with 100nm thickness)	X	Studying vascular transmigration of neutrophils
Ahn et al. [92]	2020	BBB (HBMECs + human pericytes + astrocytes in a hydrogel)	TEER, fluorescent tracers, TJ staining	~150	~1 $\cdot$ 10^{-6} (FD4)	PC (8 μm pores with 7μm thickness)	four probe	Studying nanoparticle delivery through BBB. Authors denote that TEER values are incorrect due to uneven current distribution
Hudecz et al. [40]	2020	BBB (hCMEC/D3 + human astrocytes)	fluorescent tracers, TJ stainig	X	1.5 $\cdot$ 10^{-6} (FD4)	SiN (0.5μm pore size with 400nm thickness)	X	Studying nanoparticle translocation across BBB with live imaging
Buzhdygan et al. [41]	2020	BBB (HBMECs or hCMEC/D3)	ECIS, fluorescent tracers, RT-PCR	X (only change is reported)	2.5 $\cdot$ 10^{-6} (FD4)	Transwell PET(0.4 μm pores) and a 3D microvascular mimic	two probe ECIS	Studying effect of SARS-CoV-2 spike protein exposure to BBB

Bibliography

[1] C. H. Song and J. W. Han, "Patent cliff and strategic switch: exploring strategic design possibilities in the pharmaceutical industry," *Springerplus*, vol. 5, no. 1, p. 692, 2016.

[2] J. W. Scannell, A. Blanckley, H. Boldon, and B. Warrington, "Diagnosing the decline in pharmaceutical rd efficiency," *Nat Rev Drug Discov*, vol. 11, no. 3, pp. 191–200, 2012.

[3] A. D. Hingorani, V. Kuan, C. Finan, F. A. Kruger, A. Gaulton, S. Chopade, R. Sofat, R. J. MacAllister, J. P. Overington, H. Hemingway, S. Denaxas, D. Prieto, and J. P. Casas, "Improving the odds of drug development success through human genomics: modelling study," *Sci Rep*, vol. 9, no. 1, p. 18911, 2019.

[4] L. A. Low, C. Mummery, B. R. Berridge, C. P. Austin, and D. A. Tagle, "Organs-on-chips: into the next decade," *Nat Rev Drug Discov*, 2020.

[5] G. Rossi, A. Manfrin, and M. P. Lutolf, "Progress and potential in organoid research," *Nature Reviews Genetics*, vol. 19, no. 11, pp. 671–687, 2018.

[6] M. Mastrangeli, S. Millet, t. O. partners, and J. van den Eijnden-van Raaij, "Organ-on-chip in development: Towards a roadmap for organs-on-chip," 2019.

[7] D. Huh, B. D. Matthews, A. Mammoto, M. Montoya-Zavala, H. Y. Hsin, and D. E. Ingber, "Reconstituting organ-level lung functions on a chip," *Science*, vol. 328, no. 5986, pp. 1662–1668, 2010.

[8] D. E. Ingber, "Reverse engineering human pathophysiology with organs-on-chips," *Cell*, vol. 164, no. 6, pp. 1105–1109, 2016.

[9] W. Z., H. X., Q. H., and C. P., "Global trends of organoid and organ-on-a-chip in the past decade: A bibliometric and comparative study," *Tissue Engineering Part A*, 2020.

[10] N. Franzen, W. H. van Harten, V. P. Retel, P. Loskill, J. van den Eijnden-van Raaij, and I. J. M, "Impact of organ-on-a-chip technology on pharmaceutical rd costs," *Drug Discov Today*, vol. 24, no. 9, pp. 1720–1724, 2019.

[11] H. Kadry, B. Noorani, and L. Cucullo, "A blood-brain barrier overview on structure, function, impairment, and biomarkers of integrity," *Fluids Barriers CNS*, vol. 17, no. 1, p. 69, 2020.

[12] A. D. Wong, M. Ye, A. F. Levy, J. D. Rothstein, D. E. Bergles, and P. C. Searson, "The blood-brain barrier: an engineering perspective," *Front Neuroeng*, vol. 6, p. 7, 2013.

[13] X. Yu, C. Ji, and A. Shao, "Neurovascular unit dysfunction and neurodegenerative disorders," *Front Neurosci*, vol. 14, p. 334, 2020.

[14] M. O. Romanitan, B. O. Popescu, S. Spulber, O. Bajenaru, L. M. Popescu, B. Winblad, and N. Bogdanovic, "Altered expression of claudin family proteins in alzheimer's disease and vascular dementia brains," *J Cell Mol Med*, vol. 14, no. 5, pp. 1088–100, 2010.

[15] A. Armulik, G. Genove, M. Mae, M. H. Nisancioglu, E. Wallgard, C. Niaudet, L. He, J. Norlin, P. Lindblom, K. Strittmatter, B. R. Johansson, and C. Betsholtz, "Pericytes regulate the blood-brain barrier," *Nature*, vol. 468, no. 7323, pp. 557–61, 2010.

[16] M. Pekny and M. Pekna, "Astrocyte reactivity and reactive astrogliosis: costs and benefits," *Physiol Rev*, vol. 94, no. 4, pp. 1077–98, 2014.

[17] M. van der Helm, *Electrical and microfluidic technologies for organs-on-chips Mimicking blood-brain barrier and gut tissues.* PhD thesis, University of Twente, 2018.

[18] H. H. Hussing and K. Zerahn, "Active transport of sodium as the source of electric current in the short-circuited isolated frog skin," 1950.

[19] H. U., F. M., K. K.M., and W. M., "Bovine and porcine large intestine as model epithelia in a student lab course," *Institut fur Klinische Physiologie, Klinikum Steglitz der Freien Universitat Berlin.*

[20] M. Amini, J. Hisdal, and H. Kalvoy, "Applications of bioimpedance measurement techniques in tissue engineering," *J Electr Bioimpedance*, vol. 9, no. 1, pp. 142–158, 2018.

[21] L. L. Crowell, J. S. Yakisich, B. Aufderheide, and T. N. G. Adams, "Electrical impedance spectroscopy for monitoring chemoresistance of cancer cells," *Micromachines (Basel)*, vol. 11, no. 9, 2020.

[22] D. T. Price, *MEMS and electrical impedance spectroscopy (EIS) for non-invasive measurement of cells*, pp. 97–119. 2012.

[23] T. Schmiedinger, S. Partel, T. Lechleitner, O. Eiter, D. Hekl, S. Kaseman, P. Lukas, J. Edlinger, J. Lechner, and T. Seppi, "Interdigitated aluminium and titanium sensors for assessing epithelial barrier functionality by electric cell-substrate impedance spectroscopy (ecis)," *Biomed Microdevices*, vol. 22, no. 2, p. 30, 2020.

[24] Y. Xu, X. Xie, Y. Duan, L. Wang, Z. Cheng, and J. Cheng, "A review of impedance measurements of whole cells," *Biosens Bioelectron*, vol. 77, pp. 824–36, 2016.

[25] L. D. Robilliard, D. T. Kho, R. H. Johnson, A. Anchan, S. J. O'Carroll, and E. S. Graham, "The importance of multifrequency impedance sensing of endothelial barrier formation using ecis technology for the generation of a strong and durable paracellular barrier," *Biosensors (Basel)*, vol. 8, no. 3, 2018.

[26] D. M. Lewis, N. Mavrogiannis, Z. Gagnon, and S. Gerecht, "Microfluidic platform for the real time measurement and observation of endothelial barrier function under shear stress," *Biomicrofluidics*, vol. 12, no. 4, p. 042202, 2018.

[27] B. Srinivasan, A. R. Kolli, M. B. Esch, H. E. Abaci, M. L. Shuler, and J. J. Hickman, "Teer measurement techniques for in vitro barrier model systems," *J Lab Autom*, vol. 20, no. 2, pp. 107–26, 2015.

[28] L. Kaplan, B. W. Chow, and C. Gu, "Neuronal regulation of the blood-brain barrier and neurovascular coupling," *Nat Rev Neurosci*, vol. 21, no. 8, pp. 416–432, 2020.

[29] R. Booth and H. Kim, "Characterization of a microfluidic in vitro model of the blood-brain barrier (mubbb)," *Lab Chip*, vol. 12, no. 10, pp. 1784–92, 2012.

[30] R. Booth and H. Kim, "Permeability analysis of neuroactive drugs through a dynamic microfluidic in vitro blood-brain barrier model," *Ann Biomed Eng*, vol. 42, no. 12, pp. 2379–91, 2014.

[31] L. M. Griep, F. Wolbers, B. de Wagenaar, P. M. ter Braak, B. B. Weksler, I. A. Romero, P. O. Couraud, I. Vermes, A. D. van der Meer, and A. van den Berg, "Bbb on chip: microfluidic platform to mechanically and biochemically modulate blood-brain barrier function," *Biomed Microdevices*, vol. 15, no. 1, pp. 145–50, 2013.

[32] M. Odijk, A. D. van der Meer, D. Levner, H. J. Kim, M. W. van der Helm, L. I. Segerink, J. P. Frimat, G. A. Hamilton, D. E. Ingber, and A. van den Berg, "Measuring direct current trans-epithelial electrical resistance in organ-on-a-chip microsystems," *Lab Chip*, vol. 15, no. 3, pp. 745–52, 2015.

[33] H. J. Kim, D. Huh, G. Hamilton, and D. E. Ingber, "Human gut-on-a-chip inhabited by microbial flora that experiences intestinal peristalsis-like motions and flow," *Lab Chip*, vol. 12, no. 12, pp. 2165–74, 2012.

[34] F. R. Walter, S. Valkai, A. Kincses, A. Petneházi, T. Czeller, S. Veszelka, P. Ormos, M. A. Deli, and A. Dér, "A versatile lab-on-a-chip tool for modeling biological barriers," *Sensors and Actuators B: Chemical*, vol. 222, pp. 1209–1219, 2016.

[35] Y. I. Wang, H. E. Abaci, and M. L. Shuler, "Microfluidic blood-brain barrier model provides in vivo-like barrier properties for drug permeability screening," *Biotechnol Bioeng*, vol. 114, no. 1, pp. 184–194, 2017.

[36] O. Y. F. Henry, R. Villenave, M. J. Cronce, W. D. Leineweber, M. A. Benz, and D. E. Ingber, "Organs-on-chips with integrated electrodes for trans-epithelial electrical resistance (teer) measurements of human epithelial barrier function," *Lab Chip*, vol. 17, no. 13, pp. 2264–2271, 2017.

[37] M. W. van der Helm, O. Y. F. Henry, A. Bein, T. Hamkins-Indik, M. J. Cronce, W. D. Leineweber, M. Odijk, A. D. van der Meer, J. C. T. Eijkel, D. E. Ingber, A. van den Berg, and L. I. Segerink, "Non-invasive sensing of transepithelial barrier function and tissue differentiation in organs-on-chips using impedance spectroscopy," *Lab Chip*, vol. 19, no. 3, pp. 452–463, 2019.

[38] A. Mossu, M. Rosito, T. Khire, H. Li Chung, H. Nishihara, I. Gruber, E. Luke, L. Dehouck, F. Sallusto, F. Gosselet, J. L. McGrath, and B. Engelhardt, "A silicon nanomembrane platform for the visualization of immune cell trafficking across the human blood-brain barrier under flow," *J Cereb Blood Flow Metab*, vol. 39, no. 3, pp. 395–410, 2019.

[39] A. T. Salminen, J. Zhang, G. R. Madejski, T. S. Khire, R. E. Waugh, J. L. McGrath, and T. R. Gaborski, "Ultrathin dual-scale nano- and microporous membranes for vascular transmigration models," *Small*, vol. 15, no. 6, p. e1804111, 2019.

[40] D. Hudecz, T. Khire, H. L. Chung, L. Adumeau, D. Glavin, E. Luke, M. S. Nielsen, K. A. Dawson, J. L. McGrath, and Y. Yan, "Ultrathin silicon membranes for in situ optical analysis of nanoparticle translocation across a human blood-brain barrier model," *ACS Nano*, vol. 14, no. 1, pp. 1111–1122, 2020.

[41] T. P. Buzhdygan, B. J. DeOre, A. Baldwin-Leclair, T. A. Bullock, H. M. McGary, J. A. Khan, R. Razmpour, J. F. Hale, P. A. Galie, R. Potula, A. M. Andrews, and S. H. Ramirez, "The sars-cov-2 spike protein alters barrier function in 2d static and 3d microfluidic in-vitro models of the human blood-brain barrier," *Neurobiol Dis*, vol. 146, p. 105131, 2020.

[42] J. Ryan, "Evolution of cell culture surfaces," 2008.

[43] Y. Son, "Determination of shear viscosity and shear rate from pressure drop and flow rate relationship in a rectangular channel," *Polymer*, vol. 48, no. 2, pp. 632–637, 2007.

[44] M. Sun, K. Han, R. Hu, D. Liu, W. Fu, and W. Liu, "Advances in micro/nanoporous membranes for biomedical engineering," *Adv Healthc Mater*, p. e2001545, 2021.

[45] M. P. Tibbe, *Improving Organ on-Chip Physiology: Exploring the barrier in blood-brain barrier on-chip systems*. PhD thesis, University of Twente, 2020.

[46] H. H. Chung, M. Mireles, B. J. Kwarta, and T. R. Gaborski, "Use of porous membranes in tissue barrier and co-culture models," *Lab Chip*, vol. 18, no. 12, pp. 1671–1689, 2018.

[47] it4p, "Basics of track-etching technology,"

[48] S. M. Casillo, A. P. Peredo, S. J. Perry, H. H. Chung, and T. R. Gaborski, "Membrane pore spacing can modulate endothelial cell-substrate and cell-cell interactions," *ACS Biomater Sci Eng*, vol. 3, no. 3, pp. 243–248, 2017.

[49] F. K. e. a. van Meer BJ, de Vries H, "Small molecule absorption by pdms in the context of drug response bioassays,"

[50] M. S., A. S.A., and F. P.J., "Silicon sensors actuators," 2020.

[51] R. N. Carter, S. M. Casillo, A. R. Mazzocchi, J. S. DesOrmeaux, J. A. Roussie, and T. R. Gaborski, "Ultrathin transparent membranes for cellular barrier and co-culture models," *Biofabrication*, vol. 9, no. 1, p. 015019, 2017.

[52] S. H. Ma, L. A. Lepak, R. J. Hussain, W. Shain, and M. L. Shuler, "An endothelial and astrocyte co-culture model of the blood-brain barrier utilizing an ultra-thin, nanofabricated silicon nitride membrane," *Lab Chip*, vol. 5, no. 1, pp. 74–85, 2005.

[53] W. Wang, R. Narain, and H. Zeng, *Hydrogels*, pp. 203–244. 2020.

[54] J. Nicolas, S. Magli, L. Rabbachin, S. Sampaolesi, F. Nicotra, and L. Russo, "3d extracellular matrix mimics: Fundamental concepts and role of materials chemistry to influence stem cell fate," *Biomacromolecules*, vol. 21, no. 6, pp. 1968–1994, 2020.

[55] "Hydrogels for 3d cell culture, https://www.sigmaaldrich.com/nl/en/technical-documents/technical-article/cell-culture-and-cell-culture-analysis/3d-cell-culture/3d-hydrogels,"

[56] S. Kim, M. Chung, J. Ahn, S. Lee, and N. L. Jeon, "Interstitial flow regulates the angiogenic response and phenotype of endothelial cells in a 3d culture model," *Lab Chip*, vol. 16, no. 21, pp. 4189–4199, 2016.

[57] MIMETAS, "Hydrogels for 3d cell culture, https://www.mimetas.com/en/blogs/345/3d-cell-culture-vs.-traditional-2d-cell-culture-explained.html,"

[58] P. Vulto, S. Podszun, P. Meyer, C. Hermann, A. Manz, and G. A. Urban, "Phaseguides: a paradigm shift in microfluidic priming and emptying," *Lab Chip*, vol. 11, no. 9, pp. 1596–602, 2011.

[59] A. Nicolas, F. Schavemaker, K. Kosim, D. Kurek, M. Haarmans, M. Bulst, K. Lee, S. Wegner, T. Hankemeier, J. Joore, K. Domansky, H. L. Lanz, P. Vulto, and S. J. Trietsch, "High throughput transepithelial electrical resistance (teer) measurements on perfused membrane-free epithelia," *Lab Chip*, vol. 21, no. 9, pp. 1676–1685, 2021.

[60] S. J. Trietsch, E. Naumovska, D. Kurek, M. C. Setyawati, M. K. Vormann, K. J. Wilschut, H. L. Lanz, A. Nicolas, C. P. Ng, J. Joore, S. Kustermann, A. Roth, T. Hankemeier, A. Moisan, and P. Vulto, "Membrane-free culture and real-time barrier integrity assessment of perfused intestinal epithelium tubes," *Nat Commun*, vol. 8, no. 1, p. 262, 2017.

[61] R. Hatsuki, F. Yujiro, and T. Yamamoto, "Direct measurement of electric double layer in a nanochannel by electrical impedance spectroscopy," *Microfluidics and Nanofluidics*, vol. 14, no. 6, pp. 983–988, 2012.

[62] P. S., "Electrochemistry crash course for engineers," 2021.

[63] S. Grimnes and G. Martinsen, "Sources of error in tetrapolar impedance measurements on biomaterials and other ionic conductors," *Journal of Physics D: Applied Physics*, vol. 40, no. 1, pp. 9–14, 2007.

[64] J. Yeste, X. Illa, C. Gutiérrez, M. Solé, A. Guimerà, and R. Villa, "Geometric correction factor for transepithelial electrical resistance measurements in transwell and microfluidic cell cultures," *Journal of Physics D: Applied Physics*, vol. 49, no. 37, 2016.

[65] S. R. Gillmer, D. Z. Fang, S. E. Wayson, J. D. Winans, N. Abdolrahim, J.-P. S. DesOrmeaux, J. Getpreecharsawas, J. D. Ellis, P. M. Fauchet, and J. L. McGrath, "Predicting the failure of ultrathin porous membranes in bulge tests," *Thin Solid Films*, vol. 631, pp. 152–160, 2017.

[66] Kovács, A. Kovács, and U. Mescheder, "Estimation of elasticity modulus and fracture strength of thin perforated sin membranes with finite element simulations," *Computational Materials Science*, vol. 43, no. 1, pp. 59–64, 2008.

[67] R. L. Edwards, G. Coles, and W. N. Sharpe, "Comparison of tensile and bulge tests for thin-film silicon nitride," *Experimental Mechanics*, vol. 44, no. 1, pp. 49–54, 2004.

[68] S. Gholizadeh, Z. Allahyari, R. Carter, L. F. Delgadillo, M. Blaquiere, F. Nouguier-Morin, N. Marchi, and T. R. Gaborski, "Robust and gradient thickness porous membranes for in vitro modeling of physiological barriers," *Adv Mater Technol*, vol. 5, no. 12, 2020.

[69] H. A., "Failure theories, http://ah-engr.com/som/9_failure/text_9-1.htm,"

[70] E. Kobeda, "Intrinsic sio2 film stress measurements on thermally oxidized si," *Journal of Vacuum Science Technology B: Microelectronics and Nanometer Structures*, vol. 5, no. 1, 1987.

[71] E. Serra, M. Bawaj, A. Borrielli, G. Di Giuseppe, S. Forte, N. Kralj, N. Malossi, L. Marconi, F. Marin, F. Marino, B. Morana, R. Natali, G. Pandraud, A. Pontin, G. A. Prodi, M. Rossi, P. M. Sarro, D. Vitali, and M. Bonaldi, "Microfabrication of large-area circular high-stress silicon nitride membranes for optomechanical applications," *AIP Advances*, vol. 6, no. 6, 2016.

[72] "Bosch process oxford instruments website, https://plasma.oxinst.com/technology/deep-reactive-ion-etching."

[73] T. S., "Rapier recipe parameters overview," *EKL Phoenix Database*.

[74] S. Matter, "Block copolymers, http://soft-matter.seas.harvard.edu/index.php/block_copolymers,"

[75] F. Montagne, N. Blondiaux, A. Bojko, and R. Pugin, "Molecular transport through nanoporous silicon nitride membranes produced from self-assembling block copolymers," *Nanoscale*, vol. 4, no. 19, pp. 5880–6, 2012.

[76] J. P. DesOrmeaux, J. D. Winans, S. E. Wayson, T. R. Gaborski, T. S. Khire, C. C. Striemer, and J. L. McGrath, "Nanoporous silicon nitride membranes fabricated from porous nanocrystalline silicon templates," *Nanoscale*, vol. 6, no. 18, pp. 10798–805, 2014.

[77] B. Wolfrum, Y. Mourzina, F. Sommerhage, and A. Offenhauser, "Suspended nanoporous membranes as interfaces for neuronal biohybrid systems," *Nano Letters*, 2006.

[78] J. R. Oh, J. H. Moon, H. K. Park, J. H. Park, H. Chung, J. Jeong, W. Kim, and Y. R. Do, "Wafer-scale colloidal lithography based on self-assembly of polystyrene nanospheres and atomic layer deposition," *Journal of Materials Chemistry*, vol. 20, no. 24, 2010.

[79] K. Chen, S. V. Stoianov, J. Bangerter, and H. D. Robinson, "Restricted meniscus convective self-assembly," *J Colloid Interface Sci*, vol. 344, no. 2, pp. 315–20, 2010.

[80] A. Dimitrov and N. K., "Continuous convective assembling of fine particles into two-dimensional arrays on solid surfaces," *Langmuir*, 1995.

[81] Y. Chen, D. Shi, Y. Chen, X. Chen, J. Gao, N. Zhao, and C. P. Wong, "A facile, low-cost plasma etching method for achieving size controlled non-close-packed monolayer arrays of polystyrene nano-spheres," *Nanomaterials (Basel)*, vol. 9, no. 4, 2019.

[82] B.-K. Lee, K. S. Kim, J.-H. Lee, N.-H. Kim, and Y. Roh, "Nanometer-scaled triangular platinum islands fabricated using the bridge phenomenon of polystyrene beads," *Journal of Vacuum Science Technology A: Vacuum, Surfaces, and Films*, vol. 26, no. 4, pp. 819–823, 2008.

[83] C. T. Pan, P. J. Cheng, M. F. Chen, and C. K. Yen, "Intermediate wafer level bonding and interface behavior," *Microelectronics Reliability*, vol. 45, no. 3-4, pp. 657–663, 2005.

[84] M. J. K. Klein, F. Montagne, N. Blondiaux, O. Vazquez-Mena, H. Heinzelmann, R. Pugin, J. Brugger, and V. Savu, "Sin membranes with submicrometer hole arrays patterned by wafer-scale nanosphere lithography," *Journal of Vacuum Science Technology B, Nanotechnology and Microelectronics: Materials, Processing, Measurement, and Phenomena*, vol. 29, no. 2, 2011.

[85] L. Cucullo, N. Marchi, M. Hossain, and D. Janigro, "A dynamic in vitro bbb model for the study of immune cell trafficking into the central nervous system," *J Cereb Blood Flow Metab*, vol. 31, no. 2, pp. 767–77, 2011.

[86] A. K. Achyuta, A. J. Conway, R. B. Crouse, E. C. Bannister, R. N. Lee, C. P. Katnik, A. A. Behensky, J. Cuevas, and S. S. Sundaram, "A modular approach to create a neurovascular unit-on-a-chip," *Lab Chip*, vol. 13, no. 4, pp. 542–53, 2013.

[87] B. Prabhakarpandian, M. C. Shen, J. B. Nichols, I. R. Mills, M. Sidoryk-Wegrzynowicz, M. Aschner, and K. Pant, "Sym-bbb: a microfluidic blood brain barrier model," *Lab Chip*, vol. 13, no. 6, pp. 1093–101, 2013.

[88] J. A. Brown, V. Pensabene, D. A. Markov, V. Allwardt, M. D. Neely, M. Shi, C. M. Britt, O. S. Hoilett, Q. Yang, B. M. Brewer, P. C. Samson, L. J. McCawley, J. M. May, D. J. Webb, D. Li, A. B. Bowman, R. S. Reiserer, and J. P. Wikswo, "Recreating blood-brain barrier physiology and structure on chip: A novel neurovascular microfluidic bioreactor," *Biomicrofluidics*, vol. 9, no. 5, p. 054124, 2015.

[89] O. Kilic, D. Pamies, E. Lavell, P. Schiapparelli, Y. Feng, T. Hartung, A. Bal-Price, H. T. Hogberg, A. Quinones-Hinojosa, H. Guerrero-Cazares, and A. Levchenko, "Brain-on-a-chip model enables analysis of human neuronal differentiation and chemotaxis," *Lab Chip*, vol. 16, no. 21, pp. 4152–4162, 2016.

[90] G. Adriani, D. Ma, A. Pavesi, R. D. Kamm, and E. L. Goh, "A 3d neurovascular microfluidic model consisting of neurons, astrocytes and cerebral endothelial cells as a blood-brain barrier," *Lab Chip*, vol. 17, no. 3, pp. 448–459, 2017.

[91] A. T. Salminen, Z. Allahyari, S. Gholizadeh, M. C. McCloskey, R. Ajalik, R. N. Cottle, T. R. Gaborski, and J. L. McGrath, "In vitro studies of transendothelial migration for biological and drug discovery," *Frontiers in Medical Technology*, vol. 2, 2020.

[92] S. I. Ahn, Y. J. Sei, H. J. Park, J. Kim, Y. Ryu, J. J. Choi, H. J. Sung, T. J. MacDonald, A. I. Levey, and Y. Kim, "Microengineered human blood-brain barrier platform for understanding nanoparticle transport mechanisms," *Nat Commun*, vol. 11, no. 1, p. 175, 2020.